BATCH PROCESSING OF BRAIN TISSUE SECTIONS FOR MILLIMETER-SCALE SERIAL SECTION TRANSMISSION ELECTRON MICROSCOPY CONNECTOMICS

A Dissertation
Presented to
The Academic Faculty

by

Timothy J. Lee

In Partial Fulfillment
of the Requirements for the Degree
BioEngineering

Georgia Institute of Technology
August 2019

BATCH PROCESSING OF BRAIN TISSUE SECTIONS FOR MILLIMETER-SCALE SERIAL SECTION TRANSMISSION ELECTRON MICROSCOPY CONNECTOMICS

Approved by:

Dr. Craig R. Forest, Advisor
School of Mechanical Engineering
Georgia Institute of Technology

Dr. Peter J. Yunker
School of Physics
Georgia Institute of Technology

Dr. R. Clay Reid
Allen Institute for Brain Science

Dr. Todd A. Sulchek
School of Mechanical Engineering
Georgia Institute of Technology

Dr. Machelle T. Pardue
School of Biomedical Engineering
Georgia Institute of Technology

Date Approved: June 13, 2019

To my grandma and grandpa, who instilled in me a desire to learn and to teach others, to my parents, who have always supported me in my education, and to my wife, who has helped me through countless sleepless nights along this journey

ACKNOWLEDGEMENTS

There are many people who I would like to thank for all of their encouragement and support throughput my doctoral studies. First, I would like to thank my family for their indefatigable support throughout my PhD: To my wife, Jacqueline, who has and continues to support my academic pursuits, I thank you, for I could and would not do this without you. To my mother and father, thank you for your unending encouragement and reassurance of my choices. It was during some of my lowest points filled with self-doubt that you provided words of love and compassion. To my sister and brother-in-law, thank you for your help and kindness; some of my fondest memories these past years have been the times we laughed and celebrated my successes together.

Thank you to my doctoral thesis committee; I have been lucky to have such a supportive and collegial thesis committee—dear professors who I look forward to calling colleagues in the future. Thank you to my advisor, Dr. Craig, Forest for your support and encouragement. From the beginning of my project, hatched at the Allen Institute in the autumn of 2014, to soon the end of my work at Georgia Tech, you have been a phenomenal mentor, coach, advocate, critic, partner, and colleague. Thank you Dr. Clay Reid for your mentorship and guidance, particularly in the field of neuroanatomy and connectomics. Coming in as a first-year student having a degree in mechanical engineering, you welcomed me into your office at the Allen Institute to chat over five years ago. To think at the time that we would be sharing drinks and conversing over the latest advances in connectomics in Berlin five years later would have been unfathomable. Yet, here we are. Thank you Clay, for without you, I would not be going into neuroscience. You have

provided more than just guidance and mentorship—for me you have provided inspiration and instilled in me self-confidence, that I can go into neuroscience and that I can and will make an impact in this new field. Thank you Dr. Machelle Pardue for your advice over these years. You have always lent me an ear no matter when I happened to visit your office and find you there. I am deeply grateful for your kindness in training me to use the ultramicrotome as well as in entertaining all of the wacky and crazy ideas with regards to serial sectioning. Thank you, also, for making me think critically about how I can use the tools I have developed to further neuroscience, beyond just the neuroanatomy of cortical tissue, but also thinking about the applications to other tissues in the nervous system. Thank you Dr. Peter Yunker for teaching me about the fascinating field of soft matter physics. It was serendipitous that we would be able to collaborate and that your interests would help my research. I am glad that part of my doctoral studies included some physics, for often times, it is easy to get mired in the details engineering and forget the broader implications, which by peering through the lens of a physicist, can often elucidate. In the end, I am excited that I have been able to use our work in capillary interactions, and I hope others adopt this work! Thank you Dr. Todd Sulchek for all of your help when I was in need of advice about microfabrication. You were always willing to chat about my research when I happened to stop by your office—for this I am grateful. Also, due to the proximity of the Forest and Sulchek Labs in Wing 2A of the Petit Institute for Bioengineering and Bioscience, I have benefited greatly from all of the wonderful friendships with your lab members.

Thank you to all of the Allen Institute for Brain Science staff that I have had the pleasure of working with over these five years; coming into Georgia Tech, I knew close to

nothing of neuroscience, but with the guidance, friendship, and mentorship of so many people—largely in part from the Allen Institute—I look forward to bravely charging headfirst into field of connectomics and neuroanatomy. Thank you to Dr. Dan Bumbarger—a dear colleague and friend—for everything: from working long hours in the sectioning room, to staying late to image some tissue in the TEM, to recommending me to your colleagues for a post-doc, to grabbing a beer just for the sake of having a beer together, I could not have completed my doctoral thesis without you nor would I have the opportunity to move to Germany for a post-doctoral position. I look forward to hanging out and collaborating again soon! Thank you Dr. Stephen Smith for your wonderful wit, enthusiasm, and encouragement; it was your interest in my work—manipulating serial sections with fluid flow—many years ago that made me believe that I could make an impact in the field of neuroscience. Everyone needs someone to believe in them—not just people who are inherently on their side, like their friends and family, but rather people who are in field. Thank you Dr. Smith for your belief in me. I look forward to contributing to the field of neuroscience, connectomics, and neuroanatomy. Thank you to Dr. Nuno da Costa, Dr. Adam Bleckert, Dr. Agnes Bodor, Dr. Forrest Collman, Marc Takeno, Derrick Brittain, and Joann Buchanan for all of your advice and support. Thank you, especially, for making me feel welcome whenever I visited Seattle.

Thank you to all of my collaborators at Georgia Tech: to Drs. Tom Read and Ross Ethier for their time and use of ultramicrotomy equipment. In particular, thank you Tom for your willingness to talk about the most random of topics, like the pesky raccoons of Toronto, despite your busy schedule. You have been a wonderful resource in helping me develop my automated serial sectioning system; thank you for all of the resources, training,

and advice you have given me throughput the duration of my doctoral studies. Thank you to the Parker H. Petit Institute for Bioengineering and Bioscience staff for their kindness and support. In particular, thank you to Melissa Raine for your kindness and diligence. Your work ethic, compassion, and honesty have served as an example for me. Thank you to Lois Wiggins for your kindness and support; I always appreciate the conversations we can have to take a break from the busy-ness of work. Thank you to Dr. Bob Nerem for your generous support in founding and providing the Nerem International Travel Award, through which I was able to travel to Bonn, Germany and complete part of my doctoral studies. In traveling to Bonn, thank you to Drs. Kevin Briggman and Stephan Irsen for your time, advice, and use of electron microscopy equipment at the Center of Advanced European Studies and Research (caesar). Thank you to the Institute for Electronics and Nanotechnology staff for providing both seed grant funding as well as exemplary advice and assistance in all of my microfabrication needs.

Thank you to all the current and past Precision Biosystems Lab members who have been critical to my finishing my PhD work. Thank you to Dr. Christopher Phanuef for showing me the ropes when I first arrived at Georgia Tech. Thank you to Dr. Caitlin Austin for being a wonderful friend and confidant during all of my research struggles; you are the best Dr. Teemo. Thank you to Dr. Gregory Holst for advice and assistance—your commitment to detail and thoroughness serve as an example for me. Thank you to Dr. Ilya Kolb for your friendship and advice; your scientific rigor and work ethic are admirable, and I look forward to crossing paths in the future. Thank you to Dr. William Stoy for your willingness to talk about anything. I am deeply grateful for the creative and open atmosphere you brought to the lab, and I will miss it dearly. I look forward to future

collaboration. Thank you to Corey Landry, Colby Lewallen, Mighten Yip, Dr. Bo Yang, and Phoebe Welch for being wonderful lab mates, helping me with experiments, editing my papers, and much more. You have made these past years extremely fun, between the group workouts, lab outings, weird lab traditions, and spontaneous lunches/coffee breaks. Thank you to Aditi Kumar, the best undergraduate student one could hope for. Your hard work and dedication have been a blessing to me. Working with you has solidified my desire to become a professor in the future. I look forward to seeing where life takes you.

Thank you to all of my friends who have played critical roles in supporting my well being outside of the lab to make this PhD possible. Thank you to Dr. Brandon Dixon for your hospitality and support since the first year of my PhD. Thank you to my wonderful house church: Cam, Rachel, Michael, Mike, and Mason for being there for me, counseling me through tough times, and celebrating with me through the good. Thank you to Bill and Carol Robinson for being wonderful friends to me since moving to Georgia five year ago. Thank you to Dr. Ernest Lai and Dr. Dennis Shem for your constant companionship: it seems like in the blink of an eye we have come so far from freshman year at Cal. Thank you to Chris Chu for being my best friend through it all; thanks for helping me find time to relax and play some video games between the long hours in lab.

And to all else who have played some role—big or small—in helping me get to this point in my PhD, thank you. For without you, I would not be here.

TABLE OF CONTENTS

LIST OF FIGURES

LIST OF SYMBOLS AND ABBREVIATIONS

3D-EM	three-dimensional electron microscopy
ATLUM	automatic tape-collecting lathe ultramicrotome
ATUM	automated tape ultramicrotome
ATUM-SEM	automated tape-collecting ultramicrotome scanning electron microscopy
CAD	computer-aided design
CAM	computer-aided manufacturing
DOF	degrees of freedom
EM	electron microscopy
ESF	edge spread function
FEA	finite element analysis
FIB-SEM	focused ion beam scanning electron microscopy
LASSO	loop-based, automated serial sectioning operation
MRI	magnetic resonance imaging
PDMS	polydimethylsiloxane
RMS	root mean square
RMSE	root mean square error
ROI	region of interest
SBEM	serial block-face electron microscopy
SEM	scanning electron microscopy
SiN	silicon nitride
SLA	stereolithography
ssEM	serial section electron microscopy

ssTEM	serial section transmission electron microscopy
STEM	scanning transmission electron microscopy

SUMMARY

In the field of connectomics, serial section transmission electron microscopy (ssTEM) has emerged as a promising approach for exploring the nature of neural circuits. These neuronal networks likely contain significant insight into information processing, learning, and memory. However, our ability to study neural circuits using ssTEM is held back by the difficulty in consistently and rapidly collecting neuroanatomical datasets. Currently, these datasets are obtained by cutting ~10^2 – 10^3 consecutive, i.e., "'serial," brain slices, i.e., "sections," with a diamond knife. As a result, the collection of ~10^2 – 10^3 serial sections in a repeatable and robust fashion remains an unsolved problem that is paramount for the advancement of ssTEM connectomics. In this work, I discuss and demonstrate a serial sectioning technology platform that enables the automated collection of ~10^2 – 10^3 serial sections. I show with modeling and experiment, that serial sections can be accurately and repeatably transported and trapped using hydrodynamic forces and curvature-induced quadrupolar-monopolar capillary interactions (RMS accuracy and repeatability = 360 ± 200 μm). Subsequently, I describe and implement a scalable, batch-process serial sectioning methodology that utilizes microfabricated and robotic tools, collecting 729 serial sections of human brain tissue without significant tissue damage and with 99.7% yield. Lastly, I demonstrate an open-loop, automated approach for trapping and collecting serial sections in an in-line fashion with capillary- and Stokes-based forces, acquiring batches of ~10^2 serial sectioning with < 1% loss onto a variety of light and electron microscopy substrates. In total, this work outlines a scalable, flexible, and accessible technology platform for automated serial sectioning, enabling and accelerating the pace of millimeter-scale ssTEM connectomics studies.

CHAPTER 1. INTRODUCTION

Understanding the brain remains one of the greatest scientific challenges of our time. Over the past decade, the field of connectomics has emerged as one of the most promising approaches to exploring the nature of neural circuits. A millimeter-scale connectome—a neuron-to-neuron wiring diagram of a neural circuit—potentially contains a vast trove of information regarding sensory processing, learning, and memory. The field of connectomics is held back, however, by the great difficulty in reliably collecting these neuroanatomical datasets, i.e., connectomes, using serial section electron microscopy (ssEM). Currently, these datasets are obtained by cutting plastic-embedded neural tissue blocks into ~10^2 – 10^3 consecutive, i.e., "'serial," ultrathin (~50 nm) brain slices, i.e., "sections," with a diamond knife into an adjoining waterboat. As a result, the collection of serial sections, i.e., "serial sectioning" in a repeatable and robust fashion remains an unsolved problem that is paramount for the advancement of ssEM. In this work, I describe technologies I have developed to create a platform for high-throughput, high-reliability serial sectioning for millimeter-scale connectomics.

In the past decade, a multitude of electron microscopy-based, connectomics studies have emerged, elucidating the efficacy of electron microscopy (EM) for neural circuit mapping (Bock, Reid, et al., 2011, Helmstaeder, et al., 2013, Kasthuri, et al., 2015, Zheng, et. al., 2017). Yet, among these methods, serial section transmission electron microscopy (ssTEM) remains the fastest technique (Briggman and Bock, 2012, Kornfeld and Denk, 2018). In ssTEM connectomics studies of neural circuits, significant time and effort is spent (1) collecting tissue sections, (2) imaging sections, and (3) tracing neuronal processes

(Oberti, et al., 2011). Developments in automating the imaging of sections have greatly improved the imaging throughput of ssTEM (Bock, et al., 2011). Subsequently, the tracing process, i.e., segmentation, has seen significant progress due to the application of novel image processing algorithms and artificial intelligence (Arganda-Carreras, et al., 2015, Beier, et al., 2017, Lee, et. al., 2017). Accordingly, the remaining bottleneck in producing connectomics data lies in the reliable collection of serial sections for serial section transmission electron microscopy.

To advance our understanding of the mammalian brain structure and function, I have developed tools and methods for ultrathin serial sectioning to enable millimeter-scale connectomics studies. While the following dissertation has been divided into three main parts—or "aims"—these components come together to form a unified technology platform, both pragmatically and theoretically, to enable millimeter-scale serial section electron microscopy-based connectomics. In Chapter 2, I design, test, and characterize a novel hydrodynamic and surface tension-based device to enable passive transport and trapping of ultrathin sections. I discuss and demonstrate curvature-induced quadrupolar capillary interactions and their effect upon ultrathin sections, which had not been previously shown. In Chapter 3, I investigate and implement batch processing of serial sections to enable reliable section processing. This work, being multi-disciplinary in nature, combines aspects of neuroscience (EM-based connectomics), mechanical engineering (microfabrication and robotics), and industrial engineering (batch processing and statistical modeling). And in Chapter 4, I develop and characterize an automated section-processing platform to enable high-throughput millimeter-scale connectomics dataset collection. I use the insights found in Chapter 2—the effect of curvature-induced quadrupolar capillary interactions upon

serial sections—to trap individual sections and subsequently—using the insights drawn from Chapter 3—to pick up these sections in an open-loop, batch-process fashion. Finally, in Chapter 5, I discuss perspectives and future direction for the field of EM connectomics as a whole. Altogether, this work contributes to the expanding field of connectomics to usher in the rapid investigation of neural circuits, shedding light unto human cognition, memory, and learning as well as the neuroanatomical underpinnings of neurological diseases in the human brain.

1.1 Background

1.1.1 Overview of volume electron microscopy

Up to four different electron microscopy techniques exist for high-throughput, large-scale volume electron microscopy. Each of these methods is useful for the study of neuroanatomy and connectomics but have inherent drawbacks.

Serial Blockface Electron Microscopy (SBEM) involves placing a volume of tissue inside an electron microscope, imaging, and then physically sectioning the imaged surface to uncover the next layer of tissue to be imaged. In this way, one is able to image a volume of tissue. SBEM typically cedes 16 nm x 16 nm (in-plane resolution) x 24 nm (determined by section thickness) with imaging rates ~1 Mpix/s. With this methodology, each section can only be imaged once, for immediately after imaging, each section is removed from the block-face via physical sectioning, i.e., it is not collected. This precludes the ability to reimage sections at higher magnification, if desired. On the other hand, this methodology cedes inherently aligned image stacks; because the sample block does not move laterally

between consecutive sections, the acquired images come pre-aligned, which is beneficial for downstream image processing.

Focused Ion Beam Scanning Electron Microscopy (FIB-SEM) uses a focused beam of gallium ions to destroy each layer of tissue after it has been imaged. FIB-SEM is capable of delivering perfectly isotropic voxels, 5 nm in each dimension, with imaging rates ~1 Mpix/s. The obtaining of isotropic voxels is beneficial for downstream segmentation as consecutive sections in the nominal "z-direction" display less change; therefore, it becomes easier to align and segment consecutive sections. For both methods, SBEM and FIB-SEM, their imaging rates are too slow for millimeter-scale neuroanatomy studies and as a result, are best for investigating smaller volumes (~1,000 μm^3) (Briggman and Bock, 2012). Similar to SBEM, FIB-SEM destroys the tissue after it has been imaged in the electron microscope, precluding the ability for samples to be re-imaged.

Automated Tape-collecting Ultramicrotome Scanning Electron Microscopy (ATUM-SEM) uses an automated device to simultaneously cut and collect ultrathin sections onto a reel of tape (e.g., Kapton tape), which are subsequently imaged in an SEM (Hayworth, et. al., 2006). While this device eliminates the difficulty in section handling, the slow imaging rates of scanning electron microscopy prohibit millimeter-scale neuroanatomical studies. It is important to note, in recent years, this technique has been adapted to TEM systems (personal communication, W.C.A., Lee, D.J. Bumbarger, & R.C. Reid).

In a similar vein, serial section transmission electron microscopy (ssTEM) consists of ultrathin serial sectioning followed by placement of consecutive sections onto an electron microscopy substrate, known as a "TEM grid" (See Figure 1).

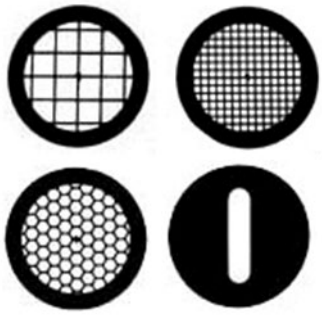

Figure 1: Examples of TEM grids. Grids can be purchased with various mesh sizes or aperture patterns. The "slot grid" (*bottom right*) is commonly used for ssTEM studies due to its relatively large aperture size.

Since the work of Porter, Claude, and Fullam in 1945, transmission electron microscopy has become the gold standard for the investigation of cellular ultrastructure (Porter, et. al., 1945). Moreover, the study of *serial* sections with transmission electron microscopy has enabled three-dimensional cellular ultrastructural studies (Sjostrand, 1958, Ware & LoPresti, 1975). Currently, the field is held back by section processing: While state-of-the-art techniques allow for the processing of thousands of sections, these methods are not scalable to tens of thousands of sections. Therefore, significant innovation in section processing is necessary to enable millimeter-scale connectomics studies.

1.1.2 Section processing state-of-the-art

Blocks of tissue, prepared for electron microscopy, are cut into ultrathin (< 50 nm) section using an ultramicrotome. Details regarding *en bloc* staining and plastic embedment are contained in Appendix A. A specialized diamond knife is used (with tip-radius of nominally 2 nanometers) to cut tissue sections. For serial sectioning, it is convenient to cut

ribbons of sections, wherein consecutive sections are connected to one another in a head-to-tail fashion. Due to their thickness, sections must be cut into a water boat, a small reservoir for water that is attached to a diamond or glass knife. Modern diamond knives typically have the diamond knife embedded within the waterboat. As sections are cut, the water contained within the waterboat supports the sections; accordingly, the sections lie on the water-air interface. Once sections have been cut and lie on the water-air interface, a series of steps must occur to move sections onto a transmission electron microscopy substrate. I will define these series of steps to be "section processing."

Since the 1950's, a variety of techniques have been used for section processing. Below, a history of section processing is given.

1954 Gay and Anderson: A platinum wire loop is coated with an electron transparent film, e.g., Formvar (see Revell and Agar, 1955 for description of fabrication of Formvar). The coated loop is manually lowered over a ribbon of sections, picking them up. An uncoated TEM grid is placed on a cylindrical pillar, with outer diameter smaller than the inner diameter of the platinum loop. The loop is concentrically lowered over the pillar, paying careful attention to align the ribbon of sections with the grid aperture. As the loop is lowered over the grid, the thin film detaches from the loop and attaches to the grid, suspending the ribbon of sections over the grid aperture.

1959 Dowell: A Formvar-coated grid is lowered at a near-vertical angle into the water boat until the grid aperture is fully submerged. The grid is manipulated until it is beneath a ribbon of sections, paying close attention

to align the slot aperture in the grid with the ribbon of sections. The grid is gently lifted out of the water, picking up the ribbon of sections.

1961 Barnes and Chambers: A Formvar-coated platinum wire loop is secured to a manual micromanipulator comprised of microscope slides and bent tubing. The wire loop is positioned over a ribbon of sections in the waterboat, picked up, and transferred to a slot grid, paying careful attention to align the section ribbon with the orientation of the slot in the grid.

1962 Westfall and Healy: An external device is used to clamp a Formvar coated grid within the waterboat and submerged beneath the water-air interface. An eyelash is used to transport a ribbon of sections until the ribbon is positioned over the slot in the grid. The water level is lowered and the ribbon of sections is lowered onto the grid.

The method introduced by Dowell (1959), later reproduced by Harris, et. al., (2006), has remained the conventional method by which sections are processed for ssTEM studies. In all of these methods, section processing can be sub-divided into three steps:

Section transport: Sections are manipulated on the water-air interface, i.e., an eyelash is used to move the section.

Section pick-up: Sections are pick-up, i.e. a loop end-effector or grid is used to remove the section from the water-air interface.

Section placement: Sections are placed onto a transmission electron microscopy substrate.

For the remainder of this thesis, I will discuss serial sectioning with respect to these three steps.

CHAPTER 2. MODELING, DESIGN, AND CHARACTERIZATION OF A DEVICE FOR PASSIVE TRANSPORT AND TRAPPING OF ULTRATHIN SECTIONS USING HYDRODYNAMICS AND SURFACE TENSION FORCES

2.1 Introduction

A significant risk for section loss occurs during section transport and section pick-up (Westfall and Healy, 1962, Bock, et. al., 2011, Bumbarger, et. al., 2013). Sections must not be damaged during transport and must be placed accurately and repeatably onto an electron transparent substrate. Hydrodynamic forces (Shenoy, et. al., 2016, Tanyeri, et. al., 2013) and surface tension forces (Würger, 2006, Sharifi-Mood, et. al., 2015, Yao, et. al., 2015, Sharifi-Mood, 2016) show potential for non-contact, passive transport and trapping of ultrathin sections. Therefore, in the following, I discuss a novel device, with associated mathematical modeling, that enables intact, passive transport of sections as well as accurate and repeatable trapping of sections for section pick-up.

2.1.1 Ultrathin sections and nanosheets

Two-dimensional nanomaterials, also called "nanosheets", feature thicknesses on the order of nanometers, with lengths and widths on the order of micrometers to millimeters. Nanosheets hold promise to bring significant advances in thin-film transistor, actuator, energy harvesting/power generating, and opto-electronic technologies (Rogers, et. al., 2011, Eda, et. al., 2008, Rao, et. al., 2009, Monch, et. al., 2011, Fend, et. al., 2016). Accordingly, nanosheets, which are typically discussed in the disciplines of chemical

engineering and material science and engineering, bear remarkable similarity to ultrathin sections. Therefore, it is without surprise that many of the challenges faced by the nanosheet community overlap with that of those of the serial sectioning community. Namely, the fabrication and manipulation of nanosheets (i.e., ultrathin sections), as well as their integration with substrates and devices (i.e., section transport, pickup and placement), remains a significant challenge. In recent years, methods of nanosheet fabrication involving self-assembly of nanomaterials at liquid-air interfaces have been shown to be reliable for nanosheet manufacturing (Wang, et. al., 2011, Wang, et. al., 2015, Wang, et. al., 2016, Im, et. al., 2014). However, objects on liquid-air interfaces are subject to a complex combination of capillary and hydrodynamic forces (Stamou, et. al., 2000, Bowden, et. al., 2001, Kralchevsky, et. al., 2001, Fournier & Galatola, 2002, Loudet, et. al., 2005, Vella & Mahadevan, 2005, Würger, 2006, Dominguez, et. al., 2008, Cavallaro, et. al., 2011, Sharifi-Mood, et. al., 2015, Sharifi-Mood, et. al., 2015, Yao, et. al., 2015). Thus, while the ability to fabricate nanosheets has been well established, the manipulation of nanosheets remains an unsolved problem. In the following, we discuss various techniques that have been used to trap particles (of a wide range of sizes) and their relevancy to trapping nanosheets.

2.1.2 Overview of particle trapping methodologies

While nanosheet and ultrathin sections typically lie on a water-air interface, it is important to consider, as a starting point, methods of trapping for particles suspended within a single fluid. Within a single fluid, there are many options for particle manipulation, ranging from optical, magnetic, electrokinetic, closed-loop microfluidic hydrodynamic, and acoustic systems (Gosse & Croquette, 2002, Neuman & Block, 2006, Cohen &

Mourner, 2008, Ding, et. al., 2012, Probst & Cummins, 2012, Tanyeri & Schroeder, 2013, Shenoy, et. al., 2016).

Each method offers advantages and disadvantages closely tied to the particle of interest, but none are immediately compatible with a liquid-air interface used for nanosheet manufacturing: Specifically, magnetic or electrokinetic systems require nanosheets with intrinsic magnetism and polarizability, respectively. Optical or acoustic systems would be technically and practically difficult to implement due to their need for closed, microfluidic systems that are often pressurized. If considering only the aforementioned techniques, hydrodynamic systems would be the most promising direction for transporting and trapping of nanosheets.

2.1.3 Overview of curvature-induced capillary interactions

Curvature-induced capillary interactions exist at the interface between two fluids. These forces exist at the fluid-fluid interface due to the existence of a particle or particles that lie at this fluid-fluid interface and the necessity of this fluid-fluid interface to minimize its surface energy, i.e., particles on a fluid-fluid interface perturb the surface away from a minimal energy state so curvature-induced capillary interactions exist to return the interface back to a minimal energy state. Specifically, these interactions exist with different "polarities," each coming from its own mathematical description: Curvature-induced monopolar capillary interactions have an inverse relationship between force and distance, i.e., $F \sim r^{-1}$; curvature-induced dipole capillary interactions have an inverse relationship between force and distance squared, i.e., $F \sim r^{-2}$; quadrupolar capillary interactions have an inverse relationship between force and distance to the power four, i.e., $F \sim r^{-4}$. While higher order multipole interactions theoretically exist, they are often difficult to observe

experimentally. Yet, this has not dissuaded the empirical investigation of higher-order, multipole capillary interactions, with recently a hexapole capillary interaction being shown (Ferrar et al., 2018). It is important to note, all of these multipole interactions can exist simultaneously (and often do), but a single multipole interaction will typically dominate the other multipole interactions. Additionally, any deviation from any given specific multipole behavior can be often attributed to smaller higher order moments.

Curvature-induced capillary multipole interactions at the fluid-fluid interface are able to manipulate a variety of particles but typically across distances less than one capillary length. From prior literature, the dominant multipole interaction that facilitates particle movement varies depending on the geometry of the object: quadrupolar capillary interactions are known to facilitate the attraction of small ($r \sim 1$ μm) particles, while monopolar capillary interactions are known to facilitate the attraction of large ($r \sim 1$ mm) isometric objects (Gosse & Croquette, 2002, Neuman & Block, 2006, Cohen & Mourner, 2008, Ding, et al., 2012, Probst & Cummins, 2012, Tanyeri & Schroeder, 2013, Shenoy, et. al., 2016). For extremely anisotropic materials with aspect ratios much greater than one—e.g., nanosheets—it remains unclear which multipole capillary interaction is the dominant term. Nonetheless, for distances greater than one capillary length, multipole capillary interactions are generally impractical for rapid manipulation of nanosheets. Conversely, hydrodynamic forces are effective for long-range transportation at the air-water interface but are difficult to utilize for trapping. In the following, we discuss a hybrid technique which utilizes hydrodynamic forces for long-range transport of nanosheets and curvature-induced multipole capillary interactions for short-range trapping of nanosheets.

2.2 Methodology

An experimental test bed was developed to test hydrodynamic transport and curvature-induced capillary interaction-based trapping of nanosheets on a water-air interface. A schematic of the device is shown in Figure 2. Initially, a nanosheet is placed onto a flat water-air interface, thus deforming the water surface around itself, i.e., inducing curvature in the water-air interface. Due to surface tension forces, the nanosheet remains trapped at the water-air interface and does not sink. Bulk flow is produced within the channel, and the nanosheet is transported "downstream" via hydrodynamic forces, as indicated in Figure 2a, right. Further downstream, a trap is created from a micro-machined notch in the channel wall, which induces curvature on the water-air interface, shown in Figure 2b. As the nanosheet approaches the trap, the curvature induced by the nanosheet interacts with the curvature induced by the trap, attracting the nanosheet towards the trap. Ultimately, the nanosheet comes to rest at the trap, as shown in Figure 2c.

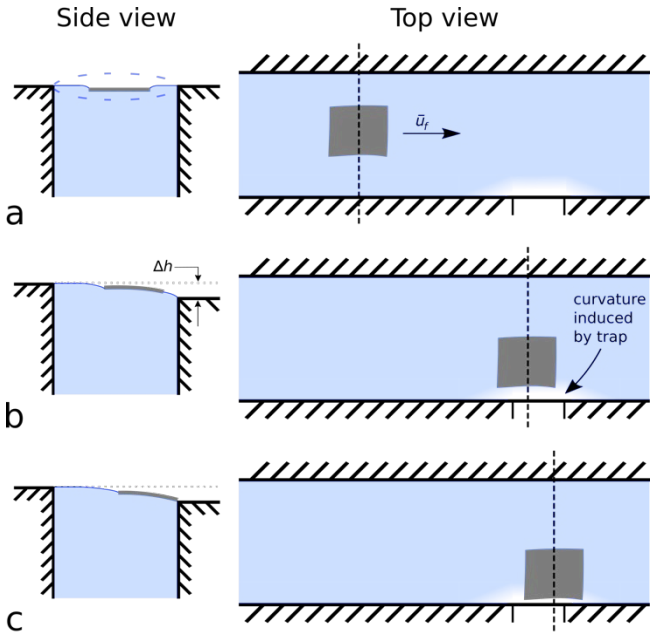

Figure 2: The nanosheet trapping device comprises a water-filled, open millifluidic channel with a notch (i.e., trap) along one edge. As a nanosheet flows through the channel, it comes to rest in contact with the trap. The device works by using a combination of hydrodynamic forces far from the trap (view a) and curvature-

induced capillary interactions close to the trap (views b, c) to transport and trap nanosheets, respectively. Top views illustrate the position of the nanosheet in the channel relative to the trap. Side views, at locations indicated by vertical dashed lines, illustrate curvature of water-air interface. (a, side view) The trap water height is set properly when the fluid level has minimal curvature. (a, top view) The water and nanosheet both flow with average velocity, ūf far from the trap (approximately 1-10x capillary length of the water-air interface, or equivalently 2.7 mm-27 mm). (b, side view) Near the trap (<1x capillary length (<2.7 mm) of the water-air interface), the nanosheet's trajectory is influenced by water-air curvature arising from the trap's height difference, Δh. (c, side view) The nanosheet comes to rest at the trap where the water-air interface surface energy is minimized.

2.2.1 Device design and fabrication

I designed and fabricated a device for nanosheet transport and trapping, shown in Figure 3. The device was designed in computer aided design software (SolidWORKS); G-code was generated using computer-aided manufacturing software (HSMWorks). The device was fabricated using a CNC mill (Haas Office Mill, Model OM-1A) from black Delrin®. Delrin was chosen due to its ease of machining; the black color enables optical contrast via thin film interference for observation. The channel length was 100 mm with a width and depth of 2 mm and 10 mm, respectively. The trap consists of a 1 mm wide, 100 μm-deep milled feature in the channel wall on one side (Figure 3, inset). The depth of the trapping feature was verified using surface profilometry (Veeco Dektak 150). Two 1 mm holes were added near each trap as fiducial marks for video registration during data processing. The device is open to atmospheric pressure and is not enclosed within any pressurized chamber.

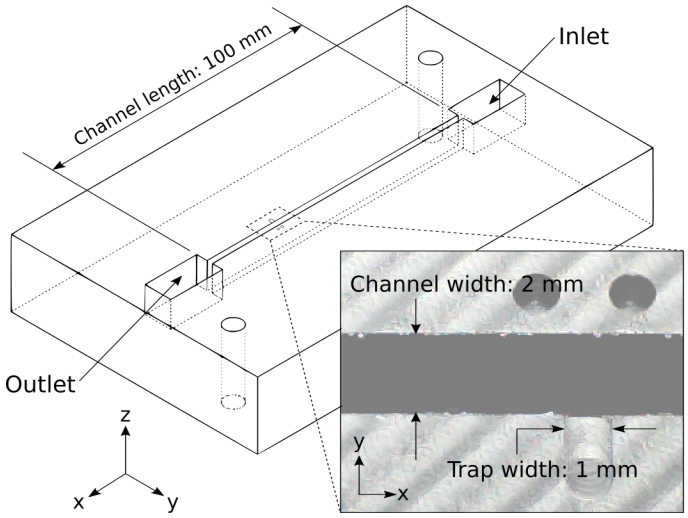

Figure 3: SolidWORKS wireframe model of device. Channel length is 100 mm, with the trapping feature positioned 90 mm from the inlet to ensure that the flow is fully developed. Inset: Field of view of camera for all experiments. The nanosheet trapping feature is shown, milled into the side of the channel. Trapping feature width is 1 mm; trapping feature depth is 100 µm, confirmed by profilometry. Channel width is 2 mm; channel depth is 10 mm.

2.2.2 Experiment methods

The device (see Figure 3) was secured to an optical breadboard (THORLABS) for all experiments. A syringe pump (Harvard Apparatus), with two 60 mL syringes filled with deionized water, was used to produce a combined flow rate of 12 mL/min (2 × 10-7 m3/s). The two syringes were connected with a T-junction, luer-lock fitting to merge the two streams. Plastic tubing with 6.35 mm outer diameter and 4.35 inner diameter was used. By using two syringes, we were able to perform six trials without refilling, using 20 mL each. The inlet tube was positioned in the device using an articulating arm. We attached one end of an outlet tube (6.35 mm outer diameter and 4.35 mm inner diameter) to the device outlet. The other end was attached to a vertically oriented (along the z-direction, as shown in

Figure 3) linear stage with coupled micrometer (THORLABS), enabling us to position the outlet tube with micrometer resolution. The water level was adjusted with the syringe pump running at the specified flow rate until there was no observed water surface deformation in the main channel. This was performed by illuminating the water surface with a white light LED lamp and observing the edges of the water channel to see if the water meniscus was convex, concave, or flat (Lee, et. al., 2019). The outlet tube was placed into a waste beaker. Water was not reused to avoid contamination. The entire experimental setup was placed inside an acrylic box to shield from ambient air currents and temperature fluctuations due to the building heating and air conditioning system.

A USB camera (Veho, VMS-004) was manually positioned with an articulating arm, 100 mm from the trap feature, and at 20 degrees from vertical to allow sufficient thin-film interference to see the nanosheets. Videos were recorded at a frame rate of 6.25 fps using the MATLAB Image Acquisition Toolbox (MATLAB 2015b). Nanosheets were cut using an ultramicrotome (Leica UC7), at 500 nm thickness, using a diamond knife (Diatome). Nanosheets were cut from an epoxy resin block (EPON 812, ρ = 1.22 g/cm3) that was trimmed manually to a cross section of roughly 1 mm x 1.5 mm. Nanosheets were transferred manually from the ultramicrotome to the device using a commercial tool (Perfect Loop, Electron Microscopy Supplies).

The Reynolds number of the main channel, Re, was calculated as

$$Re = \frac{\rho_{\text{water}} \frac{Q}{A_{\text{channel}}} R_h}{\mu}, \text{ where} \quad (1)$$

A_{channel} is the channel cross-sectional area, defined as

$$A_{\text{channel}} = w_{\text{channel}}\, d_{\text{channel}}, \tag{2}$$

ρ_{water} is the density of water at 25ºC, Q is the volumetric flow rate in the channel, $w_{channel}$ is the channel width, d_{channel} is the channel depth, R_h is the hydraulic radius, defined as

$$R_h = \frac{A_{\text{channel}}}{2d_{\text{channel}} + w_{\text{channel}}} \tag{3}$$

for open channel flow, and μ is the dynamic viscosity of water at 25ºC. With the calculated Reynolds number of the channel (Re ~ 10), we assumed primarily laminar flow. Additionally, we calculated the nanosheet Reynolds number, $Re_{\text{nanosheet}}$, to access the effect of inertial forces relative to that of viscous forces, with $Re_{\text{nanosheet}}$ defined as

$$Re_{\text{nanosheet}} = \frac{\rho_{\text{nanosheet}} \frac{Q}{A_{\text{channel}}} L_c}{\mu}, \tag{4}$$

where $\rho_{\text{nanosheet}}$ is the density of the nanosheet (ρ = 1.22 g/cm^3), Q is the volumetric flow rate in the channel, A_{channel} is the channel cross-sectional area, L_c is the nanosheet characteristic length, defined as

$$L_c = \sqrt{w^2 + l^2 + t^2} \tag{5}$$

(w, l, and t, are the width, length, and thickness of the nanosheet, respectively), and μ is the dynamic viscosity of water at 25ºC. We calculate $Re_{\text{nanosheet}} \sim 10^{-3}$, indicating inertial forces to be negligible to viscous forces exerted by the water upon the nanosheet.

Furthermore, we assessed the effects of gravity versus surface tension forces by calculating the Bond number and the effects of inertial versus surface tension forces by calculating the Weber number. The equation for the Bond number and the Weber number are

$$Bo = \frac{\Delta \rho g L_c^2}{\gamma}, \text{ and} \tag{6}$$

$$We = \frac{\Delta \rho v^2 L_c}{\gamma}, \text{ respectively} \tag{7}$$

where L_c is the nanosheet characteristic length, $\Delta\rho$ is the difference in density between the nanosheet and water at 25ºC, g is the acceleration due to gravity, v is the average fluid velocity, and γ is the surface tension coefficient of the water-air interface at 25ºC. With the calculated Bond number ($Bo \sim 10^{-2}$) and Weber number ($We \sim 10^{-10}$), we assumed gravitational forces and inertial forces on the nanosheet to be negligible relative to capillary interactions.

Prior to an experiment, a nanosheet was positioned in the flow channel at a starting position– approximately 20 mm upstream of the trap–using air puffs from a syringe with an attached, 31-gauge needle tip (Becton Dickinson). Syringe pump flow and video recording were manually initiated for each trial (i.e., a single nanosheet transport and trapping measurement). Between trials, the nanosheet was manually reset to its initial starting position using the same air-filled syringe. Trials were repeated with the same

nanosheet as many times as possible, up to ten, within one hour to minimize any effect of water evaporation. Sets of trials were performed on ten nanosheets in total. We assumed all nanosheets investigated were of the same size and did not vary significantly between trials. Additionally, we assumed that the nanosheet is neither significantly deformed nor physically changed due to the trap. Results from the trials were used to compute accuracy and repeatability of the nanosheet position in the trap and to compare with a mathematical model. For the trap, the repeatability was computed as the standard deviation of the nanosheet centroid final positions, and the accuracy was computed as the Euclidian distance between each nanosheet centroid final position and a specified reference position. Accuracy of the trap was computed relative to the trap's downstream corner, subtracting an offset of ½ of the mean nanosheet width, for each nanosheet measured.

2.2.3 Data analysis methods

Raw video files (.avi format) were imported into a custom MATLAB script. In each frame, the following basic steps were used to locate the nanosheet: video length trimming, image cropping, image binary filtering, noise removal, background subtraction, and objection detection via blob analysis. Fixed pixel count metrics were used to eliminate false-positives, and all nanosheet centroid paths were manually verified. Videos were corrected and aligned via coordinate transformations using the fiducial marks in each video.

From these videos, we obtained the nanosheet's centroid-to-trap distance over time. The x-direction, y-direction, and root-mean-square (RMS) centroid-to-trap distances were calculated as

$$\Delta x_i = |x_i - x_f|, \tag{8}$$

$$\Delta y_i = |y_i - y_f| \text{ , and} \tag{9}$$

$$r_i = \sqrt{(x_i - x_f)^2 + (y_i - y_f)^2} \text{ , respectively,} \tag{10}$$

where x_i is the current nanosheet position along the x-direction, x_f is the final nanosheet position in the x-direction, y_i is the current nanosheet position along the y-direction, and y_f is the final nanosheet position in the y-direction. For coordinate axes, see Figure 3. As a choice of convention, time, τ, is defined as

$$\tau = t_i - t_f, \tag{11}$$

where t_i is the current time and t_f is the time at which the nanosheet comes to rest. In analyzing the nanosheet centroid-to-trap distances, we decomposed the nanosheet centroid-to-trap distances into their x- and y-direction components and plotted them as a function of time. We analyzed trials that were longer than 8s; this corresponded to trials whose initial RMS centroid-to-trap distance was greater than or equal to twice the capillary length of the water-air interface. This criterion was imposed to minimize the effect of system dynamics (e.g., starting and stopping of the syringe pump). In addition, we analyzed $\Delta y > 0.42$ mm; this lower bound was obtained by multiplying the resolution limit of our camera (0.14 mm/px) by a factor of three, representing an imposed minimum signal-to-noise ratio of three.

Additionally, the mean centroid path was computed by spatially averaging centroid paths in the y-direction for each x-direction centroid coordinate. The computed mean path was compared to model results by calculating the root-mean-square (RMS) error between the predicted model path and the experimental mean path.

2.3 Theory

We hypothesize that the behavior of the nanosheet is governed by two independent forces: hydrodynamic forces far from the trap and curvature-induced capillary interactions near the trap. We note that the curvature-induced capillary interactions are based on the minimization of surface energy, and accordingly, the close-range attraction of nanosheets to the trap is driven not by gravity but rather by surface tension. As such, in our model, the forces exerted on the nanosheet via curvature-induced capillary interactions are surface tension based. In our model, we first solve two separate independent differential equations that govern the hydrodynamic and surface tension forces and then superimpose the force contributions and integrate to find the nanosheet position as a function of time.

2.3.1 Finite element method: Navier-Stokes and Young-Laplace equation solutions

We used a finite element approach to solve the two governing differential equations. The Navier-Stokes equation for hydrodynamic forces and the Young-Laplace equation for the surface tension forces are given, respectively, as

$$\rho \frac{\delta \boldsymbol{u}}{\delta t} + \rho \boldsymbol{u}(\boldsymbol{u} \cdot \nabla) - \mu \nabla^2 \boldsymbol{u} = -\nabla p + \rho \boldsymbol{g} \text{ , and} \tag{12}$$

$$\rho g h = -2\gamma H \tag{13}$$

The fluid density is given by ρ, g is the acceleration due to gravity, h is the fluid height, μ is the fluid dynamic viscosity, γ is the surface tension coefficient, and H is the mean curvature. We assume these governing equations are independent and that their respective force contributions can be superimposed. While in our Young-Laplace equation finite element solution we do not neglect hydrodynamic pressures, due to the small trap height (100 μm) relative to the capillary length of the water-air interface (~2.7mm), the hydrodynamic pressures in the Young-Laplace equation can be neglected to minimize computational costs. To solve these equations, we used a finite element software (COMSOL V5.3) using the geometry described. A 3-dimensional simulation was used for the Navier-Stokes equation to capture the entire channel volume while a 2-dimensional simulation was used for the Young-Laplace equation, simulating only the channel surface. We note that due to the laminar flow and open channel geometry in this case, the hydrodynamic model solution could be obtained using 2-dimensional, analytical methods. A 3-dimensional hydrodynamic model was used to allow ease of modeling for any design iteration.

For each differential equation, the appropriate boundary conditions were assigned to match experimental conditions. For the Navier-Stokes equation, stationary flow was assumed; inertial forces and hydrodynamic pressures were neglected. A flow-rate inlet condition and a zero-pressure outlet condition were used for the Navier-Stokes equation boundary conditions. Density and viscosity of pure water at 25°C were used. For the Young-Laplace equation, the boundary was set at a height of $h = 0$, with exception to the

device trap boundary, which was set to height of h = -100 μm. Surface tension coefficient and density of pure water at 25˚C was used. Once the initial conditions were set, the geometry mesh was automatically created by the finite element software, and the solution was obtained. The solution was obtained multiple times with refined meshes to ensure convergence of the solution. We note that the geometry mesh from the Navier-Stokes and Young-Laplace solutions did not match from the outset; therefore, the misalignment of geometry meshes needed to be reconciled during time integration (see Section 2.3.2). From the Navier-Stokes solution, we exported the 3D geometry mesh and the fluid velocity vector at each mesh node; from the Young-Laplace solution, we exported the 2D geometry mesh, the fluid height at each mesh node, and the surface gradient vector at each mesh node. These solutions were imported into a custom MATLAB script for further calculations. See Lee, et. al., 2019 for details.

2.3.2 Time integration of hydrodynamic and surface tension forces

We used a skin-drag force model as a first-order approximation of the hydrodynamic forces exerted on the nanosheet, which has x and y dimension on the order of millimeters. The skin-drag force is given by

$$\vec{F}_d = \frac{1}{2} C_f \rho A_w \left|\vec{u}_p - \vec{u}_f\right| (\vec{u}_p - \vec{u}_f) \text{ , where} \tag{14}$$

$$C_f = \frac{1.328}{\sqrt{Re}}, \text{ and} \tag{15}$$

$$Re = \frac{\rho \bar{u}_f l_c}{\mu}. \quad (16)$$

Again, ρ is the fluid density, μ is the fluid dynamic viscosity, $\vec{u}_p$ is the nanosheet velocity, $\vec{u}_f$ is the instantaneous fluid velocity, $\bar{u}_f$ is the average fluid velocity, l_c is the channel characteristic length, and A_w is the nanosheet wetted area. (Note: The equation shown for the coefficient of friction, C_f, is known as the Blasius Friction law and is applicable only in laminar flow conditions, which we impose from the outset). Also, for this calculation, we use a slightly modified form of the Reynolds number (see Eqn. 1). Due to the 2-dimensional geometry of the nanosheets, we assumed that the wetted area was equal to the area of the nanosheet, which was measured optically during experiments. The average fluid velocity and the instantaneous fluid velocity were obtained by solving the Navier-Stokes equation using the finite element method, as described previously. The drag force is calculated in a Cartesian coordinate system. As such, the individual drag force components are calculated by using the x and y components of the fluid and particle velocities.

For the surface tension forces, we used a linearly proportional model to express the surface tension force as a function of the interface height gradient, the surface tension coefficient, and the nanosheet size. To assure that surface-tension-based model was appropriate, we calculated the Bond number (see Eqn. 6). With the calculated Bond number ($Bo \sim 10^{-2}$), we assumed gravitational forces on the nanosheet to be negligible relative to surface tension forces; equivalently stated: The short-range attractive forces acting on the nanosheet are predominantly higher-order-deformation (quadrupolar or higher) interactions relative to monopole-deformation interactions.

The surface tension forces acting on the nanosheet can be written as

$$\vec{F}^{s.t.} = \oint \gamma \, \vec{e}_t \times \vec{e}_n \, dl \tag{17}$$

where $\vec{e}_t$ is the unit vector tangent to the contact line and $\vec{e}_n$ is the unit vector normal to the nanosheet surface. We observe that in Eqn. 17, the force due to surface tension exerted on the nanosheet scales with the nanosheet wetted-length (equivalently, the nanosheet-water-air contact line length). Practically, the nanosheet wetted-length is difficult to measure since the deformations that contribute to the effective wetted length are typically below the diffraction limit of light. Therefore, we derive the governing equation for curvature-induced nanosheet trapping by rewriting Eqn. 17 as

$$\vec{F}^{s.t.} = k \, \gamma \, L_c \, \nabla h \, . \tag{18}$$

The variable k is a non-dimensional scaling factor, γ is the surface tension coefficient, L_c is the nanosheet characteristic length (see Eqn. 5), and h is the water-air interface height. The surface tension coefficient of pure water at 25˚C was used. Eqn.18 was constructed using the following reasoning:

1. From Domínquez, et. al., the force exerted on a particle on a curved fluid-fluid interface is directly proportional to the gradient of the interface height.

2. From Cavallaro, et. al., the force exerted on a particle on a curved fluid-fluid interface is directly proportional to size of the particle.

3. From Stamou, et. al., the force exerted on a particle on a fluid-fluid interface is directly proportional to the interfacial surface tension coefficient.

4. The nondimensional scaling factor, *k*, was added to account for physical characteristics such as the quadrupole moment tensor, the deviatoric curvature tensor, nanosheet orientation, and constant prefactors.

It is likely the non-dimensional scaling factor, k, is a function of distance from the trap, but, we assume k is constant near the trap (<1x capillary length of water-air interface), where surface tension forces play the largest role.

By superimposing hydrodynamic forces and surface tension forces and integrating in time, we can obtain the nanosheet path as a function of time. To superimpose the force contributions, we used a Cartesian coordinate system, separated forces into their x- and y-components, and summed the respective component forces to obtain the total force in the x- and y- directions. By applying Newton's second law and dividing by the nanosheet mass, we can calculate the x- and y- direction accelerations. Subsequently, we integrate twice to obtain the nanosheet position over time. For our time integration, we used a forward Euler, adaptive time-stepping integration scheme with initial position and velocity conditions matching our experimental conditions.

At each time step, the current nanosheet position is overlaid onto the Navier-Stokes and Young-Laplace geometry meshes. To reconcile the difference in geometry meshes of the two finite element solutions, we use a distance-based weighted average to calculate the hydrodynamic and surface tensions force contributions at each time step. This process is repeated at each time-step to obtain the particle path over time. As a side note, alternatively,

due to the negligible mass of the nanosheet, the trap location and nanosheet position can be found by computing the streamlines of the velocity field.

2.3.3 Mathematical modeling of quadrupolar-monopolar interactions

From the work of Cavallaro, et. al., a quadrupole capillary deformation is produced by a cylindrical particle trapped at a fluid-fluid interface, while the capillary monopole is produced by a microfabricated micro-post, which pins the fluid-fluid interface at a particular height (Cavallaro, et. al., 2011). The interaction energy between the capillary quadrupole and monopole is given as

$$E = \gamma \nabla\nabla h_0 : \Pi \tag{19}$$

where $\nabla\nabla h_0$ is the curvature tensor of the undisturbed host interface, h_0, evaluated at the particle position, and represents contributions due to externally imposed curvature gradient. Π is the quadrupole moment tensor, which represents the contribution due to interfacial deformations resulting from the object trapped at the fluid-fluid interface. γ is the surface tension of the fluid-fluid interface.

In the case of capillary quadrupole-monopole interactions, Eqn. 19 can be simplified to

$$E(r) = -\pi\gamma H_p R_p^2 \frac{1}{r^2} \cos 2(\varphi_p - \varphi) \tag{20}$$

where r particle position, φ is the particle orientation angle, H_p is the deformation amplitude, R_p is the particle radius, and φ_p is the orientation of the quadrupolar rise axis.

The interaction force between the capillary quadrupole and monopolar can be written as

$$F = \frac{\delta E}{\delta r} = \pi\gamma H_p R_p^2 \frac{2}{r^3}\ ; \tag{21}$$

in our one-dimensional model, we assume $\varphi_p = \varphi$, resulting in the cosine term equating to one. We equate the capillary interaction force to the drag force experienced by the nanosheet, written as

$$F_{\text{capillary}} = \pi\gamma H_p R_p^2 \frac{2}{r^3} = b\frac{dr}{dt} = F_{\text{drag}}, \tag{22}$$

where b is equal to $4\pi\mu R_p$, μ is the dynamic viscosity of the fluid, and R_p is the particle radius (Saffman, 1976).

In solving the ordinary differential equation given in Eqn. 22, we are left with an explicit analytical expression of the nanosheet position, r, as a function of time, t:

$$r_{\text{model}}(t) = \left(\frac{2\gamma H_p R_p}{\mu}\right)^{\frac{1}{4}} t^{\frac{1}{4}} + c_1. \tag{23}$$

In our model, we used H_p = 50 nm. From prior work, the deformation amplitude has been shown to be roughly 10% of the particle radius for a sphere; thus in our case, we use 10% of the nanosheet thickness (Stamou, et. al., 2000). In addition, we used R_p = 500 nm for the nanosheet thickness, γ = 72 mN/m for surface tension at the water-air interface (at 25ºC), and μ = 0.89 mPa*s for the dynamic viscosity of water at 25ºC. In solving for c_1, we imposed the boundary condition $r_{model}(t = -2.0 \text{ s}) = r_{experiment}(t = -2.0 \text{ s})$; thus, for our model, c_1 = -0.304.

2.4 Results and Discussion

2.4.1 Navier-Stokes and Laplace equations-based model

I have modeled, designed, fabricated, and tested a successful device for section transport and trapping via hydrodynamic forces and capillary interactions. The device is shown below in Figure 4a. After filling the channel with water, sections were placed and flow was initiated. A typical section (red outline in Figure 4a) travels from left to right and eventually comes to rest in contact with the trap.

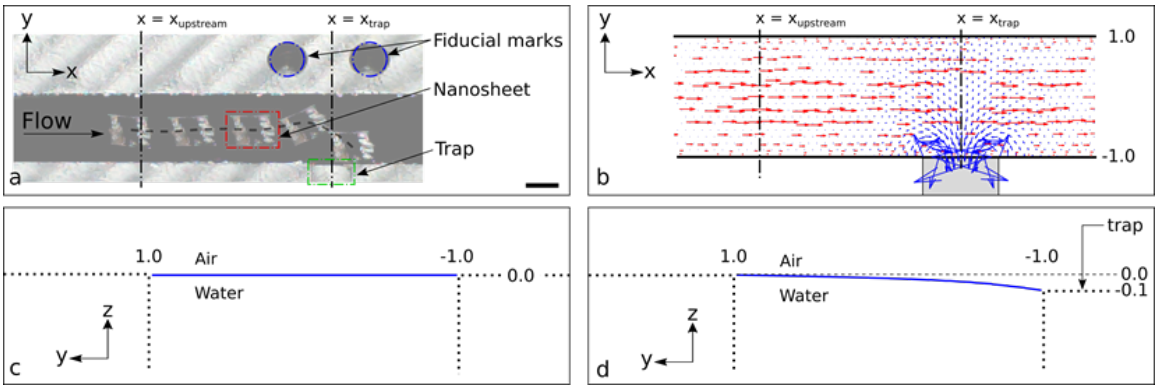

Figure 4: (a) Photograph of experimental setup showing fiducial marks (blue outline), a typical section (red outline), with superimposed photographs illustrating its trajectory (black dashed line). The section travels from left to right and eventually comes to rest in contact with the trap (green outline). Scale bar: 1 mm. (b) Modeled velocity vector field (red) and surface gradient vector field (blue). (c) Modeled result of water-air interface, shown in cross-sectional view, at $x_{upstream}$ (-10 mm relative to trap centerline). Prior to experiment, channel is filled with water to the level shown, with flat meniscus. (d) Modeled result of water-air interface, shown in cross-sectional view, at x_{trap}. The water-air interface is distorted by surface tension such that water does not enter the trap area, but rather is pinned to the wall as shown. All dimensions stated are in millimeters.

The Navier Stokes velocity vector field solution is shown in red and the Young-Laplace surface gradient vector field solution is shown in blue in Figure 4b. Based on the Young Laplace equation solution (Figure 4c), the trap creates negligible distortion in the water surface far from the trap (at $x_{upstream}$). Thus, far from the trap, the influence of the surface tension is negligible in the bulk channel, allowing for bulk transport of the section. Near the trap, surface tension forces exceed hydrodynamic forces, causing the section to migrate towards the trap (Figure 4b). Based on the Young Laplace equation solution, the water pins to the trap (Figure 4d), creating a distortion in the water surface curvature. The water, and hence the section, does not enter the 100 µm milled notch; in its final, stable location, the section is positioned with one edge mated to the channel wall. The surface

gradient is maximized at the corners of the trap, where the trap walls intersect the channel walls.

Figure 5a shows the predicted section paths for various initial positions in the y-direction, along with the overlay of Navier-Stokes solution vector field and Young-Laplace solution surface gradient vector field, to demonstrate the effect that the trap has on the bulk flow. Notably, the model shows that for starting positions equal to or greater than y = +0.2 mm, the section is not trapped. For sections that start just above the centerline (e.g., y=0 mm to +0.2 mm), the section can travel against the flow in the x-direction to be trapped. The model predicts that the sections will be trapped to the right (downstream) of the trap centerline, exactly at the corner of the trap where its wall meets the channel wall. Thus, the design gives a unique and exact trap location.

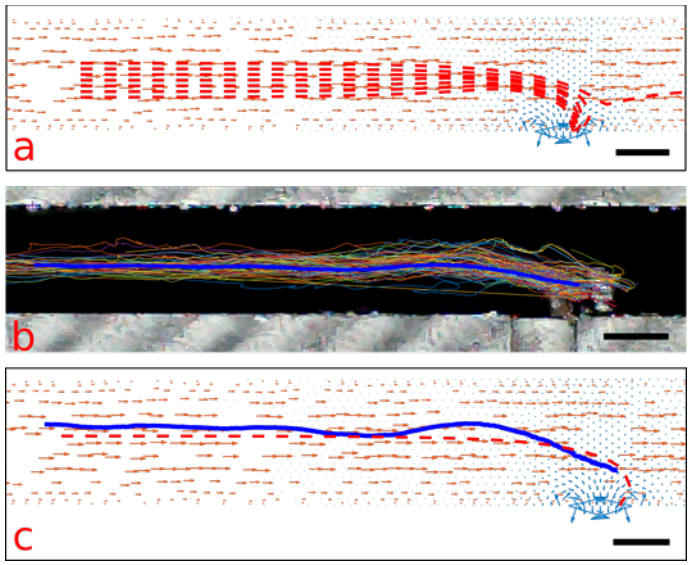

Figure 5: (a) Overlay of Navier-Stokes solution vector field, Young-Laplace solution surface gradient vector field, and modeled section paths. Initial conditions of paths range from y = +0.2 mm to y = -0.4 mm, in 0.1 mm steps, resulting in 7 paths computed (y = 0 mm at channel midline). (b) Individual experimental paths with overlaid mean experimental path (*blue*). (c) Mean experimental path plotted alongside model (initial condition y = 0.1 mm). Scale bar: 1 mm.

In total, 94 individual trials were recorded using 10 sections of thickness 500 nm. For most experiments, 10 trials were possible during the one-hour evaporation limit (7 out of 10 experiments). In all 94 trials, the sections were trapped successfully. Also, in all but 1 of the 94 trials, the long edge (~1.5 mm) of the section was trapped along the channel wall. These trials are shown as the superposition of the centroid paths in Figure 5b, along with the mean centroid path (blue). Individual experimental centroid paths occasionally demonstrated travel in the direction opposite of flow as shown in Fig. 3b, as predicted by the model.

The mean centroid path and the best-fit modeled path are depicted in Figure 5c. I found that a model starting position of y = 0.03 mm minimizes the RMS error between the

modeled path and mean experimental path. The resulting RMS error was 134 μm. This model shows good alignment with the experimental path, correctly predicting that the section comes to rest to the right of the trap centerline.

2.4.2 Device accuracy and repeatability

The final centroid position of all 94 sections is shown in Figure 6. The repeatability is the standard deviation of the centroid positions. I computed this for all 94 trials in both the x-direction and y-direction. The repeatability was 350 μm in the x-direction and 224 μm in the y-direction. I posit that the repeatability is better in the y-direction because the sections are reliably constrained by the channel wall. Small rotation differences of the sections at the trap between trials affect repeatability adversely.

Within each set of trials, I also calculated the standard deviation of the centroid position, and computed an average standard deviation, weighted by the number of trials per set of trials. With this method, I computed a repeatability of 150 μm and 120 μm in the x- and y-direction, respectively. Thus intra-set repeatability (with the same section) is greater than inter-set repeatability (using different sections). In fact, some sections exhibited repeatability as low as ~3% of their length. Thus, I posit that the manner in which the water pins to each section may vary between sections but does not change between trials for a section, attributable to variations during the fabrication process or inhomogeneity in the bulk resin block from which sections are cut.

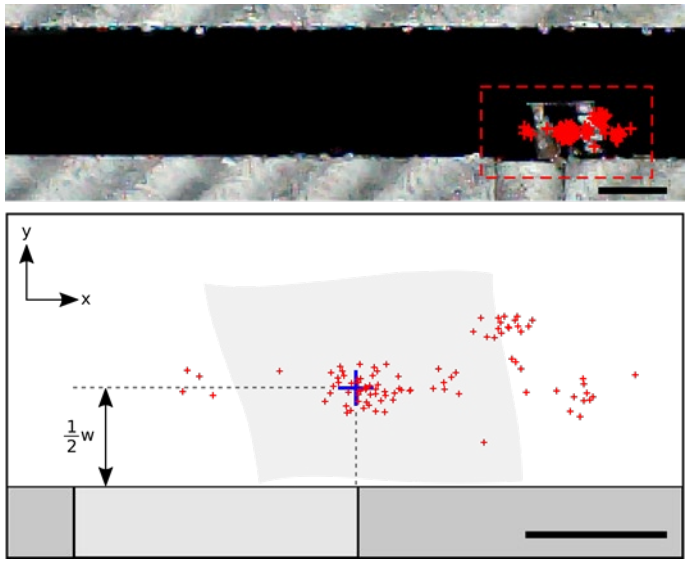

Figure 6: (top) Photograph of the device showing trapped section centroids for all trials, n = 94 (red). Detailed view (bottom) shows the distribution of the centroids. The blue crosshair indicates the desired centroid position, which is aligned with the corner of the trap in the x-direction and offset half a section's width from the trap wall in the y-direction, as shown. Scale bars: (top) 1 mm (bottom) 500 µm.

The average accuracy was 300 µm in the x-direction and 200 µm in the y-direction. While the model predicts that the sections will be trapped at the corner of the trap, where its wall meets the channel wall, I must necessarily offset the target by the width (the short edge, ~1 mm wide) of each section (See Figure 6, blue cross-hair). The accuracy of the device may be limited by several factors, such as model imperfections and the out of plane stiffness of the section counteracting the surface energy of the water, thus moving the centroid from its ideal position. The accuracy and repeatability of this device exceeds that required for mounting a section onto a copper transmission electron microscopy grid with 1 mm x 2 mm aperture, a common inspection technique following fabrication. Beyond engineering applications, this technology may have relevance for biological applications, such as serial section electron microscopy-based tomography, array tomography, or x-ray

microscopy, all of which require the manipulation of nano- to micro-scale thickness slices of biological tissue in preparation for analysis (Micheva, et. al., 2007, Bock, et. al., 2011, Dyer, et. al., 2017).

During trials, I found that sections exhibited rotation as well as translation. We observed, in all but one trial, the nanosheet's long edge (~1.5 mm) came to rest against the channel wall, indicating our device's ability to orient the nanosheets. The model, which assumes a point-mass for our section, does not capture the physical size of the section. Therefore, future work may incorporate the size of the section to account for rotation as well as translation.

I found that in our model, for initial conditions in the y-direction greater than or equal to 0.2 mm, the section failed to be trapped. From my experiments, I did not experience section trapping failure. Accordingly, in addition to the modeling improvements, I could investigate further considerations to improve the accuracy of our model such as including section physical size and bending energy.

For my experiments, all section were cut from a single EPON epoxy resin block. Further testing may involve modulating the density of the section to see its influence on the behavior of the section within our device. Similar testing may be performed by modulating the fluid of choice to change the surface tension coefficient to investigate the role of surface tension in this system.

From early experiments, we found that we could trap thinner nanosheets, but the time required for these nanosheets to pin to the trap was very long (on the order of tens of minutes). From these preliminary results, we surmise there exists a relationship between nanosheet thickness and trapping time. For 500 nm-thick nanosheets used in this work, our

throughput was one section transported and trapped every 23 seconds on average with a standard deviation of 16 seconds. Further testing may be conducted to see the trapping limits of this device with respect to section thickness. I acknowledge that 500 nm-thick sections are too thick in many applications; therefore, further device iteration is necessary to lower the section trapping thickness by an order of magnitude. This may entail microfabrication device to fabricated traps with nanometer-scale notches. This does not represent a fundamental limitation to this method, but pragmatically, the trapping of thinner nanosheets, e.g., ~10 nm, may require the composition of additional methods in addition to curvature-induced quadrupolar capillary interactions.

The trap was designed such that the size of the trap (in in-plane dimensions) was roughly the same size of the section itself. This was chosen to magnify the effect of surface tension relative to hydrodynamic forces, given that that the hydrodynamic forces scale with the section's area while surface tension forces scale with the section's characteristic length. Further testing might investigate the behavior of sections given larger trap sizes. Based on preliminary testing, I hypothesize that this phenomenon is dependent upon the section being roughly the same size as the trap.

2.4.3 Multipole interaction analysis

To determine the transportation mechanisms along the channel and into the trap, we analyzed individual nanosheet trajectories. A typical nanosheet trajectory from a single trial is shown in Figure 7a. Of the 94 trials, 48 of the trials fulfilled our criteria for further trajectory analysis (see Section 2.2.3 for details).

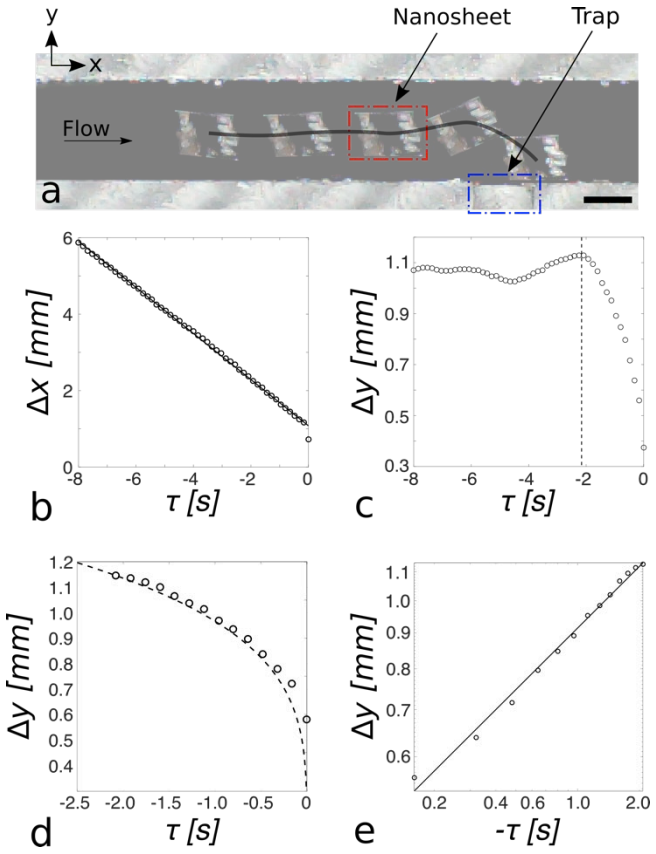

Figure 7: (a) A typical nanosheet trajectory is shown (*black line*). A nanosheet (*red outline*) travels downstream (positive x-direction) towards the trap (*blue outline*). As the nanosheet approaches the trap, it is attracted towards the trap and comes to rest with one edge mated against the channel wall. Scale bar: 1 mm. (b) Mean (n=48 trials) x-direction nanosheet centroid-to-trap distance plotted as a function of time (*black circles*) with linear regression line overlaid (*solid black line*). The x-direction centroid-to-trap distance is linear as a function of time (r^2 = 0.99), indicating steady-state hydrodynamic transport. (c) Mean (n=48 trials) y-direction nanosheet centroid-to-trap distance plotted as a function of time (*black circles*). The black dashed line indicates the time at which the nanosheet RMS centroid-to-trap distance is equal to the capillary length of water (2.7 mm). (d) Experimental, mean (n = 48), y-direction centroid-to-trap distance plotted as a function of time (*black circles*) after the nanosheet is within one capillary length of the trap with overlaid mathematical model (*dashed black line*), root mean square error (RMSE), 0.28 mm. The experiment data shows good alignment with a mathematical quadrupole-monopole capillary interaction model. (e) y-direction centroid-to-trap distance plotted vs. time on a log-log scale (*black circles*), with overlaid linear regression line (*solid black line*, α = 0.29, r^2 = 0.99). The nanosheet's y-direction centroid-to-trap distance as a function of time is well described by a power law (i.e., $y \sim t^{\alpha}$), with α = 0.29, indicating trapping of nanosheets via capillary quadrupolar interactions.

We first examined the x-direction behavior. The x-direction centroid-to-trap distance as a function of time is shown in Figure 7b (*black circles*), with an overlaid linear regression line (*black line*, slope = -0.6 mm/s, $r^2 = 0.99$). The x-direction centroid-to-trap distance is linear with respect to time, indicating steady-state hydrodynamic transport. The y-direction centroid-to-trap distance as a function of time is shown in Figure 7c (*black circles*). The black dashed line indicates the time at which the RMS centroid-to-trap distance (see Eqn. 10) is equal to the capillary length of the water-air interface (2.7 mm), which we define as t_{CL}. We observe far from the trap, the y-direction centroid-to-trap distance remains relatively constant, indicating that only hydrodynamic transport in the x-direction is occurring. To the right of the black dashed line (i.e., $\tau > t_{CL}$), the y-direction centroid-to-trap distance rapidly decreases until the nanosheet comes to rest, at time $\tau = 0$s. The shape of this decline is non-linear, as shown in Figure 7d (*black circles*), giving evidence that another force is responsible for the trapping of the nanosheets. Prior literature discussing micro-particle self-assembly via capillary quadrupolar interactions found that the particle's position, r, as a function of time, t, is well described by the power law $r \sim t^{1/4}$ (Cavallaro, et. al., 2011). Therefore, we extended the prior analytical model of capillary quadrupole-monopole interactions to our geometry and studied the effects of capillary multipole interactions on the nanosheets (Loudet, et. al., 2005, Cavallaro, et. al., 2011).

We find good alignment (RMSE = 0.28 mm) between our mathematical model (Figure 7d, dashed black line) and experiment data (Figure 7d, black circles) without any fitted parameters; suggesting that the behavior of the nanosheets is governed by capillary quadrupole-monopole interactions. Small discrepancies between our mathematical model

and the experimental data may be explained by variation in the deformation amplitude, variation in the effective particle radius, or rotational effects.

For further investigation, the y-direction centroid-to-trap distance as a function of time for $\tau > t_{CL}$ was plotted on a log-log scale (black circles), as shown in Figure 7e. The best-fit line is plotted on top of the data (solid black line). From the linear regression model, we report an ordinary r-squared value of 0.99 and slope, α, of 0.29. Our measured power-law model exponent ($\alpha = 0.29$) is consistent with previously reported values for capillary quadrupolar interactions, as opposed to monopolar interactions, which would have an expected exponent of ~0.5 (Bowden, et. al., 2001, Loudet, et. al., 2005, Vella & Mahadevan, 2005, Dominguez, et. al., 2008, Cavallaro, et. al., 2011).

Interestingly, despite the large characteristic length of the nanosheets relative to the capillary length, capillary quadrupolar interactions remain the dominant capillary multipole interaction. This finding is contrary to prior work investigating large objects trapped at a fluid-fluid interface, which typically interact via capillary monopolar interactions (Bowden, et. al., 2001, Vella & Mahadevan, 2005, Dominguez, et. al., 2008). However, while our nanosheets may be large in lateral dimensions, they exhibit a small Bond number ($Bo \sim 10^{-2}$). Therefore it is not entirely unexpected for capillary monopole interactions to be negligible.

The mechanism by which the nanosheets create a capillary quadrupolar deformation remains an open question. For nanosheets to create a capillary quadrupolar deformation via their geometry, as in the case of cylindrical micro-particles, significant distortion in the water-air interface as well as bending in the nanosheet would be required. Thus, due to their thickness, it is likely an undulated contact line, or an “irregular

meniscus," with a dominant quadrupole term that manifests the capillary quadrupole deformation (Stamou, et. al., 2000).

In Figure 7b, the x-direction centroid-to-trap distance versus time for $\tau > t_{CL}$ does not appear to deviate from its linear relationship. This gives evidence that the hydrodynamic forces and curvature-induced capillary quadrupolar interactions are acting independent from one another and that their effects may be linearly superimposed.

While a power-law model fits our data, there is a small discrepancy between our reported power-law model exponent and that of published literature. We assert this difference may be explained by the different experimental conditions: Prior literature investigated the attraction of two micro-scale particles, moving towards one another in one-dimension without rotation. In our system, the nanosheets are attracted towards a fixed trap, are moving in two-dimensions, and are free to rotate. Additionally, we acknowledge 46 of the 94 trials were not included in our trajectory analysis due to our stated criteria but, in all 94 trials, the nanosheets were transported and trapped. Therefore, we do not expect a different rationale for the observed behavior in these trials.

2.4.4 Nanosheet trapping stability

To analyze nanosheet trapping stability within our device, we first generated a stability diagram in terms of a dimensionless grouping, the capillary number (*Ca*), shown in Figure 8.

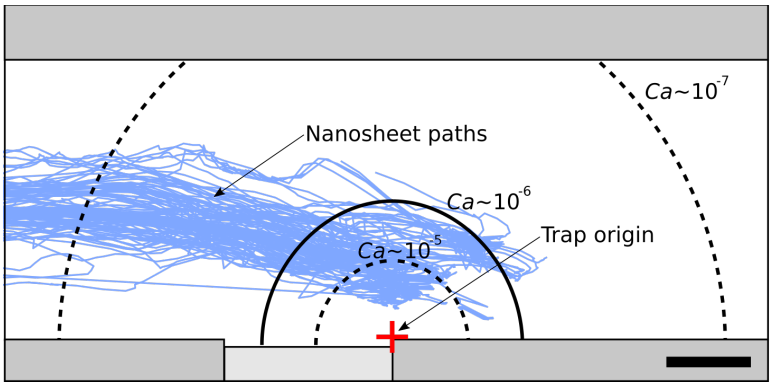

Figure 8: Diagram of stable trapping regions as a function of the capillary number, *Ca*, with overlaid nanosheet paths (*solid blue lines,* n = 94). The stability regions are shown with respect to our trap origin (*red crosshair*), defined as the right edge of the trap where the water and channel wall meet. Our system, which has *Ca* ~ 10^{-6}, contains a stable trapping region with a calculated maximum radius (r_{max}) of 1.2 mm (*solid black line*). Lowering *Ca* by an order of magnitude results in r_{max} = 2.5 mm (*outer, black dashed line*) while increasing *Ca* by an order of magnitude results in r_{max} = 0.5 mm (*inner, black dashed line*). Scale bar: 500 µm.

In expressing the nanosheet position as a function of the capillary number ($Ca = \mu v/\gamma$), Eqn. 22 can be written as

$$\frac{H_p R_p}{2r_{\max}^3} = Ca = \frac{\mu v}{\gamma}, \tag{24}$$

using values for H_p, R_p, μ, and γ previously given, and v, the average fluid velocity, equal to 0.6 mm/s, taken from the slope of the x-direction centroid-to-trap distance as a function of time plot in Figure 7b. Using these values, we report $Ca = 7.42 \times 10^{-6}$. The small capillary number gives evidence that surface tension forces play a much larger role in the transport of the nanosheet, resulting in nanosheet trapping. Further experiments could be performed by modulating capillary number to access trapping behavior: it is likely that, as the capillary number approaches unity, the efficiency of this trap would decrease.

In Eqn. 24, we replace the nanosheet position, r, with r_{max} since this equation represents the maximum distance at which trapping will occur. We measure r_{max} relative to the right edge of the trap, where the water and channel wall meet (Figure 8, *red crosshair*), since the interaction energy is maximized at this location (see Eqn. 20). Thus, in solving for r_{max}, we are able to show "stability regions" (defined mathematically as $0 < r(t) < r_{max}$), i.e., areas where a nanosheet would be successfully pulled towards and come to rest at the trap. We see that in Eqn. 24, $r_{max}^3 \sim Ca$, indicating that relatively small changes in the capillary number result in large changes in r_{max}.

For our system, using Eqn. 24 to solve for r_{max}, we obtain r_{max} = 1.19 mm. This stability region is outlined in Figure 8 (*solid black line*). Interestingly, we find this value aligns well with the mean y-direction centroid-to-trap distance at which the RMS centroid-to-trap distance is equal to the capillary length of the water-air interface (Figure 8, *black dashed line*). At this distance, the edge of the nanosheet interacts with the capillary monopole created by the trap, thereby attracting the nanosheet. We see that for our device, all nanosheet paths (Figure 8, *solid blue lines*, n = 94) cross the calculated r_{max} threshold and subsequently are trapped, as predicted. Given that the stability region is radially symmetric, it is possible for nanosheets to overshoot the trap in the x-direction and still be trapped as long as the nanosheet is within the stable region, as we observe in some of the nanosheet paths.

Furthermore, we mathematically modulate the capillary number to observe how the stability region changes. Experimentally, these changes in capillary number could be accomplished by varying the fluid velocity, the fluid dynamic viscosity, and/or the surface tension coefficient. Increasing the capillary number by an order of magnitude results in

r_{max} = 0.55 mm (Figure 8, *inner dashed black line*); a dramatically smaller trapping region. In contrast, decreasing the capillary number by an order of magnitude results in r_{max} = 2.56 mm (Figure 8, *outer dashed black line*), which would encapsulate the entire channel width. While encompassing the entire channel width may guarantee nanosheet trapping, there may be negative trade-offs. For example, lowering the fluid velocity would increase trapping time, and changing the surface tension coefficient or the fluid viscosities could introduce fluids that are chemically incompatible with the nanosheet. As encapsulated in Eqn. 24, changing the object of interest would change H_p and R_p, thereby affecting r_{max}. Future experiment could be conducted to investigate stability regions for other objects.

While multi-nanosheet experiments are beyond the scope of this work, we postulate developing a multiplexed device that incorporates our findings here, is possible. Future work may investigate a single-fluid device that modulates the fluid velocity via channel stenosis; thereby locally changing the capillary number to switch between trapping stability regimes. Further investigation would be needed to study the effects of multi-body interactions.

The interaction between two nanosheets remains unclear, particularly if one is already trapped and the other is freely moving. We speculate that multi-nanosheet interactions are likely capillary quadrupole-quadrupole interactions, as opposed to the capillary quadrupole-monopole interaction we observe between the nanosheet and the trap. From prior literature, capillary quadrupole-quadrupole interactions have lower interactions energy than that of monopole-monopole interactions. Therefore, it is plausible that the trap acts in a binary fashion: when unoccupied by a nanosheet, it will attract any nanosheet within its stability region via capillary quadrupole-monopole interactions. When occupied,

the nanosheet becomes the interacting body since it is physically blocking the trap, thus lowering the interaction energy (Kralchevsky, et. al., 2001, Bowden, et. al., 2001). If the capillary number is tuned properly, the approaching nanosheet could pass the trapped nanosheet and continue further downstream.

2.5 Conclusion

Expanding upon prior particle transport and trapping methods, we demonstrate that hydrodynamic forces in conjunction with capillary quadrupolar-monopolar interactions can be used for long-range transport (>1x capillary length) and accurate and repeatable trapping, respectively, for nanosheets on the water-air interface. Capillary quadrupolar interactions have been shown to manifest on nanoscale colloidal particles while capillary monopolar interactions have been observed for millimeter-scale particle interactions; therefore, it remains unknown how nanosheets, which feature millimeter-scale in-plane dimensions and nanoscale thicknesses, interact with their surroundings on the water-air interface. We confirm via mathematical modeling and experiment that nanosheets interact via capillary quadrupolar interactions. Furthermore, we demonstrate that our hybridized methodology enables the controlled manipulation of nanosheets on a water-air interface over distances greater than those of methods solely using capillary multipole interactions. In quantifying our device, we show that the accuracy and repeatability of this device exceeds that required for mounting a nanosheet onto a transmission electron microscopy grid, a common inspection technique following nanosheet fabrication. We envisage our methodology to be used in conjunction with techniques for functional nanosheet fabrication—which are typically created on a water-air interface—to enable accurate and repeatable device integration and manufacturing. Additionally, this technology may have

relevance for biological applications, such as serial section electron microscopy-based tomography, array tomography, or x-ray microscopy, all of which require the manipulation of nano- to micro-scale thickness slices of biological tissue on a water-air interface in preparation for ultrastructural analysis. From our stability diagram, we show the trapping stability is dependent upon the capillary number; moving forward, device multiplexing via capillary number modulation could be used to facilitate high-throughput nanosheet manipulation. Ultimately, this device demonstrates an application of capillary quadrupolar interactions in conjunction with hydrodynamic forces to overcome the challenge of nanosheet manipulation, an important problem in the fields of nanotechnology, biosciences, and material science.

CHAPTER 3. DESIGN, IMPLEMENTATION, AND CHARACTERIZATION OF BATCH PROCESSING FOR SERIAL SECTIONING

3.1 Introduction

Serial section transmission electron microscopy (ssTEM) is the most promising tool for investigating the three-dimensional structure of the brain with nanometer-scale resolution (Kornfeld & Denk, 2018, Gay & Anderson, 1954, Briggman & Bock, 2012). In recent years, ssTEM studies have provided significant insight into the physiology and neuroanatomy of mammalian and non-mammalian nervous systems with resolution and scope previously not possible (Bumbarger, et. al., 2013, Lee, et. al., 2016, Zheng, et. al., 2017), (respectively, references I, L, M in Figure 9]. From published ssTEM literature, we observe a general trend of increasing neural tissue volume studied over time, exemplifying the scientific interest in the field to study larger and larger volumes of neural tissue, as shown in Fig 1. Yet, a significant challenge remains in the *scalability* of ssTEM. As the volume of brain tissue to be studied grows larger, does ssTEM remain a viable technology in terms of yield, cost, and throughput?

Currently, the ssTEM workflow is composed of four primary steps: (1) bulk tissue processing, (2) serial sectioning, (3) post-staining, (4) TEM imaging, and (5) image segmentation. In recent years, significant advances in bulk tissue processing, post-staining,TEM imaging, and image segmentation have shown the potential scalability of ssTEM (Bock, et. al., 2011, Reid, 2012, Hua, et. al., 2015, Lee, et. al., 2016, Lee, et. al., 2017). In contrast, traditional techniques and methods for serial sectioning for ssTEM have

remained unchanged for nearly 60 years (Dowell, 1959, Harris, et. al., 2006). A recent advancement in serial sectioning technology, called the Automatic Tape-collecting Lathe Ultramicrotome (ATLUM), shows promise for the automation of serial sectioning, but demonstration and characterization for neuroanatomical ssTEM studies remains to be shown (Hayworth, et. al., 2006, Kasturi, et. al., 14). Accordingly, advances in methods for serial sectioning will be necessary for the scalability of ssTEM.

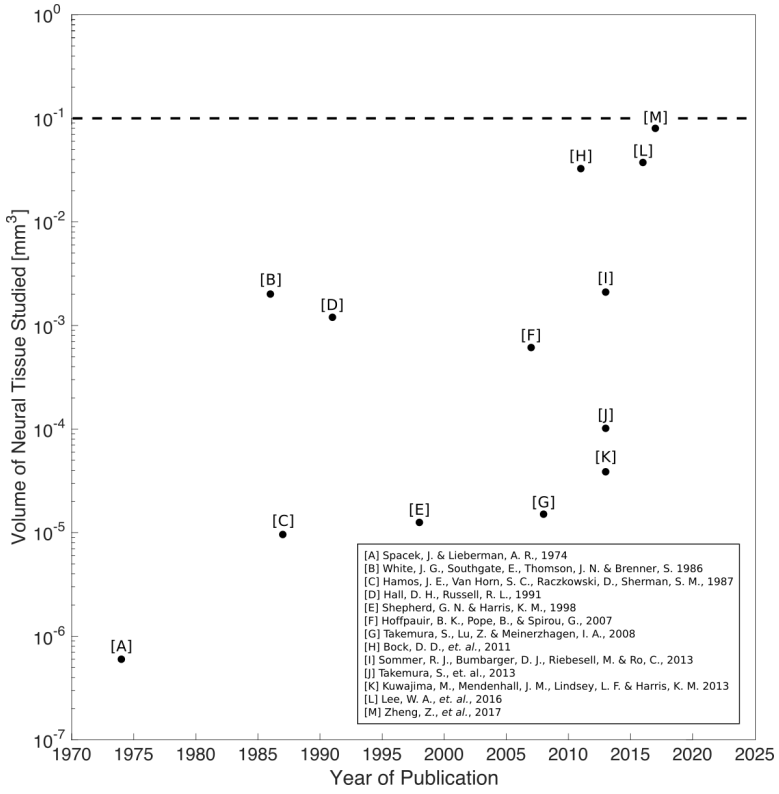

Figure 9: Volume of neural tissue in ssTEM studies versus publication year. Each data point represents one journal publication that used ssTEM for neuroanatomical studies. We observe the general trend of increasing neural tissue volume studied over time. The largest neuroanatomical ssTEM study (reference [M], Zheng, Z., *et. al.*, 2017) to date remains an order of magnitude below a cubic millimeter.

In traditional serial sectioning, an ultrathin (< 40 nm) brain slice (or "section") is cut with a diamond knife into an attached water reservoir, i.e., "waterboat" (see Figure 10.). A detailed discussion of traditional serial sectioning is given in Section 1.1.2. Individual sections are typically ultrathin in order to have sufficient out-of-plane resolution during EM tomography. Once cut, the section is suspended on and then transported (e.g., by manually whisking the water's surface with an eyelash) on the water's surface to a suitable pickup location (Harris, et. al., 2006). Subsequently, the section is carefully picked up by hand and placed onto a TEM substrate (e.g., copper, plastic-coated slot-grid), paying close attention to align the section with the substrate aperture (see Harris, et. al., 2006 for further details on traditional serial sectioning methodology.) Thus, for traditional serial sectioning, the manual pickup of sections must be repeated for each section without error. From prior work, experienced investigators typically experience 1-3% section loss; with regards to cost, each TEM grid costs ~40 cents; with regards to throughput; each cycle of ultrathin sectioning—transporting, picking up, and placing the section—takes approximately 2 min (Harris, et. al., 2006, Bock, et. al., 2011, Bumbarger, et. al., 2013, Lee, et. al., 2016). While these metrics on a section-by-section basis may seem reasonable, it is the multiplication (or "scaling") of these values by tens of thousands of serial sections that prohibits large ssTEM neuroanatomical studies.

In the field of industrial engineering, batch processing, i.e., the production of goods in quantized groupings (or "batches"), is a common methodology for yield, cost, and throughput optimization for scaling manufacturing processes (Womack, et. al., 1990, Lee & Uzsoy, 1999, Melouk, et. al., 2004, Mendez, et. al., 2006). First introduced by the Toyota Motor Company in the late 1930's to compete with continuous processing methods (e.g.,

the assembly line), batch processing enables high-yield, low-cost, high-throughput production (Womack, et. al., 1990). We set out to explore whether batch processing may be an effective methodology for scaling serial sectioning for large neuroanatomical ssTEM studies.

We introduce conceptually, experimentally, and mathematically an alternative method for large-scale serial sectioning, termed Loop-based, Automated Serial Sectioning Operation (LASSO). In our methodology, individual sections are picked up from the waterboat and placed onto TEM substrates using robotic tools for accurate and repeatable, rapid serial sectioning. Batches of sections are placed onto custom microfabricated substrates, reducing overall handling and imaging time of sections. In total, we present a flexible, scalable, and accessible technology platform for serial sectioning to enable the next generation of large-scale neuroanatomical ssTEM studies.

3.1.1 A brief history of batch processing

Prior to batch processing in the automotive industry, continuous processing was the dominant manufacturing modality, championed by Henry Ford and The Ford Company. While continuous processing led to the Ford Company's domination in the automotive industry in the early 1900's, it was quickly outpaced by The Toyota Corporation's development of batch processing in the post-WWII era of Japanese re-industrialization (Womack, et. al., 1990). This was predominantly due to two reasons: scalability and error-reduction. While continuous manufacturing was great at producing automobiles in large quantities at a high throughput, this was at the cost of many unused, out-of-specification car parts. Additionally, any fault or error in the production line would lead to cascading errors downstream within the production line and eventual shut-down of the entire

production line to fix any errors (Womack, et. al., 1990). On the other hand, in batch processing, parts are manufactured in small groupings, called batches. With each batch, individual parts are assessed for quality and adjustments are made to the manufacturing process to ensure high-yield. Due to batch processing, we observe the steady increase in Toyota's domination in the automobile industry from the 1950's to modern day (Womack et. al., 1990). It was their breaking from continuous mass manufacturing and decision to manufacture small batches of cars at a time; this enabled high quality car production with minimal reductions in throughput.

3.1.2 Manufacturing and serial sectioning

While manufacturing and serial sectioning may not seem outright related, in the following, we discuss their intrinsic similarity and why significant insight may be gleaned by observing and applying insights uncovered in the field of manufacturing.

Consider the following extreme manufacturing processing: assembly line manufacturing and artisan manufacturing. In assembly-line manufacturing, i.e., continuous processing, parts are fabricated rapidly and inexpensively but with minimal quality control. Defects often occur in large quantities before the manufacturing process can be adjusted and corrected. In short, cost and throughput are optimized, but as a result, yield is negatively impacted. On the other hand, artisan manufacturing entails the fabrication of a small number of parts, but each part is carefully crafted; yield, in this case, is optimized, while throughput and cost are adversely affected. To date, the field of ssTEM has evolved along the lines of artisan manufacturing with adept scientists picking up each section and placing them carefully onto a grid with significant care and effort. While these superhuman efforts have led to remarkable feats in the field of neuroanatomy (most recently, the

complete mapping of the drosophila nervous system (Zheng, et. al., 2017), grid-based serial sectioning methods are untenable for millimeter-scale neuroanatomical studies.

Therefore, in drawing inspiration from the field of manufacturing and applying batch processing to serial sectioning, i.e., the rapid processing of individual sections and placement of non-consecutive sections onto separate substrates, we can enable cost-effective, scalable, high-yield, high-throughput serial sectioning for millimeter-scale connectomics.

3.2 Methodology

During section processing, sections must be (1) placed accurately and repeatably, avoiding misplacement of sections over non-electron transparent regions of the substrate, (2) transported, picked up, and placed without damaging the section (i.e., avoiding folds, cracks, wrinkles), and (3) placed onto the TEM substrate without breaking the substrate aperture support film, as previously discussed in Section 1.1.2. For these reasons, great dexterity and mental acumen is required for the processing of serial sections (Williams and Kallman, 1955, Harris, et. al., 2006). The implementation of a batch process may enable reliable section processing: the accurate and repeatable processing of tens of thousands of serial sections without consecutive section loss.

3.2.1 Strategy for batch processing of serial sections

In LASSO, sections are cut on a conventional ultramicrotome with a diamond knife into an adjoining waterboat, as depicted in Figure 10b. From the waterboat, sections are picked up using a loop end-effector, controlled by three orthogonal linear actuators. Held in place by water surface tension forces within the loop (Figure 10b, inset, top right), the

sections are placed onto a microfabricated silicon/silicon nitride TEM substrate (Figure 10b, inset, bottom right). Each substrate holds more than one section with each section having its own imaging aperture. A set of substrates composes a "batch," (e.g., 4 substrates = 1 batch, as shown in Figure 10b, inset, bottom right). Immediately consecutive sections (i.e., section n and n+1) are never placed on the same substrate; therefore, the probability of consecutive section loss is minimized.

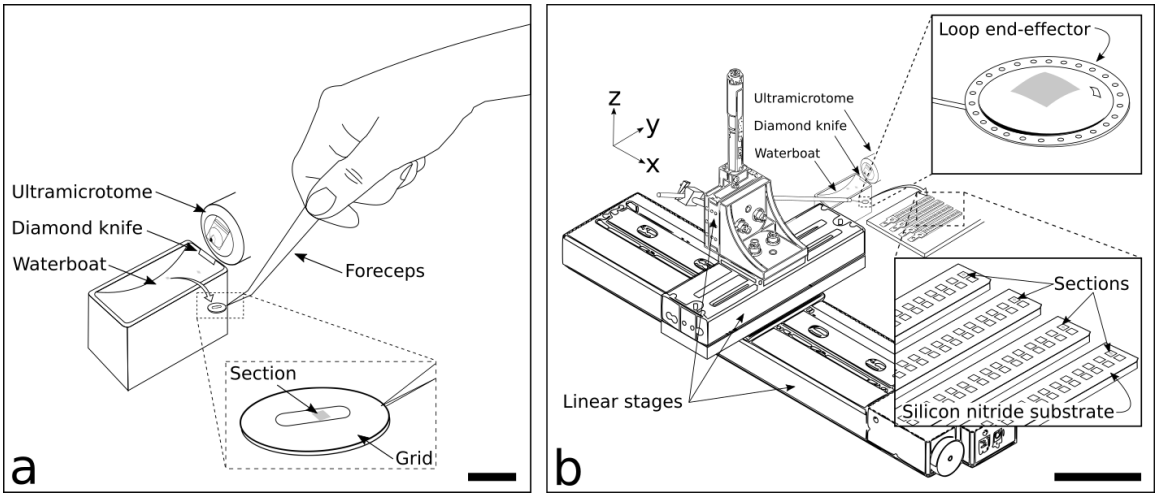

Figure 10: Traditional serial sectioning (*left*) as compared to LASSO (*right*). (a). Sections are cut on an ultramicrotome using a diamond knife and slide into an adjoining water-filled waterboat, where they float on the water surface. Using a TEM grid held by forceps, a skilled user picks up section(s) from the waterboat onto a TEM substrate, e.g., grid (*Fig 10a, inset*). Scale bar: 10 mm. (b) For LASSO, sections are fabricated in an identical manner as in Fig 10a, using the same ultramicrotome, diamond knife, and waterboat. From the waterboat, sections are picked up using a loop end-effector, actuated via a robotic system composed of three orthogonal linear axes. Held in the loop end-effector by surface tensions forces (*Fig 10b, inset, top right*), the section is placed onto microfabricated silicon nitride substrates (*Fig 10b, inset, bottom right*). Multiple sections are placed onto the same substrate, with each section having its own imaging aperture; a set of substrates compose a "batch," (e.g., 4 substrates = 1 batch, as shown in Fig 10b, inset, bottom right). Scale bar: 100 mm.

3.2.2 Design and manufacturing of microfabricated TEM substrates

3.2.2.1 Advantages of microfabricated TEM substrates

Manual methodologies for electron transparent films do not provide the repeatability and resolution in film thickness and mechanical strength achievable with modern micro-manufacturing processes (e.g., chemical vapor deposition, atomic layer deposition) (Revell, et al., 1955, Rowley and Moran, 1975). Sections and traditional substrate support films are known to degrade when exposed to the electron beam (Williams and Kallman, 1955). In addition, sections can be lost when support films break during imaging (Bock, et al., 2011, Takemura, et. al., 2013, Lee, et. al., 2016, Zheng, et. al., 2017). Recent applications of semiconductor manufacturing techniques for the fabrication of electron microscopy substrates have shown to produce high strength, electron transparent substrates with accuracy and repeatability (Nishiyama, et al., 2010, Ring, et al., 2011). While these substrates have not been tested for tens of thousands of sections, microfabricated support films hold promise to significantly reduce section loss during section processing and imaging.

In addition, slight modification of a transmission electron microscope, as performed by Bock, et. al. 2011 and Zheng, et. al., 2017, can allow for substrates with larger numbers of sections to be placed within the TEM. The loading of more sections within the electron microscope per imaging session can significantly reduce the total vacuum pump-down time associated with the exchange of TEM substrates. With traditional grids, at most two, 1 mm x 1 mm sections could be placed on one grid (assuming perfect placement); this would require 12,500 pump-down cycles to fully image a cubic millimeter of brain tissue. (1 mm3 = 25,000 40-nm sections; 25,000 sections / (2 sections/imaging run) = 12,500). Even with a load-lock, the exchange of samples would require roughly 5 minutes per imaging run—

when performed 12,500 this equates to over 1,000 hours of pump-down time. Microfabrication of substrates offers increased packing density of sections on substrates to significant reduce the total microscope pump-down time. Additionally, substrate apertures can be fabricated to accommodate larger sections as well as mitigate section placement errors, thereby eliminating misplacement of sections over the TEM substrate aperture.

3.2.2.2 Design of microfabricated TEM substrates

During the design process, substrates must be optimized for section packing density, aperture imaging quality, imaging exposure time, and ease of handling. The strength of the films can be tested with a load cell or with atomic force microscopy, comparing the maximum load capacities for the microfabricated substrates and that of TEM grids. The aperture image quality can be accessed with transmission electron micrographs; frequency analysis can be used to access for background noise in the substrate and compared to that of traditional plastic thin films. Imaging exposure time experiments in the TEM can be used to compare maximum imaging times. Substrate manufacturing processes can be scaled to accommodate high-throughput imaging, moving towards a "consumable substrate" workflow model. Substrates ideally should be designed to interface with existing TEM specimen holders and to minimize step-and-settle time between individual section image acquisitions. As a major geometric constraint, the substrates must be designed to fit within the TEM pole piece aperture, which is typically ~1 cm in width and height. Additionally, a cost analysis should be used to compare the cost of traditional substrate with that of microfabricated substrates. Surface modification of the TEM substrate can be investigated for potential increased accuracy and repeatability in placement of serial sections, e.g., metal evaporation.

3.2.2.3 Manufacturing of microfabricated TEM substrates

The final substrate design was manufactured using conventional semiconductor processing techniques, outlined below in Fig 11. A detailed fabrication plan is given in Appendix B.

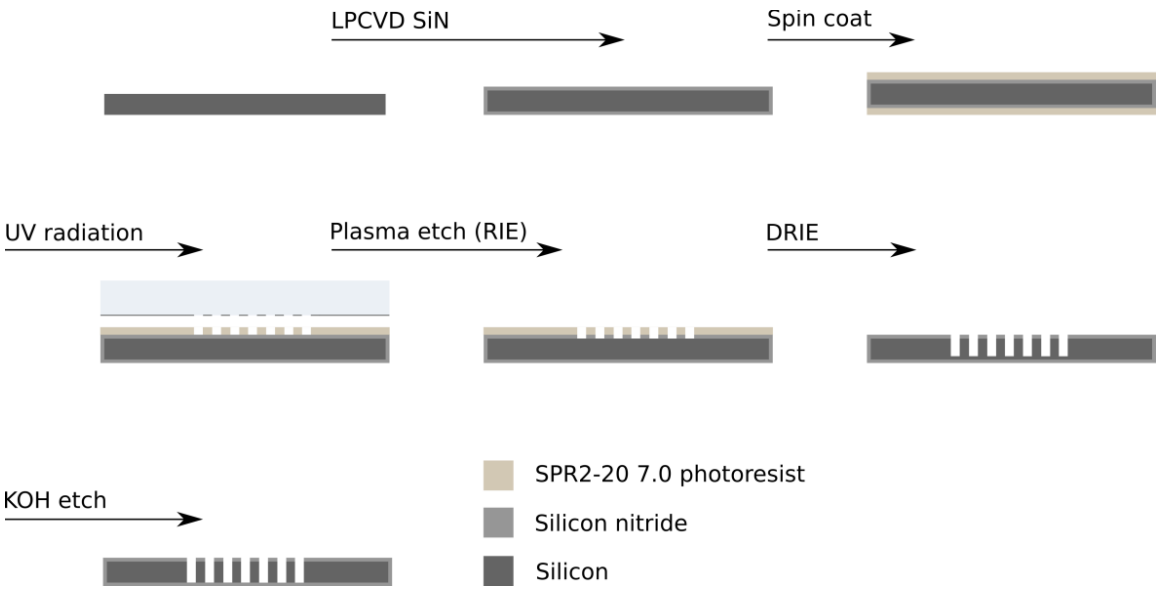

Figure 11: Overview of fabrication of silicon/silicon-nitride (Si/SiN) TEM substrates. Wafers are initially deposited with low-stress silicon nitride (100 nm-thick) followed by photolithography, and plasma etching. In practice we fabricated eight substrates on one 100-mm diameter wafer. See Appendix B for fabrication plan details.

3.2.3 Experiment methods

A single tissue block was manually trimmed to a cross sectional of ~1 mm x ~1 mm and placed into an ultramicrotome (Leica UC7). Four microfabricated substrates were placed on a hotplate (VWR), adjacent to the ultramicrotome, comprising 160 imaging

apertures. The hotplate was set to 95 ºC to enable rapid (< 30 s) drying of sections once placed onto the substrates. The ultramicrotome was set at cutting speed of 0.1 mm/s. Sections were transported away from the knife-edge via a puff of air, delivered manually through an air needle placed adjacent to the waterboat.

A 3-axis robotic system (Zaber Technologies), positioned adjacent to the ultramicrotome, was used to transport sections between the diamond knife waterboat (Diatome) and a microfabricated substrate, using a platinum-iridium wire loop (3 mm diameter) end-effector (TedPella) rigidly affixed to the terminal axis. Section pickup was conducted using manual control of the actuator system via an Xbox controller while placement of the sections onto the microfabricated substrates was automated, following a pre-specified array pattern matching that of the microfabricated substrate apertures. Custom Python-based software was used to interface with the Xbox controller and the actuator system.

After serial sectioning, sections were picked up onto the substrates using the loop end-effector and 3-axis robotic system, with no consecutive sections being placed on the same substrate. Between each section, the ultramicrotome was manually paused to allow for section pickup and placement; once pickup and placement were complete, the ultramicrotome sectioning was resumed. Section pickup and placement was conducted until all 160 apertures were occupied with sections or until a 2-hour imposed time limit to prevent effects due to water evaporation.

3.2.4 Data analysis methods

Video recording of serial section pickup and placement was conducted to analyze processing throughput and section placement accuracy, repeatability, and yield. From these

videos, a MATLAB-script was used to automatically identify and compute each section centroid. Sections that had separated into two or more pieces (but were successfully placed onto the substrate) were excluded from our accuracy and repeatability analysis to maintain a consistent section centroid definition. Yet, these partial sections were picked up and placed successfully. In determining yield, we defined section loss as sections lost due to broken substrate apertures, due to failed section pickup (e.g., loop end-effector damages the section during pickup, or partial sections were unrecoverable), due to failed section transport (e.g., surface tension within loop end-effector breaks during actuator movement), or due to failed placement (i.e., section is not released from the loop end-effector). Thus we define single section loss rate, p, as the probability of damaging or losing one section due to any of these occurrences. We note, in our yield calculation, we include sections that were partially misplaced over the TEM substrate imaging aperture but were successfully placed onto the substrate.

To compare the image quality of the microfabricated films (SiN) used in LASSO with conventional TEM grids (Luxel), we used two standard metrics to quantify the detectability of neuroanatomical structures (e.g., synaptic vesicles). First, the edge spread function (ESF) was computed by manually annotating synaptic vesicles in ITK-Snap on four separate images (2 SiN, 2 Luxel), drawing a line from the vesicle exterior to the interior, and then measuring the change in pixel intensities across the vesicle boundaries (Trägårdh, et al., 2015). Using derivative-based change-point detection, the change-points in the ESF were obtained and a line was fit to all points between the identified change points. Thus, the slope of this line, i.e., the mean roll-off of the ESF, provides a quantitative measure of the sharpness of edges for neuroanatomical structures of interest in our images

(Yushkevich, et. al., 2006). To quantify image contrast, the Michelson contrast was calculated for vesicle interior versus vesicle exterior points. Again, the vesicle interior and exterior pixel intensities were obtained from manually annotated vesicles (ITK-Snap). Then, the mean contrast value across all annotated vesicles was computed, giving a quantitative metric of the detectability of neuroanatomical structures in our images.

3.3 Theory

3.3.1 *Yield Modeling*

As a statistical model for predicting yield, we let each section pickup and placement event be a binomial random variable, where n is the number of sections to be processed and p be the probability of failure, i.e., damaging or losing one section. To successfully reconstruct a cubic millimeter of neural tissue with 40 nm-thick sections, 25,000 consecutive sections must be cut and imaged with zero *consecutive* section loss. Sections must be 40 nm thick or less to resolve distal neuronal processes that often are ~100 nm thick, thereby spatially sampling above the Nyquist frequency (Briggman & Bock, 2012). From prior literature, we can expect a single-section loss rate lower bound of 1% (Bock, et. al., 2011, Bumbarger, et. al., 2013, Lee, et. al., 2016). The probability of losing two consecutive sections then, assuming P(1 lost section) = p = .01, is

$$P(\text{2 consecutive lost}) = p * p = .0001 \tag{25}$$

Assuming n = 25,000 and a binomial probability distribution, the probably of losing 1 or more pairs of consecutive sections is

$$P(\text{1 or more consecutive pairs lost}) = \sum_{i=1}^{n-1} \binom{n-1}{i} (p*p)^i \, (1-p*p)^{n-1-i}, \tag{26}$$

equating to roughly 92%. The yield, or probability of success assuming failure criteria described above, for an experiment with 25,000 sections traditionally processed is thus 1 - 0.92 = 8%. Thus, with traditional serial sectioning, large-scale neuroanatomical studies are expected to be impractical. For LASSO, a "batch" of sections will comprise *c*m* sections, where *m* is the number of substrates per batch and *c* is the number of sections per substrate. In total, there are *k* batches where

$$k = \frac{n}{c*m} \tag{27}$$

and *n* is the total number of section to be processed. Let us assume the loss rate of a single substrate is *p'*. This is likely an overestimate of the substrate loss rate, since as substrates become larger and easier to handle, we expect fewer substrates to be lost. Within one batch, we will mandate that no two consecutive sections be placed on the same substrate. Therefore, we must lose two or more substrates to lose two consecutive sections. This probability, *P*, can be calculated as

$$P = P(\text{losing 2 or more substrates in 1 batch }) = 1 - [(1-p')^m + \binom{m}{1} (p') \, (1-p')^{m-1}]. \tag{28}$$

This represents the probability of one failed batch. Furthermore, we can calculate the probability of one or more failed batches out of the total number of batches, k, as

$$P(\text{1 or more failed batches}) = \sum_{j=1}^{k} \binom{k}{j} (P)^{i} (1-P)^{k-j}. \tag{29}$$

Thus, Eqns. 27-29 compose a framework by which to optimize yield by modulating m, the number of substrates per batch, and c, the number of sections per substrate.

3.3.2 Throughput Modeling

The total time to collect neuroanatomical datasets can be analyzed on a section-by-section basis. For traditional serial sectioning, the total time for data collection can be written as

$$T_{\text{traditional}} = \left(t_{\text{imaging}} + t_{\text{pickup, traditional}} + t_{\text{load time, traditional}}\right) * n, \tag{30}$$

where t_{imaging} is the time to image one section, $t_{\text{pickup, manual}}$ is the time to manually pick up and place one section onto a grid, $t_{\text{load time, traditional}}$ is the time to load one grid into the TEM, and n is the total number of sections to be processed.

For LASSO, the total time for data collection can be written as

$$T_{LASSO} = \left(\frac{t_{\text{load time, LASSO}}}{c*m} + t_{\text{imaging}} + t_{\text{pickup, robotic}}\right) * n\,, \tag{31}$$

where $t_{\text{pickup, robotic}}$ is the time to robotically pick up and place one section onto a substrate, $t_{\text{load time, LASSO}}$ is the time to load one substrate into the TEM.

3.3.3 Cost Modeling

For large sections, each TEM grid typically holds one section. As a result, the total cost for large-scale neuroanatomical datasets can be written as

$$C_{\text{traditional}} = n * c_{\text{grid}} , \tag{32}$$

where c_{grid} is the cost of one grid. For LASSO, sections are placed onto microfabricated substrates, which are manufactured on a wafer-by-wafer basis.

$$C_{\text{LASSO}} = \frac{n}{s} * w , \tag{33}$$

where s is the number of sections per wafer, and w is the cost of processing one wafer.

3.4 Results and Discussion

3.4.1 Manufacturing of microfabricated substrates

I have demonstrated the implementation of a scalable fabrication plan for high packing-density, electron-transparent, silicon/silicon nitride substrates (see Figure 12). Substrates were fabricated to interface with a custom load-lock for transmission electron microscopes housed at the Allen Institute for Brain Science. In addition, I have implemented surface modifications of the silicon nitride film in order to provide

differential hydrophobicity, allowing sections to dry down over the silicon nitride aperture, only, as shown in Figure 12A, by evaporating 100 nm of gold onto the silicon nitride and around the apertures. This potentially solves the problem of sections being misplaced over the non-electron-transparent region of the substrate, resulting in the inability to image those portions of the sample in the TEM.

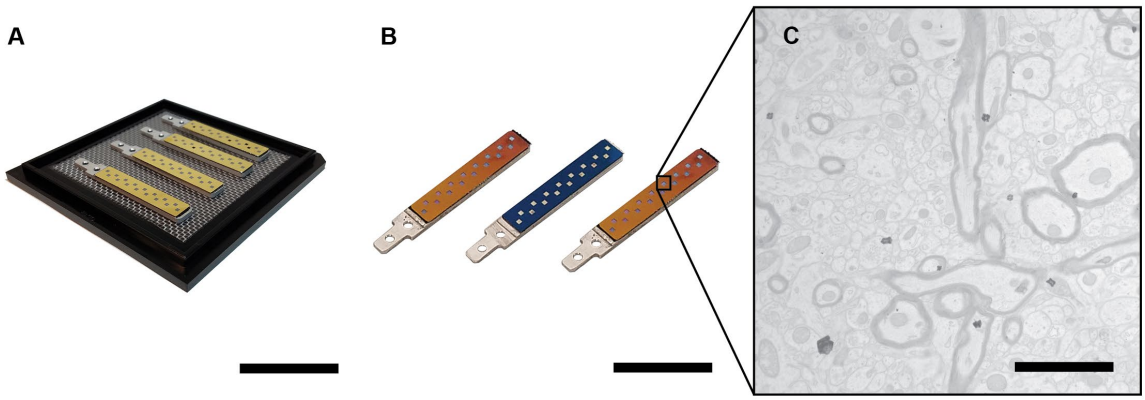

Figure 12: Photographs of preliminary results. (A) Custom fabricated Si-SiN-Au substrates for ssTEM (B) Si-SiN substrates; left to right: 200 nm, 100 nm, 50 nm SiN) (C) Transmission electron micrograph of mouse visual cortex demonstrating electron transparency of films. Scale bars: (A) 50 mm, (B) 30 mm, (C) 3 µm.

Substrates with varying SiN thickness are shown in Figure 12B. Through design and manufacturing iterations, we determined 100 nm to be an ideal thickness, balancing the film strength with image contrast. We determined 50 nm to be too thin for reliable manufacturing and handling while 200 nm to be too thick for sufficient contrast, given a 50 ms exposure time. While the exposure time could be increase to accommodate for thicker support films, this increase would significantly increase the total imaging time, which is undesired.

Furthermore, I have fabricated TEM substrates with 40 apertures of size 1.4 mm x 1.4 mm, (see Figure 13, right). With gross visual inspection, I do not observe deformation of the support film; additional TEM imaging will be necessary to confirm deformation of the support films. Additionally, I have been able to fabricate substrates containing 10 apertures with 3 mm x 3 mm apertures (see Figure 13, left) with 100 nm-thick SiN support films. This holds promise for the imaging of sections of size up to 3 mm x 3 mm, or these larger aperture substrates may be used to eliminate section misplacement.

Figure 13: (*left)* Photograph of one substrate containing 10 apertures of size 3 mm x 3 mm with silicon nitride support films of thickness 100 nm. *(right)* Photograph of 4 substrates containing 40 apertures of size 1.4 mm x 1.4 mm with silicon nitride support films of thickness 100 nm. Scale bars: 20 mm.

In total, we fabricated 26 individual silicon/silicon-nitride substrates. A photograph of four substrates (one batch) is shown in Figure 13, right. Each substrate contained forty 1.4 mm x 1.4 mm apertures with pitch 1.9 mm in both the x- and y-direction, as shown in Fig 13b. We processed four wafers and obtained an average yield of 81.25% (6.5/8 substrates) for each wafer. We note, while only 23 of the 26 substrates were used in our experiment, the remaining 3 substrates were of usable quality.

3.4.2 Pickup and placement of serial section with robotic tools

In conjunction with collaborators at the Allen Institute for Brain Science, I have designed and built an initial 3-axis manipulator system to interface with a Leica UC7 ultramicrotome (see Figure 14). The 3-axis manipulator system (Zaber) is equipped with two cameras (THORLABS) for stereoscopic vision. An Xbox controller is used to manually move the end-effector within the manipulator system work volume.

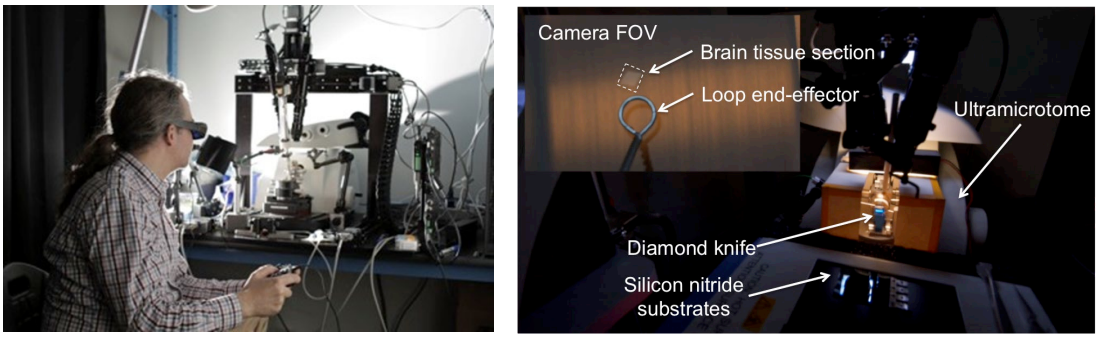

Figure 14: *(left)* Photograph of 3-axis manipulator interfacing with ultramicrotome with human operator. *(right)* Photograph of pick-and-place robot with microfabricated substrates nearby for section placement. *(right, inset)* Camera field-of-view showing the diamond knife waterboat containing an ultrathin section. The wire loop end-effector (diameter 1.5 mm) is on its way to pick up the section.

3.4.3 Characterization of LASSO

Using the robotic system, we picked up and placed 727 sections across 23 substrates, with a yield of 99.7% (727/729). A photograph of four of these substrates is shown in Figure 15a. A single video frame depicting the placement of a section onto a substrate with the loop end-effector is shown in Figure 15b. We find our yield to exceed that of prior work ($p < .05$), using the Fisher's exact test, to compare LASSO yield to

traditional serial sectioning by Lee, W.A., et. al., (3649/3700 sections) (Lee, et. al., 2016). We note that this comparison is difficult to make due to a variety of uncontrolled parameters (e.g., section size, tissue preparation, sectioning conditions), but in attempting to minimize these differences, we choose to compare to this particular work due to similar section cross-sectional area, section thickness, and the use of mammalian cortical tissue processed for electron microscopy in a similar manner (see Lee, et. al., 2016 for details). The two sections lost were due to substrate aperture failure. To this end, patterning the thin-film with out-of-plane stiffening features (e.g., ribs), may reduce aperture failures. Additionally, alternative aperture materials, such as silicon dioxide or graphene, may further reduce substrate aperture failures. As the field moves towards larger volumes of neural tissue, it is likely that a 1.4 mm x 1.4 mm would be insufficient to encompass the entire section within the imaging aperture. Thus, with the flexibility granted by microfabrication techniques—in particular photolithography—larger apertures can be readily created.

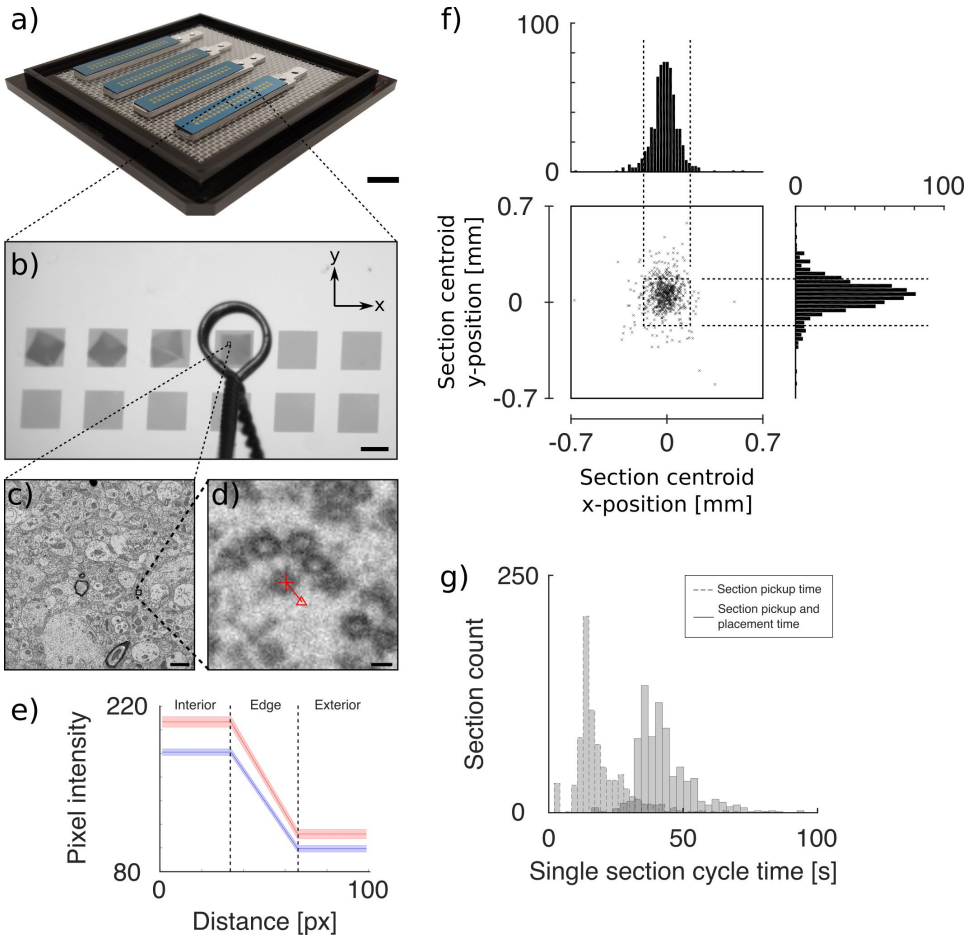

Figure 15: (a) Photograph of four microfabricated TEM substrates, each with forty 1.4 mm x 1.4 mm apertures (pitch: $p_x = p_y = 1.9$ mm) for TEM imaging. Each aperture contains a 100 nm-thick silicon nitride support films. Scale bar: 10 mm. (b) Photograph of a sub-area of a substrate with sections being placed onto the apertures using a loop end-effector. Scale bar: 1 mm. (c) Representative transmission electron micrograph of section sub-area on the microfabricated TEM substrate. Scale bar: 1 µm. (d) Electron micrograph sub-area depicting labeled vesicle interior (*red cross-hair)*, vesicle exterior *(red triangle)*, and connecting line (*red)* used to measure edge spread function. Scale bar: 10 nm (e) Mean edge spread function across manually annotated vesicle edges for images from sections on SiN *(red)* (n = 60) and Luxel *(blue)* (n = 60). We observe no significant difference in the slope of the ESF, indicating comparable sharpness of edges and image quality. (f) Using LASSO, scatter plot of section centroid positions with x- and y-centroid position distributions; plot extents correspond to imaging aperture size. Centroids located within the outlined box (*black dashed line*) have their entire area contained within the imaging aperture (587/631 sections, 93%). (g) Histogram of single-section pickup and placement time (*solid outline*) and single-section pickup time, only (*dashed outline*).

Sparse TEM imaging of sections was conducted to verify image quality. A representative transmission electron micrograph of a section placed on the microfabricated TEM substrate is shown in Figure 15c. Qualitatively, we are able to discern cell membranes and identify individual synaptic vesicles. An image sub-area is shown in Figure 15d, depicting manual annotation of one vesicle using methods described previously. Comparing images obtained on SiN compared to that of Luxel, we observe no visible difference in image quality. Furthermore, the mean slope of the computed edge spread function (ESF) was -2.56 +/-1.07 (n = 60) for Luxel (Figure 15e, blue) and -2.98 +/- 1.83 (n = 60) for SiN (Figure 15e, red), with idealized edges having infinite slope. The contrast for the Luxel film was 0.35 +/- 0.17 (n = 462) and 0.30 +/-0.14 for SiN (n = 636). Our analysis demonstrates that the image quality of the SiN film is comparable to Luxel—a conventionally used TEM grid support film. Thus, LASSO does not adversely affect image quality. Additionally, we observe a slightly larger slope in the SiN ESF, indicating sharper edges in the images. Thus, SiN-based substrates may be a suitable substrate for automated segmentation algorithms (Arganda-Carreras, et. al., 2015, Beier, et. al., 2017). While the Luxel support film does exhibit higher contrast, commonly used contrast enhancing methods (e.g., histogram equalization) could be applied to improve the contrast for SiN substrates.

Applying the criteria previously outlined, we analyzed the section placement accuracy and repeatability for 631/729 sections and report accuracy and repeatability of -20 ± 110 μm (x-axis) and 60 ± 150 μm (y-axis), as shown in Figure 15f. We find that 587/631 (93%) sections lie completely within imaging aperture while the remaining 631 – 587 = 44 sections are partially occluded from the imaging aperture. While traditional

definitions of section loss would consider these 44 sections to be "lost," we assert that this failure modality is easily remedied via fabrication of substrates with larger imaging apertures. From sections analyzed, given the same accuracy and repeatability, all 631 sections would lie within the 3 mm x 3 mm imaging aperture. We note the 96 sections excluded (due to their breaking into multiple pieces) from our accuracy and repeatability analysis (727 – 631 = 96 sections) may have fragmented due to a variety of causes, but we do not see this as a fundamental barrier for LASSO due to our ability to successfully pick up and place these sections onto TEM substrates as well as developments in segmentation algorithms to recombine fragmented sections in silico (Lee, et. al., 2017). Further study may investigate potential causes for section fragmentation to prevent partial section all together. Potential causes may include loop geometry, hysteresis of the water with respect to the loop, embedding plastic material properties, embedment protocol, or experiment section dry-down conditions.

We report an average cycle time of 43.5 s ± 11.7 s (Figure 15g, solid outline) and an average section pickup time of 18.9 s ± 9.7 s (Fig 15g, dashed outline). In comparing our average section pickup time with prior work (~2 min/section (Harris, et. al., 2006)), we find that our methodology has decreased the section pickup time by approximately a factor of five while removing the need for a human user with expert dexterity to pickup serial sections. Additionally, as demonstrated in electrophysiology (Wu, et. al., 2016), further automation of section pickup and multiplexing could lower the cycle time even further; thus increasing experiment throughput. Use of machine vision algorithms may accelerate the identification of section centroids while implementation of an automated section transport mechanism may obviate the need for a manually actuated air needle. Automated

transport of sections away from the knife-edge prior to section pickup may be accomplished via an automated pneumatic system, standing surface acoustic waves (Shi, et. al., 2007) or quadrupolar capillary interactions (Lee, et. al., 2018).

LASSO, as previously described, is the composition of several independent technologies that together create flexible, scalable, and accessible platform for large-scale ssTEM. Yet, each technology, on its own, merits its own discussion. As a part of LASSO, we introduce batch processing, an industrial engineering ideology commonplace in large-scale manufacturing settings. While we demonstrate and characterize a batch processing scheme that utilizes robotic tools and microfabricated substrates, these specifics components are not required to implement batch processing. Moreover, as shown from our modeling results, it is arrangement of serial sections in a specific manner into quantized groupings, i.e., "batches," that enables higher yield. This could be done whether using tape-based substrates (Hayworth, et. al., 2006), silicon wafer substrates (Kasthuri, et. al., 2015), or glass slides (Micheva & Smith, 2007). By distributing the risk of losing consecutive sections by physically placing them on separate substrates, we maximize the overall experiment yield.

Furthermore, in our implementation of LASSO, we used silicon/silicon-nitride substrates. In their current state, these substrates could be amenable to automated multi-parameter analysis by combining ssTEM with other analysis methods such as electrophysiology (Wu, et. al., 2016), array tomography (Micheva & Smith, 2007), and genetic analysis (Jiang, et. al., 2015). Alternatively, these substrates could be used with other imaging modalities, such as multi-beam scanning electron microscopy (SEM) (Schalek, et. al., 2016), scanning transmission electron microscopy (STEM) (Kuwajima,

et. al., 2013), or x-ray microscopy (Dyer, et. al., 2017), to provide imaging at multiple resolutions. In this manner, coarse rapid imaging could be combined with high-resolution TEM for morphological alignment. Moreover, further work could explore augmentation of our substrates. A promising direction may be the incorporation of micro-channels within the substrate (de Boer, et. al., 2000) or as a separate PDMS device (Walker & Beebe, 2002) to enable in situ staining. Additionally, the substrates could be designed for cell-culture to enable on-chip live-cell imaging/electrophysiology followed by live-cell EM imaging (de Jonge, et. al., 2009, Nishiyama, et. al., 2010). While each of these are potential future directions, LASSO does not depend on the utilization of microfabricated substrates. In our implementation, the substrates could be readily replaced with tape-based substrates, traditional grids, silicon wafers, or other substrates of choice.

While we demonstrate the ability to manipulate ultrathin sections, LASSO is likely compatible with a variety of section thicknesses. Therefore, semi-thin sections (~100 nm) for light microscopy or EM-based tilt tomography as well as thick sections (~10 μm) for focused ion beam scanning electron microscopy (FIBSEM) could be collected and placed onto an appropriate substrate using LASSO.

The picking-up of sections from the water surface remains a potential hazard. This is primarily due to the dynamic nature of the breaking and reforming of the water-air interface with each section retrieval. Therefore, alternative end-effectors for the 3-axis manipulator could be investigated to minimize surface disruption (e.g. custom microfabricated, hydrophobic, loop-based end effector, electro-wetting end-effector). These end-effectors may use capillary interactions to increase the accuracy in placement of sections.

Contamination of the silicon nitride films is a significant risk for successful connectomics studies. Any residual debris on the support film will occlude neuroanatomical information during TEM imaging. Contamination can occur at any point during the fabrication process. Potential sources of contamination include: contamination from glass containers (e.g., Pyrex), tweezers, or the etch bath. For any tools, custom Teflon tools can be fabricated to mitigate contamination. In addition, alternative etch processing can be investigated if KOH etching is insufficient, e.g., XeF2 etching.

While this study was limited to 729 sections, we do not expect fundamental barriers for scaling this technology from 10^3 to 10^5 sections, given appropriately apportioned batches. While other technologies may achieve high-yield and high-throughput serial sectioning, the accessibility of LASSO, due to our use of commercially available cameras, linear actuators, open-source, python-based control software, and standard microfabrication techniques, is a favorable alternative for large-scale serial sectioning.

3.5 Conclusion

LASSO represents a flexible, scalable, and accessible technology platform to enable the next generation of large-scale neuroanatomical ssTEM studies. From our modeling, we find that LASSO exceeds the yield, the throughput, and potentially, the cost of traditional serial sectioning methods. Moreover, implementing a batch size of four substrates, with each substrate holding forty sections, we predict an order of magnitude increase in yield. Using this prediction, we microfabricated custom substrates with corresponding size and implemented LASSO to quantify the yield and throughput of the methodology. We find our yield 727/729 (99.7%) exceeds that of prior work (two-sided Fisher test, $p = .05$); sections were placed accurately and repeatably (x-direction: -20 ± 110

μm (1 s.d.), y-direction: 60 ± 150 μm (1 s.d.)) within the imaging aperture. Sparse TEM imaging of sections showed no significant distortion, high-frequency information loss, or substrate-derived artifacts resulting from serial sectioning via LASSO. Regarding throughput, we find our methodology decreased the section pickup time by a factor of five while removing the need for a human user with expert dexterity to pickup serial sections. (Mean cycle time: 43.5 s ± 11.7 s; mean section pickup time: 18.9 s ± 9.7 s). This technology demonstrates a powerful tool for automating serial sectioning—a significant bottleneck for ssTEM neuroanatomical studies. Thus, we envisage LASSO will enable ssTEM physiological and neuroanatomical studies that investigate neural tissue volumes of size previously not possible, thereby bringing significant insight into the field of neuroscience.

CHAPTER 4. DESIGN, MODELING, AND CHARACTERIZATION OF CAPILLARY- AND STOKES-BASED SERIAL SECTIONING FOR MESOSCALE 3D-EM CONNECTOMICS

4.1 Introduction

Serial section electron microscopy (ssEM) has proven to be a powerful tool for the investigation of the brain—from analyzing millimeter-scale neuronal circuits to studying localized ultrastructure and microbiology (Briggman and Bock, 2012, Kuwajima, et. al., 2013, Lee, et. al., 2016, Hildebrand, et. al., 2017, Zheng, et. al., 2018, Karimi, et. al., 2019). To this end, the ability to process serial sections, i.e., the cutting of sections on an ultramicrotome into an adjoining waterboat and placement of serial sections onto EM substrates, has remained a critical step in ssEM. In recent years, research groups utilizing ssEM have diverged into two primary camps: (1) millimeter-scale serial section electron microscopy, which uses predominantly automated tools, collects petabyte-sized datasets composed of 10^4 – 10^5 serial sections, and investigates questions of neuronal circuit connectivity (Hayworth, et. al., 2006, Bock, et. al., 2011, Briggman and Bock, 2012, Hayworth, et. al., 2014, Kasturi, et. al., 2015, Lee, et. al., 2016, Hildebrand, et. al., 2017, Zheng, et. al., 2018, Karimi, et. al., 2019); (2) "traditional" serial section electron microscopy, which employs predominantly manual techniques, collects gigabyte-sized datasets composed of 10^0 – 10^1 sections, and investigates questions of localized neuroanatomy (Harris, et. al., 2006, de Lima, et. al., 2012, Kuwajima, et. al., 2013,

Androuin, et. al., 2018, Burgoyne, et. al., 2018, Hafner, et. al., 2018). As a result, serial sectioning has become more specialized and is predominantly conducted, correspondingly, one of two ways: automated tape ultramicrotome (ATUM) serial sectioning for millimeter-scale ssEM and ribbon-based, manual serial sectioning for "traditional" ssEM (Harris, et. al., 2006, Hayworth, et. al., 2006). While the field—through the use of these techniques—has investigated a wide range of pressing neurobiological questions, from dendritic spine geometry to large-scale cortical wiring diagrams, there remains an important need to collect and study mesoscale datasets, i.e., terabyte-sized datasets composed of 10^2 – 10^4 serial sections (Bock, et. al., 2011, Lee, et. al., 2016, Zheng, et. al., 2018, Chirillo, et. al., 2019). Within this intermediate dataset domain, a wide variety of neurobiological questions remain to be answered, e.g., questions of synaptic vesicle density, axonal fasciculation patterns, and neuronal biomechanical and ultrastructural variation, to name a few. In each of these examples, a few dozen serial sections would be insufficient to answer these questions, while several thousand serial sections would be impractical. Thus, there is a need to develop the appropriate tools for mesoscale serial sectioning to enable broader access to ssEM and accelerate the pace of neurobiological investigation.

The first described methods for collecting serial sections originate from the mid-1950's, where ribbons of sections, i.e., a series of sections that have been cut and remain attached to one another in a head-to-tail fashion, are manually picked up onto a slot grid for transmission electron microscopy (Dowell, 1959). Typically, these ribbons are ~100 micrometers in width and one millimeter in length, comprising approximately ten individual sections such that the ribbon in its entirety fits within the 1mm x 2mm slot grid (Harris, et. al., 2006). The accuracy and repeatability of this method is dependent upon the

human user and, as a result, requires significant manual dexterity and specialized training. Regardless, this methodology has remained a standard in the field of ssEM, due to its convenience and relative ease when processing only a few dozen serial sections. While a variety of methods to reduce or completely remove human skill from serial sectioning have been described, the automation of serial has converged on continuous, tape-based approaches. In this method, a reel of Kapton tape is fed into the waterboat and picks up ultrathin sections as they are cut on the ultramicrotome in a conveyor-belt-like fashion (Hayworth, et. al., 2006). The placement of the sections onto the tape is controlled by an initial calibration by a human user but is otherwise sufficiently robust for collecting thousands of serial sections without closed-loop control. While this method is highly efficacious for collecting thousands of serial sections without significant loss, the subsequent imaging of the sections is non-trivial. Conventional scanning electron microscopy (SEM), while ideal for imaging large samples, is prohibitively slow (Briggman and Bock, 2011). (As an aside, in recent years, advances in multibeam SEM have enabled high-throughput SEM imaging—the limitation now being the cost of a multibeam SEM) (Eberle, et. al., 2015). Transmission electron microscopy (TEM), on the other hand, requires customization of a TEM for tape substrate imaging (Bock, et. al., 2011, Lee, et. al., 2016, Zheng, et. al., 2018). In either case, storing, accessing, and analyzing datasets that are composed of thousands of images, i.e., several petabytes of raw data, is also not a trivial task. Thus, there remains a need for an automated serial sectioning methodology specifically designed for mesoscale ssEM studies.

In designing an automated system for serial sectioning, one of the most critical design parameters is the identification of the position of the section once it has been cut on

the ultramicrotome into the waterboat. For manual, ribbon-based serial sectioning, the human operator serves as the feedback system, using a microscope to locate the section within the waterboat, while for ATUM, the Kapton tape is placed near the cutting knife such that the section is picked-up onto the tape immediately after it is cut. In whichever case, in serial sectioning, the position of the section must be known to some degree for it to be picked-up and placed onto an EM substrate. To use the parlance of machine design, the position of the section must be controlled, ideally in a robust fashion, while minimizing sources of known errors (Dornfeld and Lee, 2008).

Prior work has shown the efficacy of curvature-induced capillary interactions and hydrodynamic forces to constrain the position, i.e., "trap," ultrathin serial sections with high accuracy and repeatability (Lee, et. al., 2018). While in this prior work, the sections were trapped using a millifluidic, open-channel device, it is likely the principles can be adapted to interface with a conventional diamond knife waterboat. Additionally, the Forest group and colleagues have shown the utility of using loop-based robotic tools to pick-up and place serial sections onto microfabricated, silicon nitride-based transmission electron microscopy substrates (Lee, et. al., 2018). While in this prior work, the robotic tools were controlled via human operator, the amalgam of a highly accurate and repeatable capillary-interaction/hydrodynamic trap with that of precision linear stage system may obviate the need for a human operator.

In the following, we describe an automated serial sectioning platform that uses a curvature-induced capillary-interaction-based (i.e., capillary-based), and hydrodynamic force-based (i.e., Stokes-based) trap to passively constrain sections with high accuracy and repeatability. In this method, individual sections are constrained in a stable force

equilibrium state akin to that of kinematic couplings used in precision machine design (Slocum, 1992, Rothenhöfer, et. al., 2013). Subsequently, the sections are picked-up with a loop end-effector that is rigidly affixed to a precision linear stage system. The end-effector is calibrated such that its pickup location is matched to a predetermined trapping location; as a result, serial sections are collected without the need for feedback control. Once removed from the waterboat, sections are placed directly onto a heated electron or light microscopy substrate for downstream imaging. In total, we design, fabricate, and characterize, with mathematical modeling and experimental validation, an open-loop, automated mesoscale serial sectioning system for scalable 3D-EM connectomics.

4.2 Methodology

In this system, individual sections are cut using a diamond knife on a conventional ultramicrotome into an adjoining waterboat. Prior to sectioning, our trapping device is installed within the waterboat, as shown in Figure 16A—otherwise, the ultramicrotome setup is unchanged from conventional ultramicrotome setup.

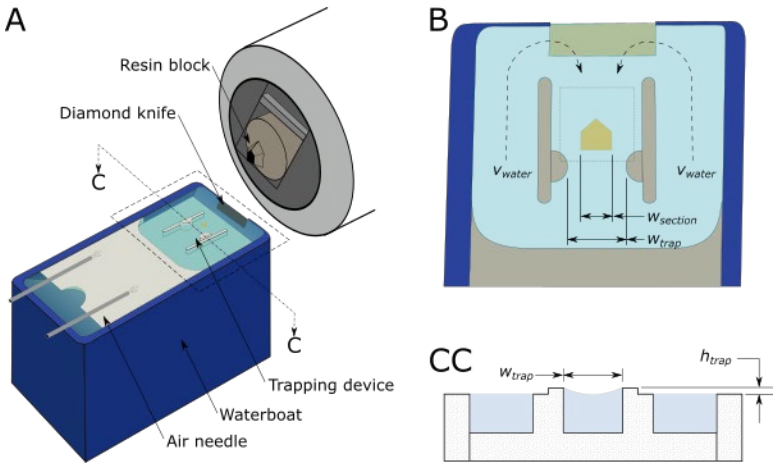

Figure 16: Diagram of diamond knife waterboat with trapping device installed. (A) The trapping device, shown within the waterboat, is composed of two semi-circular trapping posts and two parallel walls that separate the waterboat into three channels. When the water level is set to a typical cutting level, the channel walls do not protrude significantly from the water; the trapping posts, on the other hand, protrude roughly one millimeter from the nominal water surface, thereby creating curvature-induced capillary interactions (see cross-section view CC). Air needles are attached to the distal end of the waterboat to provide hydrodynamic forces. (B) Top view of trapping device, corresponding to the region bounded by the dashed line in (A). The air needles supply pressurized air which induce a symmetric water flow pattern with average water velocity, v_{water}, as shown. The forces trapping the section are modulated by the section size, $w_{section}$, the trap width, w_{trap}, the trap height, h_{trap} (see cross-section view CC), and the average water velocity, v_{water}. (CC) Cross-sectional view of the trapping device at the trapping posts. Outside of the center channel, the water level remains flat, as shown. Near the trapping posts, the water's edge attaches (or "pins") to the height of the trapping posts, h_{trap}, thereby creating local curvature in the water surface.

The section is transported away from the knife edge after it is cut and towards the trap via water flow, i.e., via hydrodynamic forces, as illustrated in Figure 16B. Upon reaching the trap, sections are repelled by curvature-induced capillary forces, establishing a static equilibrium. From this location, the section is picked up by a loop end-effector and placed onto a heated imaging substrate, e.g., silicon wafer, glass slide, in a pre-specified pattern such that the order of the serial sections is known. In the loop end-effector, the

section is held in place via surface tension forces; upon placement on the heated substrate, the residual water evaporates and the section lies down onto the substrate in a wrinkle-free fashion. The loop end-effector, being rigidly affixed to a precision xyz linear stage system, is calibrated to match the trapping location of the section; thus sections are collected in an open-loop fashion, i.e., without the need for feedback control.

Bulk resin blocks (EPON812) were trimmed manually to the appropriate cross-sectional area (~1.5 mm x 1.5 mm). Resin blocks were placed within the ultramicrotome (Leica UC7) sample chuck and not removed until all experiments trials were completed. Section trapping devices were designed using computer-aided design (CAD) software (SolidWorks). An example of a trapping device is shown in Figure 17A.

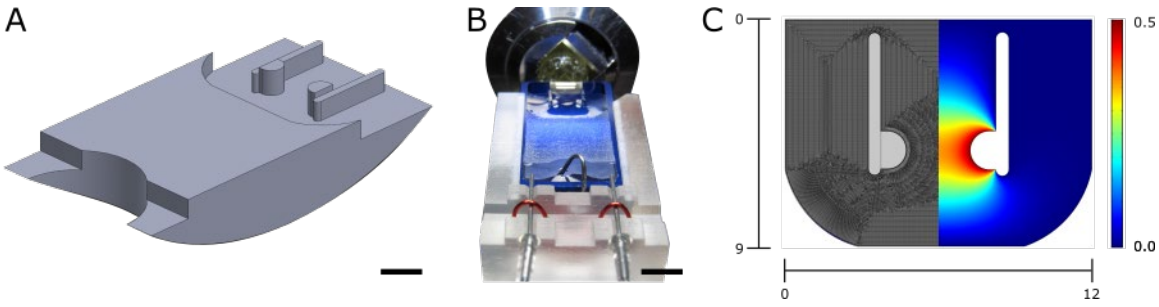

Figure 17: Computer-aided design (CAD) model with finite element analysis. (A) Isometric view of the trapping device designed in SolidWorks. This model has a trap width of 3.0 mm and a trap height of 0.5 mm. Scale bar: 3 mm. (B) Photograph of experimental setup. The trapping device is shown installed in the waterboat with water filled to appropriate height for sectioning. The induced curvature between the trapping posts can be observed. Air needles are mounted on the distal end of the waterboat using a custom fixture, which provide the hydrodynamic forces. A metal tube is shown protruding from the distal end of the waterboat used for modulating water level. Scale bar: 5 mm. (C) Top view of Young-Laplace equation solution domain. The domain is split symmetrically along the centerline, with the left side showing the finite element mesh and the right side showing the finite element solution for the interfacial height.

All devices were designed to interface with a Diatome Ultra 45 diamond knife with standard waterboat. Subsequently, design files were post-processed for 3D printing using CAM software (PreForm) and fabricated using a stereolithography (SLA) 3D printer (Formlabs, Form 2, Clear Resin). Upon completion, device dimensions were manually verified for accuracy.

Prior to sectioning, the section trapping device was placed within the diamond knife waterboat, as shown in Figure 17B. Being designed for the waterboat, the trapping device sits level with the outer walls of the waterboat, as shown in Figure 17B. Once installed, the waterboat is filled with water, as typically conducted for ultramictromy, and aligned with the resin block. Two needles were placed symmetrically at the distal end of the waterboat to induce symmetric water flow patterns within the waterboat (see Figure 17B). The needles were mounted to the waterboat using a custom fixture (see Supplemental Information) and were connected to a pressurized air cylinder. Air flow was regulated using a precision pressure regulator (Omega/ProportionAir QPV Series). A calibration was conducted to correlate the pressure regulator control voltage with water velocity (see Supplemental Information).

For characterizing and testing the section trapping device accuracy and repeatability, two experiment paradigms were used: single section testing and multi-section testing. For single section testing, the same section was trapped ten times across ten trials. In each trial, a video of the section was recorded for at least ten seconds at ~10 fps. For multi-section testing, ten different sections were trapped once, thus composing ten trials. Between trials, the previous section was removed from the waterboat and discarded and a new section was cut. In each trial, a video of the section was recorded for at least ten

seconds at 10 fps. In all experiments, the water level was maintained manually to minimize effects due to water evaporation.

Videos were imported into MATLAB for accuracy and repeatability analysis. For each video, a custom script was used to automatically identify the section centroid in each frame. For videos where contrast was insufficient for automated centroid identification, manually ROI selection was used. For accuracy measurements, the centroid measurements were compared to a fixed origin or "target" defined as the midpoint between the trapping posts and along the waterboat centerline, as shown in Figure 16B. For repeatability measurements, we used the standard deviation of the centroid measurements.

With this methodology, we fabricated and tested eight different device designs: four designs to vary the trap width (w_{trap} = 1.5 mm to 3.0 mm) while holding the trap height constant (h_{trap} = 0.5 mm) and four designs varying the trap height (h_{trap} = 0.5 mm to 0.84 mm) while holding the trap width constant (w_{trap} = 3.0 mm), as defined in Figures 16B and 16C. For all trap width modulation experiments, sections were cut at nominally 250 nm; for all trap height modulation experiments, sections were cut at nominally 200 nm. The system was calibrated such that average water velocity was ~1 mm/s to ensure laminar flow. From these experiments, an optimal trap design was selected and long-term automated serial sectioning experiments were conducted; for long-term automated serial sectioning experiments, sections were cut at 250 nm.

During long-term serial sectioning experiments, an individual section is cut using a diamond knife (Diatome) on a conventional ultramicrotome (Leica UC7) into an adjoining waterboat. In cases where the section stuck to the knife edge, an eyelash end-effector, rigidly affixed to a precision xyz linear stage system (ThorLabs) and manually

calibrated such that the eyelash end-effector would detach sections stuck to the knife edge, was used to remove the section from the knife edge. Upon being transported to the trap, the section is picked up by a loop end-effector (TedPella, inner diameter = 2.5 mm) and placed onto an adjacent heated imaging substrate, e.g., silicon wafer, glass slide, in pre-specified grid pattern. The loop end-effector is rigidly affixed to the same aforementioned precision xyz linear stage system and is manually calibrated to match the trapping location of the section. Once all the water has evaporated from the loop end-effector and the section has dried down onto the substrate, the loop end-effector returns to the pickup location, but above the water level, to await the next section for pickup. Sections were placed in a 14 x 9 grid with 3 mm spacing. Trials were limited to 126 serial sections, due to the size of the substrate. Between trials, the substrate was replaced with a new, empty substrate, the diamond knife was cleaned, and the loop and eyelash end-effectors were re-calibrated.

Samples were prepared for electron microscopy using previously published methods for electron microscopy staining. Prior to scanning electron microscopy (SEM) imaging, samples were imaged on a Zeiss Smartzoom 5 automated digital microscope to locate fiducial markers and obtain low-magnification mosaic images. SEM imaging was conducted using a multi-beam SEM (Zeiss MultiSEM 506) at 30 kV. Transmission electron microscopy was conducted using a JEOL 1200EX-II with accelerating voltage 120 kV. Samples placed onto glass slides for light microscopy were stained with toluidine blue for 30 s at 80°C and then imaged using a Leica DM6 microscope.

4.3 Theory

A mathematical model was used predict the trapping location of each trap design. The model is composed of two force contributors resulting in a static equilibrium:

curvature-induced capillary interactions and hydrodynamic forces. To model the effect of curvature-induced capillary interactions, we solved the Young-Laplace equation for each of our trap designs; using this solution, we calculated the capillary force acting upon a section within the device domain. To model the effect of hydrodynamic forces, we utilized the Stokes' drag force formulation. All parameters within our model were matched to that of experimental parameters, e.g., mean water velocity, section thickness. Using a force balance, we created a mathematical model to predict the centroid trapping location of a section for each trap design.

4.3.1 Curvature-induced Capillary Interactions

For each trap design, the model file was imported into a finite element analysis software (COMSOL) to solve the Young-Laplace equation for the water height within the device domain, as shown in Figure 17C. A two-dimensional domain matching the waterboat wetting conditions was selected, and a mesh was automatically generated, limiting the maximum element size to 0.025 mm to ensure sufficient spatial resolution of the solution and solution convergence, as shown in Figure 17C, left. In setting the boundary conditions, the water height at the trapping posts water set to match the height of the trapping posts, ranging from h = 0 mm to 0.84 mm, while all other boundaries were set to a water height of zero. Upon solving the Young-Laplace equation, written as

$$\Delta p = 2\gamma H, \tag{34}$$

where Δp is the Laplace pressure for the water-air interface, γ is the surface tension coefficient for a water-air interface at 25°C, and H is the mean curvature of the fluid-fluid

interface, the solution for the surface height, surface gradient, and surface Laplacian were exported as text files; an example of the surface height solution is shown in Figure 17C, right. These solutions were then imported into a custom MATLAB script (see Supplemental Information) to calculate the capillary force at each point in the domain. From prior literature, the curvature-induced capillary force, F_c, can be written as

$$F_c = 2\pi\gamma H_p R_p^2 \nabla^2 h \,, \tag{35}$$

where γ is the surface tension coefficient for a water-air interface at 25°C, H_p is the mean water deformation amplitude surrounding the section, R_p is the particle radius, i.e., the section thickness, and $\nabla^2 h$ is the surface height Laplacian (Stamou, et. al., 2000, Cavallaro, et. al., 2011).

4.3.2 Hydrodynamic Force Modeling

The Stokes' Law drag formula is written as

$$F_d = 4\pi\mu L_c C_d v \,, \tag{36}$$

where μ is the viscosity of water at 25°C, C_d is the drag coefficient of a thin plate, v is the average water velocity, taken from our calibration curve (see Supplemental Information), and L_c is the characteristic length of the section, defined as

$$L_c = \sqrt{w_{section}^2 + h_{section}^2 + t^2}\,, \tag{37}$$

where $w_{section}$, $h_{section}$, and t are the section width, height, and thickness, respectively (Saffman, 1976, Stamou, et. al., 2000). Given the density and viscosity of water at 25°C, the size of the trapping device (~1 mm), and the average water velocity (~1 mm/s), we calculate a Reynolds number of order unity, thus we assume laminar flow. The average water velocity was measured only for the trapping domain, thus we assume the Stokes' drag force calculation to be valid within the trapping domain. By subtracting the calculated Stokes' drag force, F_d, from the curvature-induced capillary force, F_c, and looking for the location where these two forces are equal and opposite in magnitude and direction, respectively, we are able to predict the trapping location of a section within the trapping device.

4.4 Results and Discussion

In designing our device for trapping serial sections, we performed a parameter study to understand the effect of various trap parameters. In particular, we tested four different trap widths and four different trap heights ranging from 1.5 to 3.0 mm and 0.5 to 0.84 mm respectively. A single frame of an individual section trapped within the trapping device is shown in Figure 18A. For this trial, the trap width was set to 2.5 mm and the trap height to 0.5 mm. From this image, we can see that the section is trapped between and above the semi-circular trapping posts due to the balance of curvature-induced capillary interactions (Figure 18A, *orange*) and Stokes' drag force (Figure 18A, *green*). In this way, the trap conforms to the exact constraint design principle, which states that the number of points of

constraint and number of degrees of freedom (DOF) should be equal (Blanding, 1999). The number of DOF experienced by the section is three: two DOF due to linear translation along and x- and y-axis, and one DOF due to in-plane rotation. The symmetric semi-circular trapping posts provide two capillary-based forces, pointing from the center of the semi-circular posts and towards the section centroid, and one restoring, Stokes-based force pointing down, i.e., negative y-direction, towards the section centroid, as shown in Figure 18A. In total, this trapping device represents a non-Hertzian contact-based kinematic coupling that could be useful for trapping soft matter (Young's modulus, E, ~1 MPa), as opposed to traditional Hertzian contact-based kinematic couplings used for conventional engineering materials that have Young's modulus ~1 GPa and rely on minimal deformation of the trapped material under the influence of the contact and restoring forces (Slocum, 1992, Rothenhöfer, et. al., 2013).

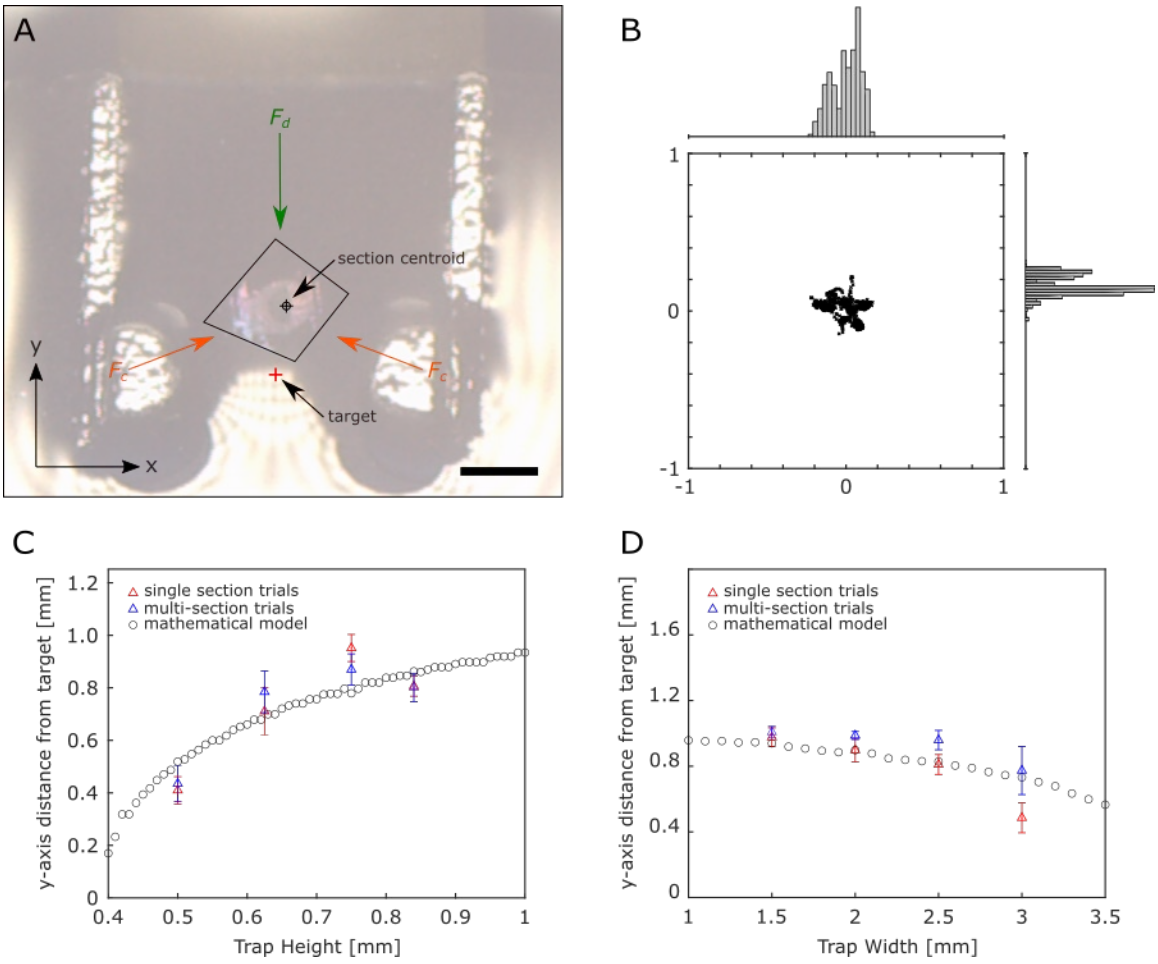

Figure 18: Trap design parameterization experiment and modeling results. (A) Single frame showing an individual section trapped within the trapping device. The section is trapped via balance of curvature induced capillary interactions, F_c, (*orange*) and Stokes drag forces, F_d, (*green*). The calculated centroid (*black crosshair*) and the defined target (*red cross*) are shown. The orientation of the x and y axes relative to the trapping device is shown in the bottom left. Scale bar: 1 mm. (B) Scatter plot of section centroid positions for a single trap design with w_{trap} = 2.5 mm, h_{trap} = 0.5 mm, $w_{section}$ = 1.5 mm. Ten sections were individually trapped and their positions recorded over time. For each section, we analyzed its local movement within the trap over ten seconds; videos were recorded at ten fps. All of the centroid positions are shown from all ten trials (*black x's*). The x-component centroid position distribution is shown above the scatter plot ($x_{st.\ dev.}$ = 91 µm); the y-component centroid position distribution is shown to the right of the scatter plot ($y_{st.\ dev.}$ = 62 µm). The centroids are plotted relative to the mean centroid position. Plot axes are given in millimeters. (C) Distance between the mean centroid position and target along the y-axis plotted versus the trap height. The mathematical model (*black circles*) shows a non-linear increase in the distance between the mean centroid position and target along the y-axis as the trap height increases. This trend shows good alignment with our single section (*red*) and multi-section (*blue*) experiment results (RMSE = 0.27 mm). (D) Distance between the

mean centroid position and target along the y-axis plotted versus the trap width. The mathematical model (*black circles*) shows a non-linear decrease in the distance between the mean centroid position and target along the y-axis as the trap width increases, showing good alignment with our single section (*red*) and multi-section (*blue*) experiment results (RMSE = 0.31 mm).

The section's centroids over a ten second duration is shown in Figure 18B, plotted with respect to its mean centroid position within this duration. We observe that the distribution of the centroid positions along both the x- and y-axis remains symmetric about its mean value without an observable bias or skew towards any direction. This is expected as the section has reached a static equilibrium in this trapped configuration, thus we do not expect a bias in the section's centroid position, which would be caused by an unaccounted external force. While the section is in a stable position, we note that the centroid positions show a non-zero standard deviation. The variability in centroid position within this ten-second duration could be caused by small variations in local water flow, in section orientation and size, or in water height due to evaporation. For each trap design paradigm, ten single section trials, i.e., trapping of the same section ten times, and ten multi-section trials, i.e., ten unique sections each trapped once, were conducted and their centroids analyzed using the methods previously described. The distance along the y-axis between the mean centroid position and the target, defined as the midpoint between the trapping posts and along the waterboat centerline, was calculated and plotted against the pertinent design parameter, as shown in Figures 18C and 18D. Due to the symmetry about the waterboat centerline for all of the trap designs, we found that the distance along the x-axis between the mean centroid position and the target to be constant between all trap designs (100 ± 80 μm). It is interesting that we observe a non-zero value given the trap design symmetry, but this is

likely due to the asymmetry of the section's geometry. Furthermore, in analyzing trends in the mean centroid position along the y-axis, we see that for the trap height parameter study, our model (Figure 18C, *black circles*) predicts that the distance between the mean centroid position and the target increases as the trap height increases in a non-linear fashion while for the trap width parameter study, our model (Figure 18D, *black circles*) predicts that the distance between the mean centroid position and the target decreases as the trap width increases in a non-linear fashion. For both the trap height and width parameter studies, the mean centroid positions from our single section (Figure 18C & D, *red triangles*) and multi-section (Figure 18C & D, *blue triangles*) experiments shows good alignment our mathematical model without any fitted parameters (RMSE = 0.27 mm, RMSE = 0.31 mm, trap height and width studies, respectively), indicating that the sections are predominantly trapped via a balance of curvature-induced capillary interactions and Stokes-based hydrodynamic forces. From prior literature, it is likely that the curvature-induced capillary interactions are quadrupolar-monopolar in nature (Stamou, et. al., 2000, Cavallaro, et. al., 2011, Yao, et. al., 2015, Lee, et. al., 2018). We note that while a trap height of 0.25 mm was tested, this trap height failed to consistently trap sections. Thus, it is likely that a trap height of 0.5 mm forms a functional lower limit for the robust trapping of serial sections. Additionally, we tested a trap height of 1.0 mm; at this trap height, the water fails to pin to the trapping post due to the inability for the water-air interface to assume such an extreme meniscus shape. Hence, a trap height of 0.84 mm represents a functional upper limit for the trapping of serial sections. Arguably, while the trapping of serial sections could still be possible for trap heights greater than 0.84 mm, additional methods would be necessary to know the precise water height at the trapping posts. For the trap width study, we limited

our minimum trap width to 1.5 mm as this value approached the section size. Further decrease in trap width would prevent movement of the section due to a physical barrier, i.e., the trapping device would behave as a size filter. Hence, for our section size, a trap width of 1.5 mm represents a functional lower bound for the trapping for serial sections. Additionally, for trap widths greater than 3.0 mm, we did not observe robust trapping of sections; instead, sections flowed freely through the trapping device without observable reduction in velocity as it approached the trapping posts; therefore, a trap width of 3.0 mm, for our section size, represents a functional upper bound for the robust trapping of serial sections. We see that in both trap design paradigms, the mathematical model capitulates an aliasing or staircase-like effect; this is likely due to the discretization of the domain from the finite element analysis and can likely be reduced by decreasing the mesh element size. While in our analysis, we use absolute values of trap height and trap width, these variables could be non-dimensionalized by relating these values to the section geometry. Additionally, since our system traps sections via a balance of two forces, capillary interactions and Stokes drag forces, this static equilibrium can be equivalently stated as the ratio of these two forces equated to unity. Hence, we can define a dimensionless quantity—the Capillary-Stokes number—that captures this relationship, written as

$$N_{cs} = \frac{F_d}{F_c} = \frac{4\pi\mu L_c C_d v}{2\pi\gamma H_p R_p^2 \nabla^2 h} = \frac{\mu v}{\gamma H_p R_p \nabla^2 h} = Ca \frac{1}{H_p R_p \nabla^2 h}. \quad (38)$$

In regimes where $N_{cs} \sim 1$, capillary/Stokes-based trapping can be effectively utilized. For systems where $N_{cs} >> 1$, drag forces dominate; while for systems where $N_{cs} << 1$, capillary interactions have a greater effect. We note that the Capillary-Stokes number can be thought

of as a modified capillary number (*Ca*), which conventionally describes the ratio of hydrodynamic to surface tensions forces. In our case, these surface tension forces are of a specific kind: curvature-induced quadrupolar capillary interaction. Thus, this is captured by the additional terms that modify the Capillary number, namely the deformation amplitude, H_p, the particle size, R_p, and the interface curvature, $\nabla^2 h$.

In selecting an optimum trap design for long-term automated serial sectioning experiments, we analyzed the root-mean-square (RMS) standard deviation of the mean centroid positions, i.e., the RMS repeatability, combining both the repeatability along the x- and y-axis into a single value. We found that for the trap height parameter study, a trap height of 0.5 mm ceded the smallest RMS repeatability (60 μm). For the trap width parameter study, while trap widths of 1.5 mm and 2.0 mm showed the smallest RMS repeatability values (70 μm for both widths), these designs were incompatible with our section pick-up method (loop-based pick-up); therefore, we chose to use a trap width of 2.5 mm, which gave the next-smallest RMS repeatability (100 μm). These repeatability values are well below 10% of the section's characteristic size. By using a loop end-effector to pick-up the sections with an inner diameter of 2.5 mm, which provided sufficient tolerance to accommodate our observed repeatability values, we were able to pick-up sections without a feedback control system. Using a trapping device with trap width and height equal to 2.5 mm and 0.5 mm respectively, we performed long-term automated serial sectioning experiments, placing the sections onto a variety of substrates to demonstrate the utility of the system. A photograph of a series of 100 serial sections (mouse cortical tissue, nominal section thickness = 60 nm) is shown placed onto a silicon wafer in Figure 19A.

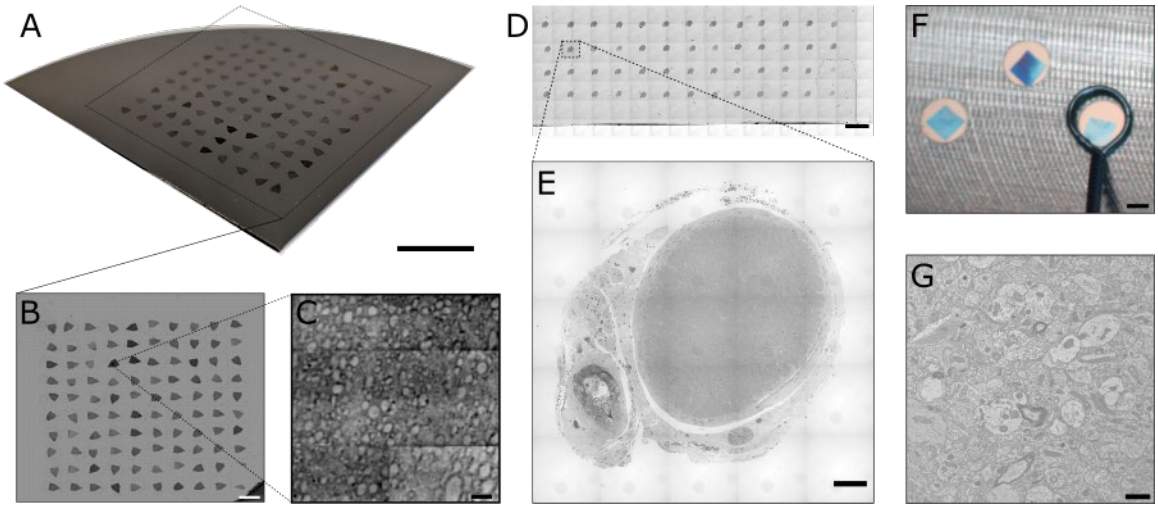

Figure 19: Examples of serial sections placed onto conventional light and electron microscopy substrates. (A) Photograph of 100 serial sections of mouse brain tissue of nominal thickness 60 nm placed onto a silicon wafer. Scale bar: 10 mm. (B) Top-view light micrograph of 100 serial sections placed onto a silicon wafer. Sections are placed in a raster-grid formation, with section 1 being on the bottom left corner, section 2 being above section 1, and section 100 at the top right corner. Scale bar: 3 mm. (C) Scanning electron micrograph imaged using a multi-beam SEM. Myelinated axons can be observed for potential sparse reconstruction of neuronal networks. Scale bar: 10 µm. (D) Mosaic low-magnification light micrograph of 52 rat optic nerve serial sections cut at 250 nm and placed onto a glass slide. Sections are stained with toluidine blue for optical contrast. Scale bar: 3 mm. (E) Mosaic high-magnification light micrograph of a rat optic nerve section. Individual axons can be observed within the optic nerve. Scale bar: 100 µm. (F) Image of three serial sections (nominal thickness 40 nm) placed onto an aluminum substrate with imaging apertures covered with Luxel support film for transmission electron microscopy. The loop end effector used to pick-up and placed sections is shown. Scale bar: 1 mm. (G) Representative high-magnification transmission electron micrograph of an ultrathin human cortical brain tissue section. Scale bar: 1 µm.

A top-view low-magnification light micrograph of the same sections is shown in Figure 19B. From this image, we do not observe any macroscopic defects, e.g., wrinkles or cracks, which may have occurred during the collection process. Because the sections are collected and placed onto a substrate in an automated fashion, the order of the placement

of the sections can be pre-specified. In this case, the sections were placed in a raster-grid pattern, i.e., section 1 is located at the bottom left corner with section 2 directly above it and section 100 is located at the top right corner. A high-magnification scanning electron micrograph is shown in Figure 19C, demonstrating the ability for this technique to be used for sparse reconstruction of neuronal networks. With further optimization of tissue staining for scanning electron microscopy could enable dense reconstruction of neural tissue as well as study of subcellular structures. A mosaic, low-magnification light micrograph of 52 serial sections (rat optic nerve tissue, section thickness = 250 nm) is shown in Figure 19D. In this experiment, sections were placed onto a glass slide and stained for optical contrast. Again, sections did not display macroscopic defects. A high-magnification image of an individual optic nerve section is shown in Figure 19E. At roughly 100x optical magnification, we do not see any defects that may have occurred during our serial section collection process. Additionally, individual axons are observable within the optic nerve, demonstrating the utility of this method for conventional light microscopy investigation of serial sections. This method could be useful for studying tissue volumes where high in-plane resolution is necessary while high out-of-plane resolution is unneeded. An example of this could be in studying structural variation in the optic nerve and the surrounding tissue along the length of the optic nerve and its relevance to myopathy or other vision degenerative diseases. An image of three serial sections (human cortical tissue, nominal section thickness 40 nm) is shown in Figure 19F. These sections are placed on an aluminum substrates with aperture covered with Luxel support film for transmission electron microscopy imaging. The loop end-effector is shown placing one section onto the substrate, demonstrating the compatibility of this system with TEM. A representative high-

magnification transmission electron micrograph is shown in Figure 19G. Within the micrograph, cross-sections of axons, dendrites, synapses, and subcellular structures can be observed. In total, we demonstrate that this system is amenable to scanning and transmission electron microscopy as well as conventional light microscopy. In total, we demonstrated the ability of this system to collect eight serial section datasets each composed of 126 serial sections with an average section loss rate 0.50% and average throughput of 63 seconds per section (see Supplemental Information for section images). We see that due to the repeatability of the trapping device and the tolerance afforded by the size of the loop, we are able to repeatably collect ~10^2 without section damage, providing a veritable mesoscale serial sectioning method for 3D-EM connectomics. This method can be scaled to larger volumes of tissue by collecting serial sections in a batch-wise process, as previously done (Lee, et. al., 2018).

The only failure mode we experienced during our long-term serial sectioning experiments were sections that stuck to the knife edge and as a result, were damaged during collection process. The source of this error remains to be determined. During our experiments, the humidity and temperature was recorded to be between 41-42% and 21-22°C; the water level was controlled within ±5 μL. Cutting and trapping parameters were kept constant between all experiments. The same tissue block was used for all experiments. Thus, with similar experimental parameters, serial sectioning experiments composed of ~10^2 can expect less than 1% section loss rate. For longer serial sectioning experiments (i.e., > 10^3 serial sections), further precision in the control of the experimental parameters is likely necessary if a 1% section loss rate is necessary, when using this serial sectioning

method. At this point, a viable alternative may be the implementation of an ATUM-based serial sectioning system.

While ATUM-based serial sectioning is capable of collecting mesoscale datasets, certain biological methods require imaging substrates other than Kapton tape, e.g., immunolabeling (Micheva and Smith, 2007, Lam, et. al., 2014, Fang, et. al., 2018). Additionally, while ribbon-based serial sectioning is capable of collecting mesoscale datasets, these are typically herculean efforts not readily replicated across research institutions. Thus, our system is a veritable method for mesoscale serial sectioning in the context of scalable 3D-EM connectomics. For many neurobiology labs which already have an ultramicrotome and an electron or light microscope, this system could be readily adopted in a piece-meal fashion, e.g., the trapping system could be used without a robotic pick-up system. In this case, the need for highly-trained, dexterous users would be ameliorated, and the traditional serial sectioning workflow would remain mostly unchanged. Another case could be adopting this system for compatibility with a tape-based substrate. As previously mentioned, immunolabeling could provide additional orthogonal information to a serial section dataset; thus by using a robotic pick-and-place system to place sections onto a variety of substrates, e.g., one out of every ten sections is placed onto a glass slide and processed for immunolabeling while the rest are imaged with EM, one could obtain both neuroanatomical and proteomic data (Randel, et. al., 2015, Williams, et. al., 2017).

With recent advances in automated segmentation of serial section EM datasets, the analysis of mesoscale datasets consisting of $10^2 – 10^3$ sections becomes possible without significant effort from human annotators. Additionally, due to the amenability of this serial

section collection methodology to various substrates, this method could be extended to other substrates, such as silicon nitride for transmission scanning electron microscopy studies (Kuwajima, et. al., 2013, Lee, et. al., 2018). Future work for this methodology may investigate a variety of parameters, such as section thickness, surface tension coefficient, and fluid viscosity. With regards to the study of section thickness, from preliminary results, it appears that the system remains stable within the 50 to 500 nm thickness range.

4.5 Conclusion

In total, this work represents an automated mesoscale serial sectioning system for scalable 3D-EM connectomics. From our experiments, we demonstrate the ability to repeatably collect ssEM datasets, composed of 126 serial sections, in an automated fashion with an average loss rate and throughput of 0.50% and 63 seconds per section, respectively (n = 8 trials). Furthermore, we show with light and EM imaging, the ability to collect serial sections onto a variety of electron and light microscopy substrates without significant defects or loss. As shown with modeling and experiment, our trapping device, accurately and repeatability positions sections through a balance of curvature-induced capillary interactions and Stokes-based drag forces. We designed, fabricated, and characterized the trapping device, identifying an optimal design from a parameterization study (RMS repeatability = 100 μm), thereby enabling collection of sections using open-loop control. Computationally, our mathematical model accurately predicts the trapping position of the sections over a range of trapping parameters (RMSE = 0.27 mm). Experimentally, our device interfaces with a conventional ultramicrotomy diamond knife, accomplishing in-line, exact-constraint trapping of sections within the waterboat. This design, model, and experiment extends the modeling of water-air interface forces as well as demonstrates a

useful tool for mesoscale serial sectioning electron microscopy, an important need in the field of connectomics and neuroscience.

CHAPTER 5. CONCLUSION

5.1 Perspectives on EM-based connectomics

Since the application of electron microscopy to the field of biology, EM has been the gold standard for studying microbiology with sub-optical resolution (Porter, et. al., 1945). Subsequently, with the invention of serial sectioning and volume electron microscopy, three-dimensional images of biological tissue could be obtained with nanometer resolution (Gay and Anderson, 1954, White, et. al., 1986). While at first, serial sectioning was prohibitively labor-intensive, in recent years, it has become more and more automated: from tissue processing to serial sectioning to imaging and to image segmentation and reconstruction (Hayworth, et. al., 2006, Bock, et. al., 2011, Hua, et. al., 2015, Lee, et. al., 2017). To some extent, volume electron microscopy has never been easier to do. So, the answer to the question (as some have previously inquired), "is EM dead?" seems as optimistic as ever: No, EM is not dead, rather we may be on the precipice of a renaissance for EM (Knott and Genoud, 2013).

5.1.1 Current drawbacks of EM-based connectomics

What are the limitations and drawbacks of EM-based connectomics? To start, there is significant capital needed—both in equipment and knowledge—to have a successful electron microscopy connectomics research program. On the low end, a TEM system, similar to the TEMCA system designed and built in the Reid Lab at Harvard, may cost a

few hundred thousand dollars. On the upper end, if one can afford it, a new multi-beam SEM would cost several millions dollars. In either case, this is a non-trivial amount of money—for a new or young investigator this may equate to a significant portion of one's university start-up package. In either case, additional cost for upkeep and maintenance is required. This portends a significant investment for an investigator not only from the standpoint of monetary cost but also in the future direction of one's research. Unlike light microscopes which have a wide variety of uses, an electron microscope represents a significant commitment to the study of the biological nanoscale, which some may not be willing to make immediately.

Second, electron microscopes require regular upkeep and well-trained users—in other words, an EM-based connectomics program requires a team of people with specialized knowledge for it to be successful. Electron microscopes, being ultra-high vacuum machines require regular maintenance, which, if not performed properly, can result in extended periods of downtime while the machine is repaired. Before use, significant training is required to learn to use an electron microscope and prepare biological electron microscopy samples. Currently, many electron microscope feature sample holders that require exceptional dexterity to handle. Preparation of biological samples for EM can take a few hours to multiple days to prepare, depending on the staining protocol, and often involves the use of hazardous and sometimes government-controlled materials, e.g., uranyl acetate. While these hurdles are not insurmountable, they can require weeks to months to even years to master.

In all—the cost, the specialized knowledge and training, the sample preparation—while on their own may not be insurmountable, the combination of all of these factors can

be a significant barrier to entry for those not fully committed to electron microscopy. In short, EM-based connectomics is not something you can quickly try out on your own. Unless a university or research institution is already set up with some of the components for EM-based connectomics, such as already owning a microscope or having technical support staff, it is incredibly difficult to enter the field.

5.1.2 Alternative technologies

Currently, there are a number of technologies that exist that could or are currently being used to investigate connectomics questions. Expansion microscopy, a method of immunolabeling and optically imaging tissue that has been expanded several orders of magnitude, has shown promise to be competitive with EM-based connectomics (Chen, et. al., 2015, Gao, et. al., 2019). Magnetic resonance imaging (MRI), which analyzes emitted radio-frequency signals in response to an imposed oscillating magnetic field, has been a popular method for connectomics but currently lacks the resolution of EM-based methods (Valiente and Marín, 2010, Jahanshad, et. al., 2013, Lynall, et. al., 2013, Marblestone, et. al., 2013, Korgaonkar, et. al., 2014, Fornito, et. al., 2015, Bray, 2017). X-ray microtomography, which uses high-energy x-rays to generate spectral images that are reconstructed *in silico* to create three-dimensional images, has been used to analyze brain tissue but is currently limited to roughly micron resolution (Dyer, et. al., 2017). In the following we discuss each of these methods and their advantages and disadvantages with respect to EM-based connectomics.

5.1.2.1 Expansion microscopy

In recent years, we have seen significant progress, predominantly by the Boyden Lab at MIT, in advancing optical methods for the investigation of nanoscale structures with expansion microscopy (Chen, et. al., 2015, Gao, et. al., 2019). Fundamentally, expansion microscopy relies on the labelling of cellular structures with molecular markers, which are then transferred to a polymer scaffold for subsequent expansion and imaging. In this process, the limiting factor for resolution is the size of the molecular marker. These labels have a finite size ~10^1 nm. As a result, obtaining ~10^0 nm resolution would require smaller molecular markers. This being known, sparse reconstructions of neuronal architectures, e.g., dendritic trees, dendritic spines, have been shown (Gao, et. al., 2019).

Overall, expansion microscopy is unlikely to replace electron microscopy in the field of connectomics—or vice versa. Electron microscopy, with its superior resolution and historical backing, will remain the gold standard for subcellular, neuroanatomical investigation. In the coming years, I would expect to see groups utilizing expansion microscopy to tackle questions of sparse neuronal connectivity. Because expansion microscopy uses molecular markers, it is inherently compatible with immunolabeling techniques, i.e., proteomic-based cell-typing. As a result, this may be an advantage for particular questions of neuroanatomy, e.g., cell-type-specific connectivity. Ultimately, optical microscopes, being ubiquitous and relatively inexpensive when compared to electron microscopes, when combined with expansion microscopy, may seem like an attractive alternative technology for young investigators looking to enter the field of connectomics.

5.1.2.2 Magnetic resonance imaging

In recent years, MRI-based methods for connectomics have been broadly applied to investigate connectomics-based changes in a variety of neuropathies as well as the link between connectomics and genomics (Valiente and Marín, 2010, Jahanshad, et. al., 2013, Lynall, et. al., 2013, Marblestone, et. al., 2013, Korgaonkar, et. al., 2014, Fornito, et. al., 2015, Bray, 2017). Being non-invasive, relatively ubiquitous, and amenable for human imaging, MRI is a powerful tool for connectomics studies. The question remains what insights can be made about neuroanatomy—if any—given the resolution of MRI. Traditionally, MRI systems cede millimeter-scale resolution—a dramatic resolution change compared to that of EM-based systems. Yet, in its current state, EM is far from imaging an entire human brain, let alone multiple human brains. (Not to mention the ability to image, store, access, and analyze this data would require herculean efforts and funding.) Therefore, MRI could be best used in conjunction with EM-based connectomics studies. A lower-resolution functional MRI could be performed to obtain high-level connectomics data to assess differences between specific regions of the brain, with these same regions being studied later on with EM-based techniques. This would be similar to approach used for functional connectomics, which combines volumetric optical imaging of live specimens followed by volumetric EM imaging of the same region. The insights drawn from a MRI/EM approach would likely be limited, given the large change in resolution.

5.1.2.3 X-ray microtomography

X-ray microtomography has been shown to be a useful tool for analyzing brain tissue with roughly micron resolution (Dyer, et. al., 2017). As a complement to EM-based techniques, x-ray tomography has been shown to be an ideal method, in part due to the similarity in sample preparation. The questions remains if x-ray tomography can

completely replace EM-based methods for neuroanatomical analysis. Fundamentally, x-ray tomography is not "diffraction limited" when it comes to resolution: x-rays have a wavelength ~0.1 to 10 nanometers, so theoretically, one could achieve sub-nanometer resolution with an x-ray tomography system. Despite the advantage of x-ray imaging ceding fully-aligned volumetric images, the limiting factor appears to be need from the scientific community. To generate an x-ray beam with sufficient power, a large synchrotron must be constructed, which is generally a large undertaking requiring significant resources, both monetarily and bureaucratically. As the field of connectomics progresses, it will be interesting to see how the development of synchrotron technology develops in parallel. Due to the limited number of facilities in the world that invest in synchrotron technology, it is unlikely that x-ray tomography will be the new mainstay technique for neuroanatomical connectomics.

5.2 Future directions

To date, the brain remains the least understood bodily organ with respect to the connection between its structure and its function. Moving forward, functional EM-based connectomics—that is the study of functional neuronal circuits *in vivo* via light-sheet or multi-photon imaging followed by EM-based neuroanatomical imaging and segmentation—is likely the best tool we have to investigate the link between form and function in the brain. While it is important to consider the method of investigation, the subject matter is equally if not more important. Do we study the human brain, the mouse brain, or something different altogether? While the human brain remains the holy grail of neuroscientific understanding, significant insights can and will be made using a variety of other animal models. The application of functional EM-based connectomics to novel

animal models will likely unlock a vast trove of discoveries with respect to sensory perception, memory, and learning. In the following we discuss various strategies young investigators might employ to further the field of connectomics.

5.2.1 Technological strategy

Let us assume, as a young investigator, we have decided to invest in functional EM-based connectomics as our main approach to studying questions of neuroscience. One, then, must consider the technologies at hand. If we look at recent young investigators who have started functional connectomics research groups, such as Professor Joshua Morgan at Washington University in St. Louis, one model for creating a successful connectomics research group is to use the existing EM infrastructure for your research. At large research universities, it is not uncommon for there to be one, if not multiple, electron microscopy suites dedicated for various types of research, e.g., materials science, neurobiology, protein crystallography. Therefore, as a young investigator, one might consider—in order to strategically budget one's start-up package—utilizing the tools already at hand at one's university.

A similar technology strategy has been collaboration. While the collection is neuroanatomical datasets using ssEM is time- and labor-intensive, once collected, they are rich with neuroanatomical and neurobiological information. A single large-scale dataset could drive multiple research questions and as a result, are often revisited time and time again to draw out further insight and discoveries. Therefore, the model of collaborating with a large EM-connectomics laboratory for the collection of these datasets, such as the connectomics group at the Allen Institute for Brain Science, the Lee Lab at Harvard, or the Lichtman group at Harvard, has been a successful strategy for a number of principal

investigators, e.g., Mei Zhen at the University of Toronto. The disadvantage of such a strategy is that the control afforded by collecting one's own data is lost. Nonetheless, the large benefit, especially for a young investigator, is the offloading of the financial investment in EM connectomics tools.

A third strategy that has yet to be employed for ssEM-based connectomics has been the use of benchtop electron microscopes. In recent years, a number of start-up companies have begun offering benchtop, low-voltage electron microscopes, e.g., element Precision Imaging, Delong America, Voxa Co. Monolithic companies, such as Zeiss, ThermoFisher Scientific, and JEOL have been the predominant manufacturers of electron microscopes for decades—as a result, these companies have dominated as well as to some extent, driven the direction of innovation in the electron microscopy space. In the case of TEM's the innovation has been directed towards higher resolution, as evinced by ThermoFisher Krios TEM, which is capable of atomic resolution. With regards to SEM's, we see multi-modal investigation as well as faster imaging have been the predominant directions of innovation, as evinced by Zeiss's suite ion beam microscopes and Zeiss's multi-beam SEM, respectively. While the multi-beam SEM developed by Zeiss is an attractive technology for EM-based connectomics, its price is a significant barrier to entry for most laboratories (~5 million USD). Therefore, the adoption of these benchtop electron microscopes paired with the low-cost serial sectioning methods, such as those described in this thesis, could be a pragmatic technology platform for entry-level EM-based connectomics research.

5.2.2 Animal model considerations

In the field of connectomics, mouse, zebrafish, and fruit-fly animal models remain the predominant biological tools used to study questions of function and neuroanatomy.

This is driven largely in part due to their amenability to genetic manipulation. Yet, historically, we see a number of remarkable discoveries in neuroscience have been through studying unlikely animal models, such as the California sea slug or the African clawed frog. Therefore, one might consider a neuroethological approach—that is a behavior driven approach—to neuroscientific research. A large range of animal behavior—behaviors that go beyond the human repertoire of abilities—remain to be studied using functional connectomics. Echolocation, used by bats and dolphins, remains to be fully elucidated from a functional connectomics-based neuroscientific understanding. Magnetoreception, used by birds, fish, and number of other organisms, is a powerful sensory perception that humans lack and remains to be understood. Yet, it is important to note, that it is only due to recent advancements in genetic manipulation and the maturation of EM-based connectomics tools, combined with volumetric light microscopy techniques that enables a neuroethological approach to neuroscience.

APPENDIX A. OVERVIEW OF BULK TISSUE PROCESSING

Overview of bulk tissue processing: A number of processing steps must occur prior to ultrathin sectioning for serial section transmission electron microscopy. For detailed procedures, see Hua et. al., 2015 and Harris, et. al., 2006. These steps are listed below with a brief description of each step:

1) Mouse brain explantation – Following in vivo experiments, i.e., functional imaging, electrophysiological recordings, the brain is removed the animal by a skilled researcher.

2) Chemical fixation – The explanted brain is immersed in a chemical fixative, such as paraformaldehyde. The chemical fixative cross-links proteins in the brain, preventing further natural decay.

3) Coarse sectioning – The brain once cross-linked is sliced in to thick slices (~1 mm – 100 μm) on a microtome, paying close attention to the brain's structure. Depending on the portion of the brain to be reconstructed using ssTEM, each slice is annotated according to which part of the brain is contained, e.g., visual cortex, somatosensory cortex, etc.

4) Heavy metal post-fixation – Thick slices must be stained with heavy metals to provide contrast during electron microscopy. Typically osmium tetroxide is used, which readily binds to cell membranes.

5) Dehydration – The thick slices must be dehydrated in preparation for epoxy infiltration. Typically, this is conducted via a graded series of alcohol immersion, such as methanol or ethanol.

6) Epoxy infiltration – Once dehydrated, thick slices are infiltrated with an epoxy resin and cured with heat. This encases the brain tissue within a hard plastic case, which can be cut into ultrathin sections.

7) Block-face trimming – At this point, the tissue is considered embedded. The embedded tissue is secured within an ultramicrotome collet and trimmed, either manually or with assistance from the ultramicrotome, until the appropriate cross-sectional area is exposed. The exposed surface is known as the block face.

8) Serial sectioning – The block face is aligned parallel to the knife. The water boat is filled such that the water barely wets the knife-edge. Section thickness is controlled by the ultramicrotome and can be modulated based on the observed section interference color. Sections are cut consecutively and lie on the water-air interface. Often, ribbons of sections are created during sectioning; consecutive sections as they are cut adhere to one another in a head-to-tail fashion, forming a long ribbon of sections.

9) Section processing – Sections are picked-up from the water-air interface and placed onto an electron transparent substrate, e.g., TEM grid.

10) Section imaging – Substrates with placed sections are loaded into a TEM and imaged.

APPENDIX B. FABRICATION PLAN FOR TEM SUBSTRATES

STEP #	PROCESS DESCRIPTION
0010	**OBTAIN SILICON WAFER WITH SiN** POLISH: SSP DIAMETER: 4 INCH DOPANT: B TYPE: P ORIENTATION: <100> THICKNESS: 500 µm GRADE: PRIME SiN SPECIFICATIONS: THICKNESS: 100 nm TYPE: LOW-STRESS CVD VENDOR: UNIVERSITYWAFER.COM
0020	**DEPOSIT HMDS LAYER** EQUIPMENT: KARL SUSS RC8 SPINNER RECIPE: STEP 1: 3000 rpm 1000 rpm/s 10 s NOTES FOR KARL-SUSS RC8 SPINNER: • PRESS 'ENTER' TO CLEAR ERRORS • PRESS 'ST/STOP' TO CLEAR ERRORS UNTIL YOU SEE '0000' • 'DEVICES' SHOULD ALL BE 'READY' • RIGHT-CLICK TO RESET IF THERE ARE STILL ERRORS • IF YOU NEED TO, POWER CYCLE THE MACHINE • SELECT THE OPEN FOLDER ICON TO ADD A RECIPE • SELECT THE NEW PAGE ICON TO EDIT A RECIPE • TO RUN YOUR RECIPE, USE THE DROP-DOWN MENU TO SELECT YOUR RECIPE, THEN SELECT RUN • BE SURE TO RUN THE AUTO-CLEAN RECIPE WITH THE CLEANROOM WAFER

	• FOR THE HOT-PLATE, DO NOT CHANGE 'CALIBRATION' OR 'PID' LOOPS VALUES
0030	**DEPOSIT PHOTORESIST** PHOTORESIST: SPR-220 EQUIPMENT: KARL SUSS RC8 SPINNER RECIPE: STEP 1: 500 rpm 100 rpm/s 10 s STEP 2: 3000 rpm 1000 rpm/s 40 s STEP 3: 0 rpm 500 rpm/s 0 s
0040	**BAKE PHOTORESIST** EQUIPMENT: KARL SUSS RC8 SPINNER RECIPE: TEMPERATURE: 115 °C TIME: 60 seconds
0050	**ALIGN MASK / EXPOSE PHOTORESIST** EQUIPMENT: KARL SUSS TSA MA-6 PARAMETERS: CONTACT TYPE: HARD CONTACT ALIGNMENT GAP: 30 µm NOTES FOR KARL-SUSS TSA MA-6: • BE SURE TO CHECK LAMP INTENSITY WITH UV SENSOR, IN BLACK CASE UNDERNEATH MACHINE • BE SURE 365 nm WAVELENGTH IS SELECTED • CH 1 IS 365 nm • IF 'CHANGE MASK' SCREEN IS ON, PRESS' CHANGE MASK' TO GO BACK TO MAIN SCREEN

	• PLACE SENSOR ON CHUCK AND PRESS 'LAMP TEST' TO COMMENCE UV INTENSITY TEST • FOR SPR-220, APPROXIMATELY 500 mJ/cm^2 IS REQUIRED • USE 'EDIT PARAMETER' BUTTON TO ADJUST EXPOSURE TIME AND THE ALIGNMENT GAP • HARD CONTACT IS OK • ONCE MASK IS ALIGNED, PRESS 'ALIGN CONT/EXP' TO BRING WAFER INTO CONTACT WITH MASK. IF ALIGNMENT IS NOT GOOD, PRESS 'ALIGN CONT/EXP' TO RELEASE MASK AND WAFER PROCEED WITH ALIGNMENT • PRESS EXPOSE TO BEGIN EXPOSURE. • BE SURE TO REMOVE THE MASK, RETURN SUBSTRATE KNOBS TO X10 AND Y10, AND ROTATE CHUCK HOLDER SO THAT THE WHITE LINES MATCH.
0060	**DEVELOP PHOTORESIST** DEVELOPER: MF-319 for SPR-220 photoresist DEVELOP FOR 3 MINUTES, THEN PLACE WAFER IN WATER BATH FOR AT LEAST 3 MINUTES. AFTERWARDS, THOROUGHLY DRY THE WAFER.

0070	**ETCH SILICON NITRIDE LAYER THRU TO SILICON**
	
	EQUIPMENT: OXFORD END-POINT RIE
	
	NOTES FOR OXFORD END-POINT RIE:
	
	• VISION RIE IS FINICKY. IT MIGHT BE FASTER, BUT IT IS INCONSISTENT. BEST TO USE OXFORD.
	• SELECT THE 'SYSTEM' BUTTON
	• PRESS 'STOP' TO BEGIN VENTING PROCESS
	  ○ SELECT 'VENT' TO VENT CHAMBER
	• WHEN TIME IS <100s, SWITCH 'CHAMBER DOWN' TO 'CHAMBER UP'
	  ○ THEN PRESS BOTH GREEN BUTTONS SIMULTANEOUSLY TO OPEN CHAMBER
	  ○ YOU WILL ALSO HEAR WHEN IT IS OK TO OPEN THE CHAMBER
	• MAKE SURE O-RING IS SEATED EVENLY

	• THERE ARE 2 PLATTENS: Al & Graphite
	  ○ Al if etch depth is < 2 μm
	  ○ Graphite is etch depth is > 2 μm
	• SWITCH TO 'CHAMBER DOWN' AND PRESS BOTH GREEN BUTTONS SIMULTANEOUSLY TO LOWER LID
	  ○ MAKE SURE LID IS ALIGNED CORRECTLY. MAY NEED TO ADJUST MANUALLY
	• PRESS 'STOP', THEN 'EVACUATE'
	  ○ BE SURE TO READ PROMPT CLOSELY. IT WILL TELL YOU TO PRESS 'CANCEL' IF YOU ARE EVAUCATING AN EMPTY CHAMBER.
	• TO SELECT YOUR PROCESS, GO SELECT THE PROCESS BUTTON
	  ○ RECIPES -> LOAD -> OK
	
	• **STANDARD OXIDE ETCH: (OK for etching 100 nm of SiN)**
	  ○ **PRESSURE: 50 mTorr**
	  ○ **O_2: 4**
	  ○ **CHF_3: 35**
	  ○ **RF power: 250**
	  ○ **Step time: 3 min**
	
	• AFTER DONE, SELECT CHAMBER CLEAN
	  ○ MAKE SURE Al PLATTEN IS IN CHAMBER

0080	**ETCH (DRIE) SILICON**
	
	EQUIPMENT: STS HRM ICP
	
	RUN RECIPE 'HC_GENM' FOR 350 CYCLES. THIS SHOULD ETCH 400 μm OF Si.
	
	NOTES FOR STS HRM ICP:
	
	• 'VENT' LOAD LOCK TO LOAD SAMPLE; LID WILL OPEN ONCE BY ITSELF
	• PLACE SAMPLE ON SHUTTLE, CLOSE LID, AND PRESS 'PUMP & MAP'
	• SELECT WAFER POSITION (1 OR 2) AND PRESS 'LOAD' TO LOAD SAMPLE INTO ETCHING CHAMBER
	• GO TO 'RECEIPE'
	  ○ OPEN AND EDIT THE RECIPE YOU WANT TO RUN.
	  ○ IT IS OK TO OVERWRITE RECIPES
	  ○ USE 'HC_GENM' RECIPE
	  ○ WE WILL ONLY EDIT THE NUMBER OF CYCLES
	  ▪ 350 CYCLES ≈ 400 μm

	○ SAVE RECIPE AND CLOSE RECIPE EDITING WINDOW • PRESS 'SELECT' (NOT 'PROCESS') ○ SELECT DESIRED RECIPE, LET IT LOAD. ONCE LOADED, PRESS 'PROCESS' TO BEGIN ETCH.
0090	**DICE WAFERS USING DICING SAW** EQUIPMENT: ADT 7100 DICING SAW
0100	**PEEL INDIVIDUAL DICED SUBSTRATES FROM DICING TAPE** SUBSTRATES ARE VERY FRAGILE; USE CARE WHEN PEELING SUBSTRATES OFF OF DICING TAPE. USING ACETONE TO REMOVE ADHESIVE CAN HELP BUT CAUSES ADHESIVE LAYER TO COME OFF OF THE TAPE BACKING. CAN BE MESSY.
0110	**RINSE SUBSTRATES OFF WITH ACETONE THEN ISOPROPYL ALCOHOL AND THEN DI WATER** BE SURE TO REMOVE ALL RESIDUAL PHOTORESIST PRIOR TO KOH ETCH.
0120	**LET SUBSTRATES AIR DRY THOROUGHLY** SUBSTRATES CAN BE PLACED ON HOTPLATE TO ACCELERATE DRYING.
0130	**KOH ETCH SILICON THRU TO SILICON NITRIDE AT 85˚C FOR 1 HOUR OR UNTIL APERTURES ARE CLEAR.** EQUIPMENT: KOH 45% AQUEOUS SOLUTION TEFLON ETCHING FIXTURE DO NOT DILUTE KOH; IT SHOULD BE AT CORRECT CONCENTRATION. PLACE SUBSTRATES IN TEFLON ETCHING FIXTURE. EXPOSED SILICON SHOULD BE FACING UP TO ALLOW HYDROGEN BUBBLE TO FREELY PERCOLATE. FIXTURE HOLDS UP TO 9 SUBSTRATES PLACE FIXTURE WITH SUBSTRATES IN SHALLOW BEAKER AND FILL WITH KOH TO FULLY COVER FIXTURE

	DO NOT OVER ETCH SUBSTRATES. SILICON FRAME MAY TO DETERIORATE

APPENDIX C. WATER VELOCITY CALIBRATION CURVE

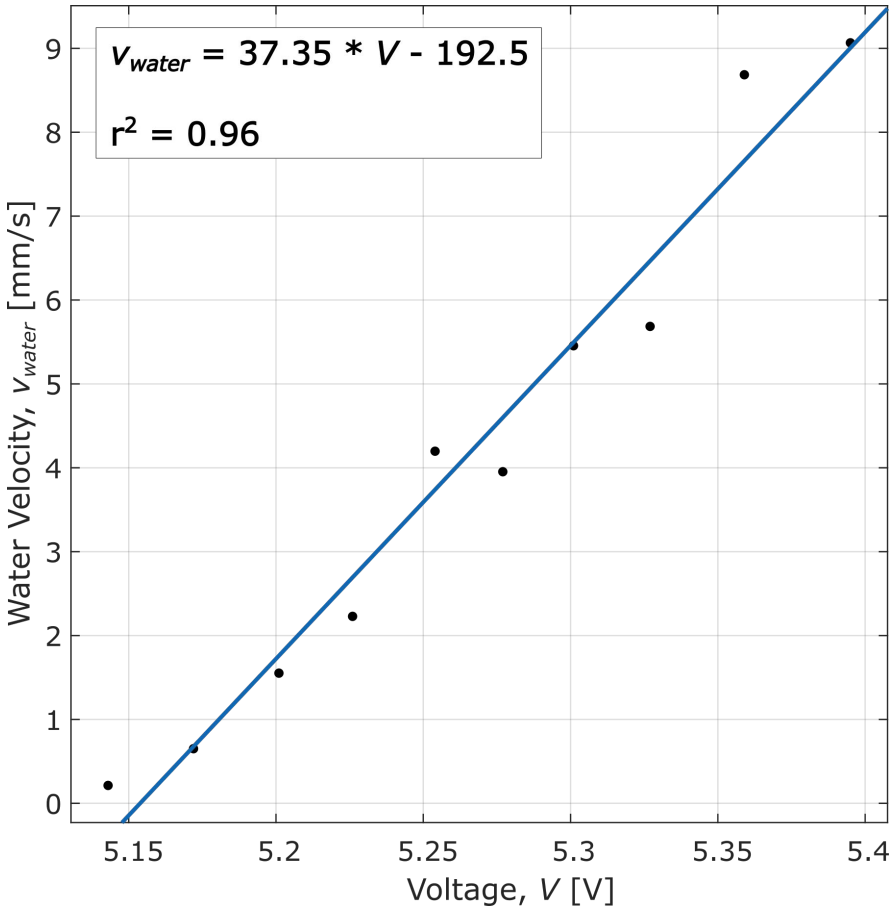

REFERENCES

Androuin, A., Potier, B., Nägerl, U. V., Cattaert, D., Danglot, L., Thierry, M., … Marty, S. (2018). Evidence for altered dendritic spine compartmentalization in Alzheimer's disease and functional effects in a mouse model. *Acta Neuropathologica*, 135(6), 839–854. https://doi.org/10.1007/s00401-018-1847-6

Arganda-Carreras I, Turaga SC, Berger DR, Ciresan D, Giusti A, Gambardella LM, et. al. (2015) Crowdsourcing the creation of image segmentation algorithms for connectomics. *Front Neuroanat*. 9:142.

Barnes, B. G. and Chambers, T. C. (1961). A simple and rapid method for mounting serial sections for electron microscopy. *J. Biophys. Biochem. Cytol.,* 9, 724.

Bauer, T., Zheng, Z., Renn, A., Enning, R., Stemmer, A., Sakamoto, J. & Schluter, A. D. Synthesis of Free-Standing , Monolayered Organometallic Sheets at the Air/Water Interface. *Angewandte Chemie*, 50(34) 7879–7884 (2011). doi:10.1002/anie.201100669

Beier T, et al. (2017) Multicut brings automated neurite segmentation closer to human performance. *Nat Meth* 14:101–102.

Blanding, D. L. (1999). Exact Constraint: Machine Design Using Kinematic Principles. *ASME Press.* https://books.google.com/books/about/Exact_Constraint.html?id=DtxSAAAAMAAJ

Bock, D. D., Lee, W. C., Kerlin, A. M., Andermann, M. L., Hood, G., Wetzel, A. W., et al. (2011) Network anatomy and in vivo physiology of visual cortical neurons. *Nature* 471:177–182.

Bowden, N., Arias, F., Deng, T., and Whitesides, G.M. (2001) Self-Assembly of Microscale Objects at a Liquid/Liquid Interface through Lateral Capillary Forces. *Langmuir.* **17(5)**, 1757-1765. doi: 10.1021/la001447o

Bray, N. (2017). Neurodevelopmental disorders: Converging on autism spectrum disorder. *Nature Reviews Neuroscience*, *18*(2), 67. https://doi.org/10.1038/nrn.2016.184

Briggman KL, Bock DD (2012) Volume electron microscopy for neuronal circuit reconstruction. *Curr Opin Neurobiol* 22:154–161.

Bumbarger DJ, Riebesell M, Rödelsperger C, Sommer RJ. (2013) System-wide Rewiring Underlies Behavioral Differences in Predatory and Bacterial-Feeding Nematodes. *Cell*. 152(1–2):109-119. https://doi.org/10.1016/j.cell.2012.12.013.

Burgoyne T, Lane A, Laughlin WE, Cheetham ME, Futter CE (2018) Correlative light and immuno-electron microscopy of retinal tissue cryostat sections. *PLoS ONE,* 13(1): e0191048. https://doi.org/10.1371/journal.pone.0191048

Cavallaro, M., Botto, L., Lewandowski, E. P., Wang, M. & Stebe, K. J. Curvature-driven capillary migration and assembly of rod-like particles. (2011) *Proc. Nat. Acad. Sci.,* 108(52) 20923-20928 doi:10.1073/pnas.1116344108

Chen, F., Tillberg, P. W., & Boyden, E. S. (2015). Expansion microscopy. *Science*, *347*(6221), 543–549.

Chirillo, M. A., Waters, M. S., Lindsey, L. F., Bourne, J. N., & Harris, K. M. (2019). Local resources of polyribosomes and SER promote synapse enlargement and spine clustering after long-term potentiation in adult rat hippocampus. *Scientific Reports*, *9*(1), 1–14. https://doi.org/10.1038/s41598-019-40520-x

Chung K, Crane MM, Lu H (2008) Automated on-chip rapid microscopy, phenotyping and sorting of C. elegans. *Nat Meth* 5:637–643.

Cohen, A. E. & Moerner, W. E. (2008) Controlling Brownian motion of single protein molecules and single fluorophores in aqueous buffer. Opt Express. May 12;16(10):6941-6956.

de Boer MJ, Tjerkstra RW, Berenschot JW, Jansen HV, Burger GJ, Gardeniers JGE, Elwenspoek M, and van den Berg A. (2000) Micromachining of Buried Micro Channels in Silicon. *J Microelectromech S.* 9(1):94-103.

de Jonge N, Peckys DB, Kremers GJ, Piston DW. (2009) Electron microscopy of whole cells in liquid with nanometer resolution. *PNAS.* 106(7):2159-2164.

de Lima, S., Koriyama, Y., Kurimoto, T., Oliveira, J. T., Yin, Y., Li, Y., … Benowitz, L. (2012). Full-length axon regeneration in the adult mouse optic nerve and partial recovery of simple visual behaviors. *Proceedings of the National Academy of Sciences*, 109(23), 9149–9154. https://doi.org/10.1073/pnas.1119449109

Ding, X. Lin, S. S., Kiraly, B., Yue, H., Li, S., Chiang, I. K., et al. (2012) On-chip manipulation of single microparticles, cells, and organisms using surface acoustic waves. Proc Natl Acad Sci U S A. June 4;109(28):11105-11109. doi:10.1073/pnas.1209288109

Dominguez, A., Oettel, M., and Dietrich, S. (2008) Force balance of particles trapped at fluid interfaces. *J. Chem Phys.*, 128, 114904. doi: 10.1063/1.2890035

Dornfeld, D. & Lee, D-E. (2008) Precision Manufacturing. New York, NY. Springer Science+Business Media. https://link.springer.com/content/pdf/10.1007%2F978-0-387-68208-2.pdf

Dowell, W. C. T. (1959). Unobstructed mounting of serial section. *J. Ultrastruct. Res.,* 28,634.

Dyer, E. L., Roncal, W. G., Prasad, J. A., Fernandes, H. L., Gürsoy, D., Andrade, V. D., Fezza, K., Xiao, X., Vogelstein, J. T., Jacobsen, C., Körding, K. P., Kasthuri, N. Quantifying Mesoscale Neuroanatomy Using X-Ray Microtomography. *eNeuro*. 4(5):0195-17.2017 (2017). DOI: https://doi.org/10.1523/ENEURO.0195-17.2017

Eda, G., Fanchini, G. & Chhowalla, M. (2008) Large-area ultrathin films of reduced graphene oxide as a transparent and flexible electronic material. Nat Nanotechnol. 3:1–5.

Eberle, A. L., Mikula, S., Schalek, R., Lichtman, J., Knothe Tate, M. L., & Zeidler, D. (2015). High-resolution, high-throughput imaging with a multibeam scanning electron microscope. *Journal of Microscopy*, *259*(2), 114–120. https://doi.org/10.1111/jmi.12224

Fahrenbach WH (1985) Anatomical circuitry of lateral inhibition in the eye of the horseshoe crab, Limulus*. Proc. R. Soc. Land.* B 225, 219-249

Fang, T., Lu, X., Berger, D., Gmeiner, C., Cho, J., Schalek, R., … Lichtman, J. (2018). Nanobody immunostaining for correlated light and electron microscopy with preservation of ultrastructure. Nature Methods, 15(December). https://doi.org/10.1038/s41592-018-0177-x

Fang, Y., Guo, S., Zhu, C., Zhai, Y. & Wang, E. Self-Assembly of Cationic Polyelectrolyte-Functionalized Graphene Nanosheets and Gold Nanoparticles: A Two-Dimensional Heterostructure for Hydrogen Peroxide Sensing. *Langmuir,* **26(13),** 11277–11282 (2010).

Feng, J., Graf, M., Liu, K., Ovchinnikov, D., Dumcenco, D., Heiranian, M., et. al. (2016) Single-layer MoS2 nanopores as nanopower generators. Nature 536(7615):197-200.

Ferrar, J. A., Bedi, S., Zhou, S., & Zhu, P. (2018). Capillary-driven binding of thin triangular prisms at fluid interfaces. *Soft Matter*, *14*, 3902–3918. https://doi.org/10.1039/c8sm00271a

Fornito, A., Zalesky, A., & Breakspear, M. (2015). The connectomics of brain disorders. *Nature Reviews Neuroscience*, *16*(3), 159–172. https://doi.org/10.1038/nrn3901

Fournier, J.B. and Galatola, P. (2002) Anisotropic capillary interactions and jamming of

colloidal particles trapped at a liquid-fluid interface. *Phys. Rev. E* **65**, 031601. doi: 10.1103/PhysRevE.65.031601

Gao, R., Asano, S. M., Upadhyayula, S., Pisarev, I., Milkie, D. E., Liu, T., … Betzig, E. (2019). Cortical column and whole-brain imaging with molecular contrast and nanoscale resolution. *Science*, *363*(245), 1–16. http://doi.org/10.1126/science.aau8302

Gay, H. and Anderson, T.F. (1954). Serial sections for electron microscopy. Science, 120, 1071.

Gosse C & Croquette V. (2002) Magnetic Tweezers : Micromanipulation and Force Measurement at the Molecular Level. Biophys. J. 82(6):3314–3329.

Gur M, Purple RL, Whitehead R. (1972) Ultrastructure within the Lateral Plexus of the Limulus Eye. J. Gen. Phys. 1972;59(3):285-304.

Hafner, A.-S., Donlin-Asp, P., Leitch, B., Herzog, E., & Schuman, E. M. (2018). Local protein synthesis in axon terminals and dendritic spines differentiates plasticity contexts. *BioRxiv*, 363184. https://doi.org/10.1101/363184

Hall DH & and Russella RL. (1991) The Posterior Nervous System of the Nematode Caenorhabditis elegans: Serial Reconstruction of Identified Neurons and Complete Pattern of Synaptic Interactions. J Neurosci, 11(1):1-22.

Hamos JE, Van Horn SC, Raczkowski D, Sherman SM. (1987) Synaptic circuits involving an individual retinogeniculate axon in the cat. J Comp Neurol, 15;260(3):481.

Harris KM, et al. (2006) Uniform serial sectioning for transmission electron microscopy. J Neurosci, 26:12101–12103.

Hayworth KJ, Kasthuri N, Schalek R, Lichtman J. (2006) Automating the collection of ultrathin serial sections for large volume TEM reconstructions. Microsc Microanal, 12(Suppl. 2):86-87.

Hayworth, K. J., Morgan, J. L., Schalek, R., Berger, D. R., Hildebrand, D. G. C., & Lichtman, J. W. (2014). Imaging ATUM ultrathin section libraries with WaferMapper: a multi-scale approach to EM reconstruction of neural circuits. *Frontiers in Neural Circuits*, 8(June), 68. https://doi.org/10.3389/fncir.2014.00068

Helmstaedter M, Briggman, KL, Denk W. (2008) 3D structural imaging of the brain with photons and electrons. Curr. Opin. Neurobiol. 18, 633–641. doi:10.1016/j.conb.2009.03.005

Helmstaedter M, et al. (2013) Connectomic reconstruction of the inner plexiform layer in the mouse retina. Nature, 500:168–74.

Hildebrand, D. G. C., Cicconet, M., Torres, R. M., Choi, W., Quan, T. M., Moon, J., … Engert, F. (2017). Whole-brain serial-section electron microscopy in larval zebrafish. *Nature*, *545*(7654), 345–349. https://doi.org/10.1038/nature22356

Hoffpauir, B. K., Pope, B. & Spirou, G. (2007) Serial sectioning and electron microscopy of large tissue volumes for 3D analysis and reconstruction: a case study of the calyx of Held. Nat. Protoc. 2, 9–22.

Hua Y, Laserstein P, Helmstaedter M. (2015) Large-volume en-bloc staining for electron microscopy-based connectomics. Nat Commun, 6:7923. doi: 10.1038/ncomms8923.

Im, S.H., Lim, Y.T., Suh, D.J., & Park, O. O. (2002) Three-Dimensional Self-Assembly of Colloids at a Water–Air Interface: A Novel Technique for the Fabrication of Photonic Bandgap Crystals. Adv Mater, 14(19):1367-1369. doi:10.1002/1521-4095(20021002).

Jahanshad, N., Rajagopalan, P., Hua, X., Hibar, D. P., Nir, T. M., … Drost, D. (2013). Genome-wide scan of healthy human connectome discovers SPON1 gene variant influencing dementia severity. *Proceedings of the National Academy of Sciences*, *110*(12), 4768–4773. https://doi.org/10.1073/pnas.1216206110

Jiang X, Shen S, Cadwell CR, Berens R, Sinz F, Ecker AS, Patel S, Tolias AS. Principles of connectivity among morphologically defined cell types in adult neocortex. Science. 2015 Nov 27; 350(6264):aac9462.

Karimi, A., Odenthal, J., Drawitsch, F., Boergens, K. M., & Helmstaedter, M. (2019). Cell-type specific innervation of cortical pyramidal cells at their apical tufts. *BioRxiv*, 571695. https://doi.org/10.1101/571695

Kasthuri N, Hayworth KJ, Berger DR, Schalek RL, Conchello JA, Knowles-Barley S, et. al. Saturated Reconstruction of a Volume of Neocortex. Cell. 2015 Jul 30; 163(3):648-661.

Knott, G. & Genoud, C (2013). Is EM dead? *J. Cell Sci.* **126,** 4545–52.

Kodandaramaiah SB, Franzesi GT, Chow BY, Boyden ES, Forest CR (2012) Automated whole-cell patch-clamp electrophysiology of neurons in vivo. Nat Meth 9:585–587.

Korgaonkar, M. S., Fornito, A., Williams, L. M., & Grieve, S. M. (2014). Abnormal structural networks characterize major depressive disorder: A connectome analysis.

Biological Psychiatry, *76*(7), 567–574.
https://doi.org/10.1016/j.biopsych.2014.02.018

Kornfeld J, Denk W. Progress and remaining challenges in high-throughput volume electron microscopy. Curr. Op. Neurobiol. 2018 June; 50:261-267.

Kralchevsky, P.A., Denkov N.D., and Danov, K. (2001) Particles with an Undulated contact Line at a Fluid Interface: Interaction between Capillary Quadrupoles and Rheology of Particulate Monolayers. *Langmuir* **17**, 7694-7705.

Kuwajima M, Mendenhall JM, Lindsey LF, Harris KM (2013) Automated Transmission-Mode Scanning Electron Microscopy (tSEM) for Large Volume Analysis at Nanoscale Resolution. PLoS ONE8(3): e59573.
https://doi.org/10.1371/journal.pone.0059573

Lam, S. S., Martell, J. D., Kamer, K. J., Deerinck, T. J., Ellisman, M. H., Mootha, V. K., & Ting, A. Y. (2014). Directed evolution of APEX2 for electron microscopy and proximity labeling. Nature Methods, 12(1), 51–54.
https://doi.org/10.1038/nmeth.3179

Lee CY, Uzsoy R. Minimizing makespan on single batch processing machine with dynamic job arrivals. Int J Prod Res. 1999; 37(1):219-236.

Lee K, & Zung J, Li P, Jain V, Seung H. (2017). Superhuman Accuracy on the SNEMI3D Connectomics Challenge. arXiv:1706.00120.

Lee TJ, Lewallen CF, Bumbarger DJ, Yunker PJ, Reid RC, and Forest CR. Transport and trapping of nanosheets via hydrodynamic forces and curvature-induced capillary quadrupolar interactions. J. Colloid and Interface Sci. 2018 Jul 18; 531:352-359.
https://doi.org/10.1016/j.jcis.2018.07.068

Lee TJ, Kumar A, Balwani AH, Brittain D, Kinn S, Tovey CA, Dyer EL, da Costa NM, Reid RC, Forest CR, and Bumbarger DJ. Large-scale neuroanatomy using LASSO: Loop-based Automated Serial Sectioning Operation. PLoS ONE. 2018 Oct 23; 13(10): e0206172. https://doi.org/10.1371/journal.pone.0206172

Lee W-C A, Bonin V et al. (2016) Anatomy and function of an excitatory network in the visual cortex. Nature 532:370–374.

Lewandowski, E. P., Bernate, J. A., Searson, P. C., and Stebe, K. J. Rotation and alignment of anisotropic particles on nonplanar interfaces. *Langmuir*. **24,** 9302-9307 (2008).

Loudet, J. C., Alsayed, A. M., Zhang, J., and Yodh, A. G., (2005) Capillary Interactions Between Anisotropic Colloidal Particles. *Phys. Rev. Lett.* **94**, 018301. doi: 10.1103/PhysRevLett.94.018301

Lynall, M.-E., Bassett, D. S., Kerwin, R., McKenna, P. J., Kitzbichler, M., Muller, U., & Bullmore, E. (2013). Functional Connectivity and Brain Networks in Schizophrenia. *Journal of Neuroscience*, *30*(28), 9477–9487. https://doi.org/10.1523/jneurosci.0333-10.2010

Marblestone, A. H., Daugharthy, E. R., Kalhor, R., Peikon, I. D., Kebschull, J. M., Shipman, S. L., … Church, G. M. (2013). Conneconomics: The Economics of Dense, Large-Scale, High-Resolution Neural Connectomics. *BioRxiv*, *3*, 1–19. https://doi.org/10.1101/001214

McGuire, B.A., Gilbert, C.D., Rivlin, P.K., and Wiesel, T.N. (1991). Targets of horizontal connections in 804 macaque primary visual cortex. J Comp Neurol 305, 370-392.

Melouk S, Damodaran P, Chang PY. Minimizing makespan for single machine batch processing with non-identical job sizes using simulated annealing. Int J Production Economics. 2004 Jan 28; 87(2):141-147.

Mendez CA, Cerda J, Grossman IE, Harjunkoski I, Fahl M. State-of-the-art review of optimization methods for short-term scheduling of batch processes. Comp & Chem Eng. 2006 May 15; 30(6-7):913-946.

Micheva, K. D. and Smith, S. J. Array tomography: a new tool for imaging the molecular architecture and ultrastructure of neural circuits. *Neuron*. 55(5):824 (2007). doi:10.1016/j.neuron.2007.06.014

Monch, I., Schumann, J., Stockmann M., Arndt, K. F., Schmidt, O. G. (2011) Multifunctional nanomembranes self-assembled into compact rolled-up sensor–actuator devices. Smart Mater Struct., 20(8). doi:10.1088/0964-1726/20/8/085016

Nishiyama H, et al. (2010) Atmospheric scanning electron microscope observes cells and tissues in open medium through silicon nitride film. J Struct Biol 172:191–202.

Neuman, K. C. & Block, S. M. Optical trapping. (2004) Rev Sci Instrum, 75(9):2787-2809.

Oberti D, Kirschmann MA, Hahnloser RHR (2011) Projection neuron circuits resolved using correlative array tomography. Front Neurosci 5:1–8.

Ohyama, T., Schneider-Mizell, C.M., Fetter, R.D., Aleman, J.V., Franconville, R., Rivera-Alba, M., Mensh, B.D., Branson, K.M., Simpson, J.H., Truman, J.W., et al. (2015). A multilevel multimodal circuit enhances action selection in Drosophila. Nature 520, 633-639.

Porter KR, Claude A, Fullam EF (1945) A study of tissue culture cells by electron microscopy. J Exp Med 81: 233.

Probst, R., Cummins, Z., Ropp, C., Waks, E., & Shapiro, B. (2012) Flow Control of Small Objects on Chip: Manipulating Live Cells, Quantum Dots, and Nanowires. IEEE Control Sys Mag, 32(2):26-53. doi:10.1109/MCS.2011.2181584

Randel, N., Shahidi, R., Verasztó, C., Bezares-Calderón, L. A., Schmidt, S., & Jékely, G. (2015). Inter-individual stereotypy of the Platynereis larval visual connectome. *eLife*, *4*, 1–11. https://doi.org/10.7554/elife.08069

Rao, C. N. R., Sood, A. K., Subrahmanyam, K. S. & Govindaraj, A. (2009) Graphene: The New Two-Dimensional Nanomaterial. Angewandte, 48(42):7752–7777. doi:10.1002/anie.200901678

Reid RC. From Functional Architecture to Functional Connectomics. Neuron. 2012 Jul 26; 75(2):209-217.

Revell RSM, Agar AW (1955) The preparation of uniform plastic films. Br J Appl Phys 6:23-25.

Rogers, J. A., Lagally, M. G. & Nuzzo, R. G. (2011) Synthesis, assembly and applications of semiconductor nanomembranes. Nature, 477:45–53.

Rothenhöfer, G., Slocum, A., & Kitajima, T. (2013). An adjustable kinematic coupling for use in machine tools with a tight structural loop. *Precision Engineering*, *37*(1), 61–72. https://doi.org/10.1016/j.precisioneng.2012.07.001

Rowley JC, Moran DT (1975) A simple procedure for mounting wrinkle-free sections on formvar-coated slot grids. Ultramicroscopy 1:151–155.

Ryan, K., Lu, Z., and Meinertzhagen, I.A. (2016). The CNS connectome of a tadpole larva of Ciona intestinalis (L.) highlights sidedness in the brain of a chordate sibling. eLife 5, e16962.

Saffman, P. G. Brownian motion in thin sheets of viscous fluid. *J. Fluid Mech.* **73(4),** 593-602 (1976).

Savall J, Ho, ETW, Huang C, Maxey JR, Schnitzer MJ (2015) Dexterous robotic manipulation of alert adult Drosophila for high-content experimentation. Nat Meth 12:657–660.

Schalek R, Lee D, Kasthuri N, Peleg A, Jones T, Kaynig V, Haehn D, Pfister H, Cox D, and Lichtman J. Imaging a 1 mm3 volume of rat cortex using a multi beam SEM. Microsc Microanal. 2016; 22:582-583.

Schmidt-Krey, I. & Rubinstein, J. L. Electron cryomicroscopy of membrane proteins: Specimen preparation for two-dimensional crystals and single particles. *Micron* **42,** 107–116 (2011).

Sharifi-Mood N, Liu IB, Stebe KJ. (2016) Capillary interactions on fluid interfaces: Opportunities for directed assembly. Soft Matter Self-Assembly, 193:165.

Sharifi-Mood N, Liu IB, Stebe KJ. (2015) Curvature capillary migration of microspheres. Soft Matter, 11(34):6768-79.

Shenoy, A., Rao, C. V & Schroeder, C. M. (2016) Stokes trap for multiplexed particle manipulation and assembly using fluidics. Proc Natl Acad Sci U S A., 113(15): 3976-3981.

Shepherd GM, Harris KM. (1998) Three-dimensional structure and composition of CA3-->CA1 axons in rat hippocampal slices: implications for presynaptic connectivity and compartmentalization. J Neurosci,18(20):8300-10.

Shi J, Mao X, Ahmed D, Colletti A, Huang TJ. Focusing microparticles in a microfluidic channel with standing surface acoustic waves (SSAW). Lab Chip. 2007 Dec 20; 8(2):221-223.

Sjostrand FS (1958) Ultrastructure of retinal rod synapses of the guinea pig eye as revealed by three-dimensional reconstructions from serial sections. J Ultrastruct Res 2:122 -170.

Slocum, A. H. (1992). Design of three-groove kinematic couplings. *Precision Engineering*, *14*(2), 67–76. https://doi.org/10.1016/0141-6359(92)90051-W

Spacek J & Lieberman AR. (1974) Ultrastructure and three-dimensional organization of synaptic glomeruli in rat somatosensory thalamus. J Anat., 117(Pt 3): 487–516.

Stamou D., Duschl C., Johannsmann D. (2000) Long-range attraction between colloidal spheres at the air-water interface: The consequence of an irregular meniscus. *Phys. Rev. E.* **62,** 5263–5272.

Sterling P. Microcircuitry of the cat retina. (1983) Annu Rev Neurosci., 6:149-85.

Takemura, S.Y., Lu, Z., and Meinertzhagen, I.A. (2008). Synaptic circuits of the Drosophila optic lobe: 886 the input terminals to the medulla. J Comp Neurol 509, 493-513.

Takemura, S., Bharioke, A., Lu, Z., Nern, A., Vitaladevuni, S., Rivlin, P. K., Chklovskii, D. B. (2013). A visual motion detection circuit suggested by Drosophila connectomics. Nature, 500(7461), 175–181. http://doi.org/10.1038/nature12450

Tanyeri, M. & Schroeder, C. M. (2013) Manipulation and Confinement of Single Particles Using Fluid Flow. Nano Lett., 13(6):2357-2364.

Thompson SE and Parthasarathy S. Moore's law: the future of Si microelectronics. Materials Today. 2006 June; 9(6):20-25.

Trägårdh J, Macrae K, Travis C, Amor R, Norris G, Wilson SH, et. al. A simple but precise method for quantitative measurement of the quality of the laser focus in a scanning optical microscope. Journal of Microscopy. 2015 Jul; 259(1):66-73.

Valiente, M., & Marín, O. (2010). Neuronal migration mechanisms in development and disease. *Current Opinion in Neurobiology*, *20*(1), 68–78. https://doi.org/10.1016/j.conb.2009.12.003

Vella D & Mahadevan L. (2005) The "Cheerios effect". *American Journal of Physics* **73**, 817 doi: 10.1119/1.1898523

Walker GM and Beebe DJ. A passive pumping method for microfluidic devices. Lab on a Chip. 2002 Aug; 2(3):131-4.

Wang, F. Seo, J. H., Luo, G., Starr, M. B., Li, Z., Geng, D., et al. (2016) Nanometre-thick single crystalline nanosheets grown at the water- air interface. Nat. Commun., 7:1–7.

Wang, F., Seo, J. H., Ma, Z., & Wang, X. (2012) Substrate-Free Self-Assembly Approach toward Large-Area Nanomembranes. ACS Nano., 6(3)2602–2609. doi:10.1021/nn2050906

Wang, X., Xiong, Z., Liu, Z. & Zhang, T. (2015) Exfoliation at the Liquid / Air Interface to Assemble Reduced Graphene Oxide Ultrathin Films for a Flexible Noncontact Sensing Device. Adv Mater., 27(8):1370-1375. doi:10.1002/adma.201404069

Ware, R. W., & LoPresti, V. (1975). Three-dimensional reconstruction from serial sections. *International Review of Cytology*, *40*, 325–440.

Westfall, J. A. and Healy, D. L. (1962). A water control device for mounting serial ultrathin section. Stain technol., 37, 118.

White JG, Southgate E, Thomson JN, Brenner S. (1986) The Structure of the Nervous System of the Nematode Caenorhabditis elegans (The Mind of a Worm). Phil. Trans. R. Soc. Lond. B., 314: 1-340. doi: 10.1098/rstb.1986.0056

Williams, E. A., Verasztó, C., Jasek, S., Conzelmann, M., Shahidi, R., Bauknecht, P., … Jékely, G. (2017). Synaptic and peptidergic connectome of a neurosecretory center in the annelid brain. *eLife*, 6, 1–22. https://doi.org/10.7554/elife.26349

Williams, R. C., and Kallman, F. (1955). Interpretations of electron micrographs of single and serial sections. J. Biophys. Biochem. Cytol., 1, 301.

Womack J, Jones D, Roos D, Massachusetts Institute of Technology. The Machine that Changed the World: Based on the Massachusetts Institute of Technology 5-million dollar 5-year study on the future of the automobile. 1st ed. New York: Rawson Associates; 1990.

Wu Q, Kolb I, Callahan BM, Su Z, Stoy W, Kodandaramaiah SB, et. al. Integration of autopatching with automated pipette and cell detection in vitro. J. Neurophysiol. 2016 Oct 1; 116(4):1564-1578.

Würger A. (2006) Curvature-induced capillary interaction of spherical particles at a liquid interface. Phys Rev E, 74(4):041402.

Yao L, Sharifi-Mood N, Liu IB, Stebe KJ. (2015) Capillary migration of microdisks on curved interfaces. Journal of Colloid and Interface Science, 449:436-42.

Yushkevich PA, Piven J, Hazlettt HC, Smith RG, Ho S, Gee JC, Gerig G. User-guided 3D active contour segmentation of anatomical structures: significantly improved efficiency and reliability. Neuroimage. 2006 Jul 1; 31(3):1116-28.

Zheng, Z., Lauritzen, J. S., Perlman, E., Saalfeld, S., Fetter, R. D., Bock, D. D., … Kazhdan, M. (2018). A Complete Electron Microscopy Volume of the Brain of Adult Drosophila melanogaster. *Cell*, *174*(3), 730–743.e22. https://doi.org/10.1016/j.cell.2018.06.019